

Particle Size Segregation in Dense Granular Flows

THÈSE N° 7028 (2016)

PRÉSENTÉE LE 11 NOVEMBRE 2016

À LA FACULTÉ DE L'ENVIRONNEMENT NATUREL, ARCHITECTURAL ET CONSTRUIT
LABORATOIRE D'HYDRAULIQUE ENVIRONNEMENTALE
PROGRAMME DOCTORAL EN MÉCANIQUE

ÉCOLE POLYTECHNIQUE FÉDÉRALE DE LAUSANNE

POUR L'OBTENTION DU GRADE DE DOCTEUR ÈS SCIENCES

PAR

Kasper VAN DER VAART

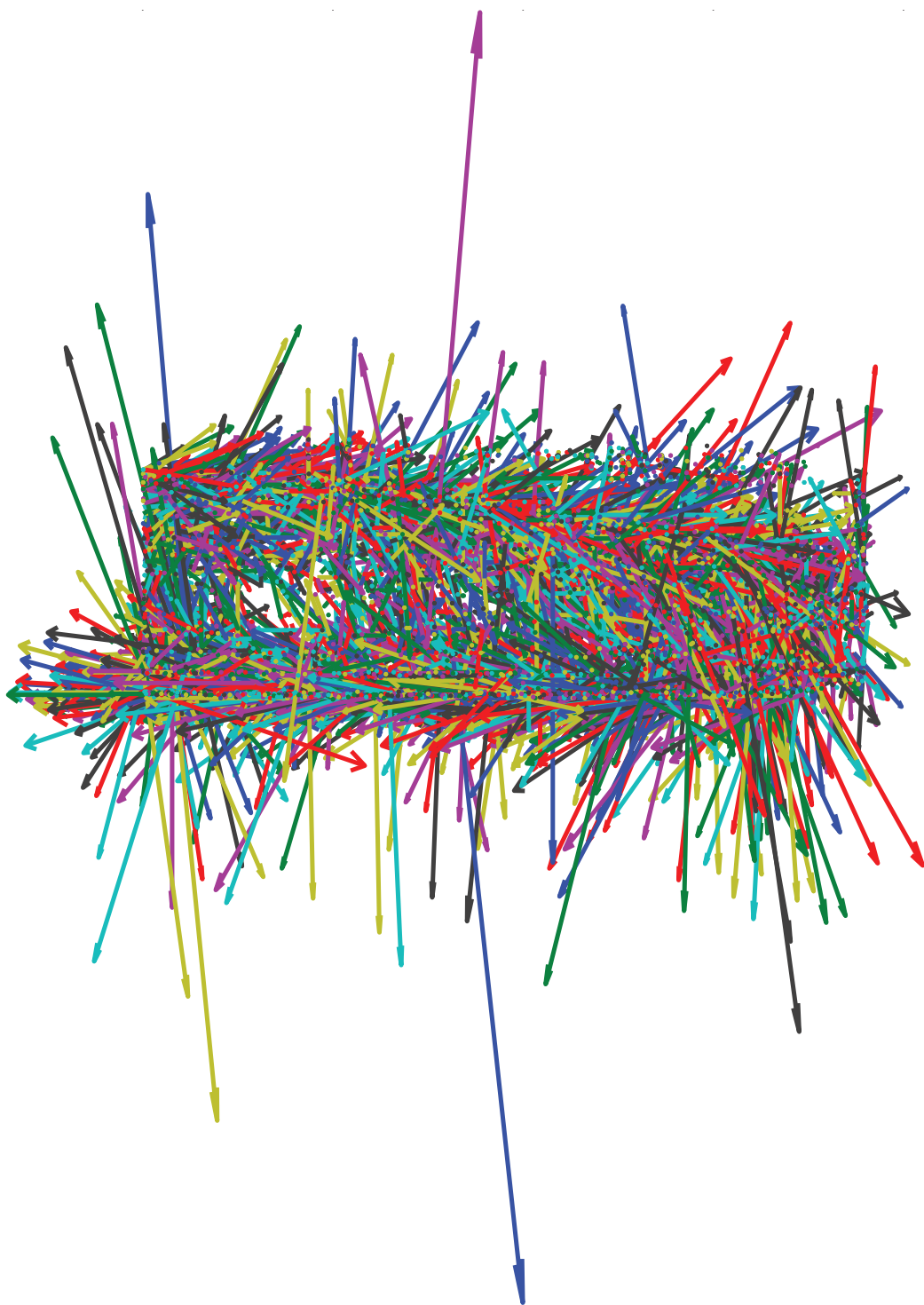
acceptée sur proposition du jury:

Prof. L. Laloui, président du jury
Prof. C. Ancey, directeur de thèse
Prof. N. Gray, rapporteur
Prof. A. Thornton, rapporteur
Prof. M. Wyart, rapporteur



ÉCOLE POLYTECHNIQUE
FÉDÉRALE DE LAUSANNE

Suisse
2016



Love does not consist in gazing at each other,
but in looking outward together in the same direction.

– Antoine de Saint-Exupery

To Siri...

Acknowledgements

I would like to thank first and foremost my supervisor Christophe Ancey, for his help and support, for letting me join the LHE, for always being available for advice when I came into his office, but most of all for trusting me and allowing me to make many decisions on my own. Unfortunately Christophe experienced severe health problems during my thesis work. Therefore I was lucky to have Nico Gray as a second mentor and my closest collaborator since the start of my Ph.D. It was thanks to him that one of the main ideas of my dissertation came into being. I want to thank Nico for patiently and enthusiastically answering all my theoretical questions, for teaching me about the bigger academic picture, and for trusting the gut feelings of a young experimentalist like me.

I also want to thank Anthony Thornton. Anthony has been my other closest collaborator and mentor during the second half of my thesis work. In Anthony I found the scientific equivalent of a soulmate. His passion for research and in particular the topic of size-segregation has been incredibly important for my continued effort in the study of this topic. Most importantly, through my discussions with Anthony I rediscovered the pleasure of doing research, despite the amount of setbacks and uncertainties one can experience in this profession.

I thank both Nico and Anthony for being on my jury, reading this thesis and their feedback. For the same reason I am grateful to Matthieu Wyart, the third member of my jury.

Besides the help of my mentors, most of the work in this dissertation would not have been possible without close collaborations with a number of other people. Therefore, I want to thank Thomas Weinhart for all his advice, help with simulations, and replying so quickly to my many emails. I thank Parmesh Gajjar, without whom I would not have had a paper in PRL. I also thank Nicolas Andreini, Chris Johnson, Deepak Tunuguntla, Bram van der Horn, Marnix van Schrojenstein Lantman, Kit Windows-Yule, and Bert Scheper for pleasant and fruitful collaborations.

During these years I had the opportunity to visit a number of conferences, workshops and other research groups, where I met many other wonderful people whom I want to thank for the good times, support, and all discussions about our work; Maxime Farin, Irana Denissen, Nico Rivas, Luca Orefice, Thomas Barker, James Baker, Geert Wortel, Casey LaMarche, Joshua Dijkman, Matt Harrington, Eric DeGiuli, Abdoulaye Fall, Marius Mermet-Guyennet, José Paredes, Janaina de Castro, Yasser Rahmani, Vijayakumar Chikkadi, Raphael Maurin, Matthias Schröter, Karen Daniels, Philippe Frey, Shiva Pudasaini, Nathalie Vriend, and Stefan Luding. In

Acknowledgements

similar spirit I want to thank my official EPFL mentor, François Gallaire, for advice during the earlier parts of my Ph.D., as well as Marco Ramaioli, for helpful discussions during his time at the LHE.

I want to thank my students; Jean-Lou Pfister, Justine Caillet, Jean-François Poustis, and Olivia Minam Borier, for giving me the opportunity to experience the joy of supervising and teaching. All of their work has been important for this thesis.

I want to take this opportunity to thank some people who have greatly influenced me during my undergraduate and graduate studies, and therefore have indirectly helped to make this dissertation possible; Wieteke de Boer, Tom Gregorkiewicz, Veerle De Graef, Frédéric Depypere, Koen Dewettinck, Daniel Bonn, and Peter Schall. I thank these people for their guidance and encouragement.

I am grateful for the unwavering support of Bob de Graffenried, our lab technician, handyman, IT specialist, photographer, and bead vacuumer. Without Bob I could not have done half the work I did. The same holds true for Michel Teuscher, head of the technical workshop, and his team, who have build all the experimental setups used in this work. Barbara Tinguely, our lab secretary, has always been helpful in all administration matters and I thank her for this. In similar vain I thank Sylvia Laarhuis, secretary of the MSM group, for her assistance. I want to thank my fellow Ph.D. colleagues at the LHE; Zhenzhu, Gauthier, Daniel and Blaise for their help and the enjoyable work environment. Thanks also to my good friends from the LCBC; Martin, Thibaud and Elisa, for all the good times.

Some of the people that have perhaps supported and encouraged me the most, through their love and friendship, did not live close by during these years. My best friend Benno and his partner Lana lived in Paris and now in Hamburg, and even though I did not see them more than three weeks in the last five years, our friendship most certainly made a difference to me, and I am thankful for that. I am also grateful for the support and love of my “in-laws”; Sybrandt, Ine, and Siepke van Keulen. During the last years they have embraced me as part of their family, which has made me very happy. On many occasions they also helped me write important pieces or make career decisions.

From the bottom of my heart I thank my mother, father and sister for their support and unconditional love, for trusting me to do the right thing, and for not taking me too serious. I’m sorry for not calling very often and for eating all the ice-cream when I am at home.

And finally “*drum roll...*” the love of my life, fellow scientist and adventurer; Siri Camee van Keulen, whom I thank for (unknowingly) motivating me to finish my studies in physics, for hours upon hours of discussing particle size-segregation, for unconditional support, trust, love, and endless laughs.

Abstract

Flows of granular materials widely occur in many industrial and natural environments. Particle-size segregation—the separation of grains of different sizes during flow—plays a crucial role in the behaviour of such flows. In spite of considerable efforts over the last years to investigate size-segregation, the phenomenon is still only partially understood. In particular for dense gravity-driven flows, where small particles percolate to the bottom of the flow and large particles rise to the top, against gravity, the particle-scale behavior and mechanisms are poorly understood.

This thesis presents an experimental and particle simulation investigation of size-segregation in dense gravity-driven bi-disperse granular flows in various three-dimensional configurations. Namely, an experimental shear-box, a numerical chute flow, an experimental moving-bed channel, and a numerical moving-bed channel. Using the non-intrusive imaging technique Refractive Index Matched Scanning (RIMS) we investigate the particle motion inside the bulk of the experimental configurations. The moving-bed channel was designed from the ground up with the use of the RIMS technique in mind.

The results obtained through both experiments and simulations demonstrate the existence of a property we call ‘size-segregation asymmetry’. This property is fundamental to the process of size-segregation and explains a number of specific features that arise on the bulk-scale of the flow. It can be simply and intuitively explained as follows: When a large particle in a granular flow is surrounded by many small particles it rises to the free-surface at a low velocity compared to the sinking velocity of a small particle in a flow surrounded by many large particles. We quantify this behaviour by measuring the segregation velocities as a function of local particle concentration. Comparison of the bulk concentration field with predictions of an asymmetric size-segregation model allow us to link the particle-scale behaviour to a number of bulk-scale features.

Segregation at the front of granular avalanches produces a recirculation zone, known as a ‘breaking size-segregation wave’, in which large particles are initially segregated upwards, sheared towards the front of the flow, and overrun before being reseggregated again. This recirculation zone separates a coarse particle front from a small-particle tail. By making use of a moving-bed channel, which permits the creation of a continuous gravity-driven flow, we are able to visualise, using RIMS, the complex internal structure of breaking size-segregation waves for the first time. We find that size-segregation asymmetry plays a role in the observed structure. In particular, it is seen that a few large particles are swept a long way upstream inside the small-particle tail and take a very long time to recirculate. Additionally, a basal slip

Acknowledgements

is observed that is linked to the local presence of the different sized particles, with the tail of the flow experiencing less friction compared to the front. By studying the basal slip we are able to explain the complex relation between the mixture ratio of the two species and the flow speed.

Overall, this thesis highlights the important role of the distinct dynamics of large and small particles in size-segregating granular flows.

Key words: Granular flows, Particle-size segregation, Particle-scale dynamics, Non-intrusive imaging, Asymmetric behaviour

Resume

Les écoulements granulaires sont omniprésents dans l'environnement et l'industrie. La ségrégation en taille—c'est-à-dire le tri de particules de différente taille dans l'écoulement—joue un rôle crucial dans le comportement de ces écoulements. En dépit d'efforts considérables, le phénomène reste partiellement compris. En particulier pour les écoulements denses gravitaires, dans lesquels les particules fines percolent vers le fond de l'écoulement tandis que les grosses particules remontent vers la surface, le comportement à l'échelle des particules et les mécanismes sont peu compris.

Cette thèse présente des recherches s'appuyant à la fois sur des expériences et des simulations particulières de la ségrégation dans des écoulements denses gravitaires composés de deux tailles de grains dans différentes configurations (à savoir une boîte de cisaillement et un canal à fond mobile pour les expériences, et un canal à fond fixe ou mobile pour les simulations). En me servant d'une technique de mélange iso-indice (appelée «scan par indice de réfraction ajustée»), j'ai étudié le mouvement des particules au sein de l'écoulement dans les expériences. Le canal à fond mobile a été conçu dès le début pour une utilisation avec des mélanges iso-indices. Les résultats obtenus montrent l'existence d'une propriété des écoulements appelée «asymétrie de la ségrégation en taille». Cette propriété est fondamentale pour le processus de tri granulométrique. Elle peut être expliquée de façon intuitive comme suit : quand une grosse particule d'un écoulement granulaire est entourée par beaucoup de petites particules, elle remonte vers la surface à une vitesse plus faible que celle d'une petite particule qui descendrait entourée de grosses particules. Je quantifie ce comportement en mesurant les vitesses de ségrégation en fonction de la concentration locale. La comparaison du champ de concentration moyen avec les prédictions fournies par un modèle de ségrégation asymétrique me permet de relier le comportement à l'échelle de la particule avec un certain nombre de caractéristiques macroscopiques.

La ségrégation dans le front d'avalanches granulaires crée une zone de recirculation appelée « vague déferlante de ségrégation », dans laquelle les grosses particules sont repoussées vers le haut de l'écoulement, transportées vers le front de l'écoulement, puis recirculées de nouveau. La zone de recirculation sépare un front riche en grosses particules et une queue riche en petites particules. En utilisant un canal à fond mobile, j'ai pu visualiser la structure interne complexe des vagues déferlantes dues à la ségrégation. C'est la première fois qu'une telle observation est réalisée. J'ai trouvé que l'asymétrie de ségrégation joue un rôle dans la structure observée. En particulier, quelques-unes des grosses particules sont repoussées loin en amont dans la queue riche en petites particules et ont besoin de bien plus de temps pour

Acknowledgements

recirculer. En outre, du glissement est observé sur le fond du canal ; il est lié à la présence de particules de différentes tailles ainsi qu'à la différence de frottement basal entre la queue de l'écoulement et le front. En étudiant le glissement au fond, j'ai pu expliquer la relation entre le rapport de mélange des deux fractions granulométriques et la vitesse de l'écoulement. Dans l'ensemble, la thèse éclaire le rôle important des dynamiques respectives des petites et grosses particules dans les écoulements soumis au tri granulométrique.

Mots clefs : écoulements granulaires, ségrégation granulométrique, dynamique particulière, imagerie non perturbatrice, asymétrie de comportement

Contents

Acknowledgements	i
Abstract (English/Francais)	iii
List of figures	xi
List of tables	xix
1 Introduction	1
1.1 Context and Motivation	1
1.1.1 Granular materials	1
1.1.2 Particle Segregation	3
1.2 Problem: Particle-Scale Analysis of Size-Segregation	5
1.3 Summary of Original Contributions	6
1.4 Organization of this Dissertation	7
2 Fundamentals of Granular Materials and Size-Segregation	9
2.1 Granular Materials	9
2.2 Dense Granular Flows	11
2.3 Particle-Size Segregation in Dense Granular Flows	13
2.3.1 Mechanisms for Size-Segregation	13
2.3.2 Theory and Modelling of Size-Segregation	15
2.4 Terminology	16
3 Methods and Techniques	17
3.1 Experimental Techniques	17
3.1.1 Refractive Index Matched Scanning	17
3.1.2 The RIMS Technique Applied	20
3.1.3 Image Analysis and Tracking	20
3.1.4 Complications and Uncertainties	22
3.2 Experimental Geometries	22
3.2.1 Shear-box	22
3.2.2 Shear-box RIMS Implementation	24
3.2.3 Moving-bed Channel	25
3.2.4 Moving-Bed Channel RIMS Implementation	27

Contents

3.2.5	Design Challenges of the Moving-Bed Channel	28
3.3	Numerical Simulations	33
3.3.1	Simulating the moving-bed channel	35
3.4	Summary of Particle Parameters	36
3.5	Differences between the simulations and experiments	36
4	Size-Segregation Asymmetry	37
4.1	Introduction	38
4.2	Theory and Modeling of Size-Segregation Asymmetry	39
4.3	Setup and Protocol	41
4.3.1	Experiments: Shear-box	41
4.3.2	Numerical Simulations: Chute Flow	43
4.4	Experimental Results: Shear-box	44
4.4.1	Phenomenology	44
4.4.2	Particle Dynamics	45
4.4.3	Displacement Dependence on Local Volume Fraction	49
4.4.4	Temporal Volume Fraction	50
4.5	Simulation Results: Chute Flow	52
4.5.1	Phenomenology	53
4.5.2	Trajectories and Mean Square Displacement	54
4.5.3	Displacement Dependence on Local Volume Fraction	58
4.6	Conclusions	62
5	Breaking Size-Segregation Waves	65
5.1	Introduction	66
5.2	Setup and Protocol	69
5.2.1	Experiments	69
5.2.2	Numerical Simulations	71
5.3	Results	71
5.3.1	Phenomenology	71
5.3.2	Velocity Profile	74
5.3.3	Time-averaged Structure	76
5.3.4	Recirculation	77
5.3.5	Slip Velocity	79
5.3.6	Mobility Feedback	80
5.3.7	Theoretical Comparison	83
5.4	Conclusions	83
6	Conclusion and Outlook	85
A	Theoretical Segregation Velocities	89
	Bibliography	102

Curriculum Vitae	103
-------------------------	------------

List of Figures

1.1	Granular materials occur on a vast range of scales and locations, from a pile of sugar grains in your kitchen (<i>a</i>), sand avalanches in the dessert (<i>b</i>), boulders on the moon (<i>c</i>) to ice particles in Saturn's rings (<i>d</i>). Image (<i>c</i>) and (<i>d</i>) courtesy of NASA.	2
1.2	Examples of particle-size segregation. (<i>a</i>) Larger strawberry pieces end up in earlier poured servings of cereals. (<i>b</i>) Large croutons end up in the outer regions and fine grains end up in the center when pouring on a heap. Images courtesy of Jenike & Johanson, Inc.	3
1.3	(<i>a</i>) Segregation in natural geophysical granular flows lifts large particles to the top of the flow. This results in inversely-graded layers in deposits. Two avalanches have occurred that have left two inversely-graded deposits where the particle-size distribution coarsens upwards. (<i>b–c</i>) Large particles can also be sheared towards the front of an avalanche, where they accumulate. This is shown in the debris flow deposit at Rif du Sap, Réserve Naturelle Haute Vallée de la Séveraisse, in the French Alps (<i>b</i>), and in an experimental debris flow deposit (<i>c</i>), USGS flume, Oregon, USA (August 2009). Image adapted from [Johnson et al., 2012]. (<i>d</i>) Coarse fronts are unstable and can break into a distinct channels that have large-particle levees lined with fine particles, as can be seen in pumiceous pyroclastic flow deposits from Mount St. Helens, 1980. Photograph courtesy of Dan Miller and USGS.	4
2.1	Force chains in a two-dimensional granular heap. The forces visualised using photo-elastic discs. Thicker white lines correspond to larger forces. The force network is highly heterogenous. Image adapted from [Zuriguel and Mullin, 2008].	10
2.2	Kinetic sieving is easy to imagine when you consider the system in (<i>a</i>): plenty of space for small particles to fall into. The system in (<i>b</i>) has less space, but perhaps particles can still fall occasionally. But what happens in system (<i>c</i>)?	14

List of Figures

3.1	Schematic of the RIMS technique. A mixture of transparent spherical grains is submerged in a liquid of the same refractive index as the grains. As a consequence the mixture becomes transparent. By adding a fluorescent dye and exciting this dye in a narrow plane with a laser sheet a cross-section of the mixture becomes visible. This cross-section can be imaged using a camera to obtain images with dark disks on a bright background. A filter in front of the camera blocks out the laser light and only permits the light emitted from the dye to reach the camera. Image adapted from [Andreini, 2016].	18
3.2	An example of the effect of refractive index matching and exciting a fluorescent dye in the mixture with a laser sheet. (<i>a–b</i>) This cup contains borosilicate beads and a liquid that is index matched. One can easily see the lines on the paper below the cup. (<i>c–d</i>) Here the same cup is illuminated with a laser sheet. The fluorescent dye is excited and emits light from within the cross-section.	19
3.3	Schematics of the two shear-box geometries that are used. (<i>a</i>) Traditional shear-box with rotation point at the bottom. (<i>b</i>) Improved shear-box with rotation point midway. The numbers indicate: (1) Side-walls made of Polyoxymethylene (POM); (2) Front- and back-walls made of glass; (3) Bottom-wall made of glass; (4) Additional glass bottom-wall; (5) Groove in the glass side-walls through which the additional glass bottom-wall (4) slides. Not depicted: the connection between the top of the oscillating side-walls and the driving motor.	23
3.4	A schematic of the RIMS implementation with the shear-box geometry. On the left is a front view and on the right is a side view. The shear-box is submerged in an aquarium filled with the RIMS liquid. A laser sheet is directed at the mixture from the bottom. The mixture is imaged from the front with one camera and from the back with another camera. Section (A) containing the lenses and the laser is moved by a stepper motor in order to scan the mixture.	24
3.5	(<i>a</i>) Schematic showing the general change in velocity field between a conventional channel and a moving-bed channel. The velocity field in the moving-bed channel is shifted to the left with the belt velocity. Image adapted from [Davies, 1990]. (<i>b</i>) A schematic of the moving-bed channel submerged in the aquarium. The numbers indicate: (1) the motor; (2) the belt; (3) the upper and lower wall that keep the granular mixture in the channel; (4) the aquarium filled with RIMS liquid; (5) a plastic box that lowers the total volume of RIMS liquid in the aquarium; (6) The inclination of the belt is changed by sliding along these points. Image courtesy of J.-L. Pfister.	25
3.6	A photograph of Channel A. See the schematic in Figure 3.5(<i>b</i>) for details. Image courtesy of J.-L. Pfister.	26
3.7	(<i>a</i>) A schematic of the laser setup for the moving-bed channel. (<i>b</i>) A photograph of the setup in the lab. Both images are courtesy of J.-L. Pfister.	27
3.8	A photograph of Channel B mounted on the carriage to facilitate a change in inclination. See the text for details.	28

3.9	(a) Channel A submerged in an aquarium with RIMS liquid. This is a simple solution, which unfortunately brings with it a host of challenges, namely; a large amount of liquid, which is difficult to control and accurately tune for RIMS; the laser sheet needs to travel to a large amount of liquid before it reaches the particle mixture, which, as a consequence of diffusion, reduces the thinness of the sheet. (b) Channel B with the aquarium build around the channel. This solution has a number of advantages, however its construction and design is much more challenging.	30
3.10	(a) The gates at the upslope and downslope ends of the channel can be removed by letting the belt curve upwards, a so-called U-belt. (b) Schematic of a U-belt consisting of individual bars.	31
3.11	(a) Photograph of a belt piece consisting of a metal construction with a plastic piece on top. The plastic piece can be slid off. (b) Side-view of a belt piece. (c) A schematic side-view of belt pieces. When they pass the concave corner the bars are pushed into each other. The distance between bars and their height must be carefully tuned to prevent jamming.	31
3.12	View inside Channel B, looking at the upstream wall. Don't be misled by the reflection of the belt in the right wall.	32
3.13	Schematic of the interior of Channel B, with the front panel removed. The yellow belt is drawn here as a continuous belt, whilst in fact it is made of discrete pieces. The red belt that is wrapped around the bottom two axis is a solution to drive the yellow belt. Friction is applied along the entire length of the channel instead of only at the axes.	33
4.1	Particle A is smaller than its neighbours and will sink. Particle B is larger than its neighbours and will rise. Does particle A sink at the same velocity as B rises? . .	37
4.2	Flux functions and segregation velocities. (a) Cubic (dashed line) with $\kappa = 0.97$ and quadratic (solid line) flux function. The cubic flux function is skewed to the left and asymmetric around $\phi = 0.5$. (b) Segregation velocity w_v ($v = l, s$) of large (green) and small (red) particles as a function of volume fraction ϕ for the quadratic (solid line) and cubic (dashed line), with $\kappa = 0.97$, flux functions. For the quadratic flux function the small and large particle velocities are identical but opposite, whereas for the cubic flux function the maximum of the small particle velocity is much higher than for the large and the maximum of large particles is shifted to intermediate ϕ	40
4.3	Schematic of the experimental setup. Full details can be found in Section 3.2. A raw data image is shown in grayscale and a cross-section of a reconstructed particle mixture in the setup. The colors are added for clarity, since the actual particles are transparent. This particular mixture is composed of particles of diameter 3 and 6 mm, which were used in preliminary testing. Image courtesy of G. Epely Chauvin.	42

4.4	Chute flow simulation of a bi-disperse mixture, shortly after startup, for $\Phi = 0.5$. The inclination is $\theta = 23^\circ$. The diameters of the large (orange), small (blue) and bed (yellow) particles are $d_l = 2.4$, $d_s = 1.0$ and $d_{base} = 1.7$, respectively. Gravity direction g and coordinates (x, z) are indicated, with the direction- y perpendicular to the xz -plane. The domain is periodic in the x - and y -directions.	43
4.5	Cross-sections at different times during an experiment. Particle positions are reconstructed from the experimental data. This particular mixture is composed of particles of diameter 3 and 6 mm, and is one of the preliminary tests. Image courtesy of G. Epely Chauvin.	45
4.6	(a) Time evolution of the vertical center of mass position z_m for large and small particles in $\Phi = 25\%$ (black), 50% (dark gray) and 75% (light gray) mixtures. $\theta_{max} = \pm 30^\circ$. (b) Segregation time \hat{t}_{seg} as a function of Φ ; solid line is a fit for the symmetric model with $S_r = 0.016$, whilst the dashed line is a fit for asymmetric model with $S_r = 0.030$ and $\kappa = 0.89$.	46
4.7	Individual particle dynamics for small particles (blue) and large particles (red) with $\theta_{max} = \pm 10^\circ$. (a) Vertical trajectories of a small particle segregating in a $\Phi = 0^+$ mix; and a large particle segregating in a $\Phi = 100^-$ mix. Inset: Particle movement in the horizontal plane. (b) RMSD $\sigma(\hat{\tau})$ for different mixtures (see legend), with the solid line a fit of $\sigma_s = \sqrt{D_0 \hat{\tau} + w_s^2 \hat{\tau}^2}$ at $\Phi = 50\%$ (shifted for clarity). The dotted lines show the slopes 0.5 and 1. Inset: $w_v(\Phi)$ for large (red) ($v = l$) and small particles (blue) ($v = s$).	47
4.8	Root mean square displacement for single cycles $\zeta = \sqrt{\langle \Delta z^2(\hat{\tau} = 1) \rangle}$ for small particle(s) (blue) and large particle(s) (red), with $\theta_{max} = \pm 10^\circ$, for mixtures of (a) $\Phi = 0^+$, (b) 50% and (c) 100%. The ζ for small particles in (b) and (c) is averaged over multiple particles. The ζ for large particles in (a) and (b) is averaged over multiple particles.	48
4.9	(a–b) Conditional probabilities $P(\Delta z_l \phi)$ and $P(\Delta z_s \phi)$. White curves are $\langle \Delta z_l \rangle$ and $\langle \Delta z_s \rangle$. (c–d) $ \langle \Delta z_l \rangle /A$ and $ \langle \Delta z_s \rangle /A$ as a function of ϕ , with error-bars indicating the standard error of the mean. Dashed and solid lines are plots of equation (4.7) for quadratic and cubic flux functions $F(\phi)$ with $S_r = 0.008$ and $S_r = 0.015$ respectively. The values of S_r were scaled to account for the lower shear rate $\gamma_0 \omega$ at $\theta_{max} = \pm 10^\circ$.	50
4.10	(a) Temporal development of $\phi(z, \hat{t})$ versus normalized flow height z/h for a $\Phi = 50\%$ mixture with $\theta_{max} = \pm 30^\circ$. (b)–(c) Theoretical predictions from equation (4.6). (b) Prediction using the symmetric flux function (4.2), with $S_r = 0.016$ and $S_r/D_r = 20.9$. The ratio S_r/D_r is found by least squares matching the steady end state. (c) Prediction using the asymmetric flux function (4.5), with $S_r = 0.030$, $S_r/D_r = 29.6$ and $\kappa = 0.89$.	51
4.11	Snapshots at different times of a simulation of a bi-disperse segregating mixture in a chute flow configuration. The yellow particles are the fixed rough bed. The global small particle volume fraction $\Phi = 50\%$. The size ratio is 2.4. The time increases from left to right. The slope inclination is $\theta = 23^\circ$.	53

-
- 4.12 Downstream velocity averaged over all particles $\langle u \rangle_p$ as a function of time for different global volume fractions Φ . Note that the sudden jump in $\langle u \rangle_p$ for $\Phi = 30\%$ at $t = 2300$ is the result of layer forming in the large particle mass. . . . 54
- 4.13 Example vertical trajectories of a single small intruder in a $\Phi = 0^+\%$ mixture (blue), and a single large intruder in a $\Phi = 100^-\%$ mixture (blue). Inset: y -trajectories. The x -trajectory is not shown because it is the downslope direction. 55
- 4.14 Vertical mean square displacement $\langle \Delta z^2(\tau) \rangle$ plotted as a function of delay time τ for single small particles in a $\Phi = 0^+\%$ mixture (blue circles), single large particles in a $\Phi = 100^-\%$ mixture (red circles), small particles in a $\Phi = 30\%$ mixture (light blue dots), and large particles in a $\Phi = 50\%$ mixture (orange +). For all data $\langle \dots \rangle$ indicates a time-average, except for the single small particles (blue circles), where it indicates both time- and ensemble averaging. The dashed lines indicate different slopes. 56
- 4.15 Mean vertical displacement $\langle \Delta z(\tau) \rangle$ as a function of delay time τ for large (red) and small (blue) particles chosen at random, for (a) $\Phi = 100^-\%$, (b) $\Phi = 30\%$ and (c) $\Phi = 50\%$. The $\langle \dots \rangle$ indicates a time average. 57
- 4.16 In a mixture of $\Phi = 30\%$: (a) Different plots of the average vertical displacement as a function of ϕ for $\tau = 1.5$ and varying W_{shell} . Inset: $\langle \Delta z_s(\phi = 0) \rangle$ plotted as a function of W_{shell} . The magnitude of the errorbars $E(W_{shell})$ is calculated by $E(W_{shell}) = 10^{-3} N_d(0.25) / N_d(W_{shell})$, where N_d is the amount of displacement data. The error is an indication of reduction in the amount of data with respect to the amount for the point at $W_{shell} = 0.25$. The standard deviation is not a good measure of the error because it remains fairly constant. (b) $\langle \Delta z_s(\phi) \rangle$ for different delay times τ . Inset: A plot of $\langle \Delta z_s(\phi) \rangle / \tau$ shows that all data in (b) collapses. The data for $\tau = 50$ with the * marker does not collapse on the other data. 59
- 4.17 The mean vertical displacement of large particles at $\phi = 1$ for different shell widths W_{shell} . Mixture $\Phi = 90\%$ and $\tau = 2.5$. The magnitude of the errorbars $E(W_{shell})$ is calculated by $E(W_{shell}) = 10^{-3} N_d(0.25) / N_d(W_{shell})$, where N_d is the amount of displacement data. The error is an indication of reduction in the amount of data with respect to the amount for the point at $W_{shell} = 0.25$ 60
- 4.18 (a) Semi-log plot and (b) normal plot of the absolute values of the mean vertical displacement as a function of ϕ for large particles (red) and small particles (blue), normalized by τ . The mixture $\Phi = 30\%$, $W_{shell} = 2$ for small and $W_{shell} = 2.5$ for large particles. Data sets for different τ are shown for both species in order to demonstrate a collapse by dividing by τ . The blue line and red line are the theoretical small particle velocity and large particle velocity, respectively, using an exponential flux function with $S_r = 1.7$ and $G = 3.7$ 61

List of Figures

- 4.19 (a) Semi-log plot and (b) normal plot of the absolute values of the mean vertical displacement as a function of ϕ for large particles (red) and small particles (blue), normalized by τ . $W_{shell} = 2$ for small and $W_{shell} = 2.5$ for large particles, whilst $\tau = 1.5$. Data sets for different Φ are shown with different symbols, and only those data points are plotted that are averaged over at least 10,000 displacements. The blue line and red line are the theoretical small particle velocity and large particle velocity, respectively, using an exponential flux function with $S_r = 1.7$ and $G = 3.7$ 62
- 5.1 Movement of large particles near the front of an avalanche. A large particle segregates to the free-surface and travels to the front because higher layers move faster. When a large particle is deposited on the bed it effectively travels backwards because the avalanche is flowing over it. If this particle gets picked up by the flow it will segregate again. 65
- 5.2 Field example of a snow avalanche that uprooted trees and entrained debris in the Puschlav valley (Grisons, Switzerland). The deposit exhibits a coarse front and lateral levees. Image courtesy of P. Bartelt, WSL-Institut, Davos. 66
- 5.3 (a) Fingering in experiments, performed in the lab of Nico Gray at the University of Manchester, and in (b) pumiceous pyroclastic flow deposits from Mount St. Helens, 1980. Photograph courtesy of Dan Miller and USGS. Coarse lateral levees (1) made up of larger brown grains channelize the flow. These levees are lined with finer light colored grains (2). Similar features are observed in the pyroclastic flow deposit although at a completely different scale. The channels in the experimental deposit are approximately 1.5 cm, whereas in the pyroclastic deposit they are of the order of 10 m. 67
- 5.4 A schematic diagram showing the formation of a breaking size-segregation wave. First large particles accumulate at the front (a). Next, small particles are sheared over the large particles (b). Because of size-segregation this configuration is unstable and the “wave” of small particles breaks, similarly to the breaking of a water wave as illustrated by the woodcut print The Great Wave from the Japanese artist Katsushika Hokusai (c). The result is a complex recirculation structure of small and large particles (d). 68

5.5	(a) A vertical section through a steadily propagating avalanche travelling down an inclined plane. In the body of the flow, the large grains segregate to the upper layers, where the velocity $u(z)$ is greatest, and hence are transported towards the front of the avalanche, where they are over-run, re-segregated upwards and recirculated to form a coarse-rich particle front. A breaking size-segregation wave forms between the vertically segregated flow in the rear of the avalanche and the coarse grained front. Although the front can increase in size when more large particles are supplied from the inversely graded flow upstream, the recirculation region shown with dotted lines reaches a steady structure that travels at the average speed u_{wave} . (b) In the moving-bed channel the belt moves upstream at a speed $u_{belt} = -u_{wave}$, driving an upstream flow in the lowest layers, whilst the upper layers move downstream under gravity. This generates a net velocity profile $\hat{u}(z) = u(z) - u_{wave}$ and is the same as examining the recirculation zone within the full avalanche (a) in a reference frame moving with u_{wave} . In the configuration in (b) there is no upstream supply of large particles, and so, provided that the segregation and diffusion rates are constant [Thornton and Gray, 2008], it is mathematically equivalent to the region in (a) marked by the dotted lines. Image reprinted from [Gajjar et al., 2016].	70
5.6	Photographs showing the steady recirculation regime established within the channel. These are dry preliminary tests using 5 mm and 14 mm glass marbles. The normal exposure photograph (a) shows that the large blue and white marbles collect towards the right, forming a coarse grained flow front at the downstream end of the channel, whilst the long exposure photograph (b) shows a time-averaged concentration field and the structure of the breaking size-segregation wave. An exposure time of 133 s was used to capture (b). Images reprinted from [Gajjar et al., 2016]	72
5.7	Snapshots of simulations with varying Φ . From top to bottom: $\Phi = 25\%$, 50% , 60% and 75% , for $u_{belt} = 3.55, 3.2, 3.2$ and 3.4 , respectively.	73
5.8	Belt velocity u_{belt} required to maintain a uniform flow depth along the channel for different global small-particle volume fractions Φ in the simulations.	73
5.9	Horizontal velocity profiles at different x positions for (a) the experiment with $\Phi = 70\%$ and (b) the simulation with $\phi = 60\%$. Each black dashed line indicates the zero velocity line for the data taken at that position. Red dashed lines are fits with $f(z) = bz^{3/2}$, where b is some constant.	74
5.10	Horizontal velocity u minus u_{belt} versus depth z , in the small particle tail, for (a) the experiment with $\Phi = 70\%$ and (b) the simulation with $\Phi = 60\%$. Red dashed lines are fits with $f(z) = bz^{3/2}$, where b is some constant.	75
5.11	(a) Snapshot of the experiment. The white label indicates the length scale of 14 mm. (b) Snapshot of a simulation for $\Phi = 62\%$. The fixed base particles are shown in grey. (c) The experimental time-averaged small-particle volume fraction field $\phi(x, z)$. (d) The time-averaged small-particle volume fraction field for the simulations. Images adapted from [Gajjar et al., 2016].	76

List of Figures

5.12 Simulation trajectories for a large particle (<i>a</i>) and a small particle (<i>b</i>) in a mixture of $\Phi = 50\%$, chosen at random. The color change in the trajectory is added to make it easier to follow. The arrows are a reminder that the top of the flow moves downstream, towards the right, and the bottom of the flow moves upstream, towards the left.	77
5.13 Experimental streamlines for large (<i>a</i>) and small (<i>c</i>) particles, constructed from velocity fields. Faded arrows indicate a lower concentration of that species. . .	78
5.14 Simulation streamlines for large particles (<i>a</i>) and small particles (<i>b</i>). Lighter color and larger arrows indicates a higher velocity. For a $\Phi = 50\%$ mixture. . . .	78
5.15 (<i>a</i>) Slip velocity $u_{slip} = u(z = 0) - u_{belt}$ in the simulations for three different global small-particle concentrations Φ . (<i>b</i>) Slip velocity in the simulations normalised by u_{belt} for mixtures of varying Φ and u_{belt} . The values of u_{belt} for each Φ can be found in Figure 5.8.	79
5.16 Slip velocity $u_{slip} = u(z = 0) - u_{belt}$ for $\Phi = 50\%$ plotted together with $\phi(x, 0)$ and $\phi_l(x, 0) = 1 - \phi(x, 0)$	80
5.17 (<i>a</i>) Plotted as a function of Φ : The mean downstream free-surface velocity $\bar{u}(h)$, where h is the flow depth; the absolute value of the mean velocity at the bed $ \bar{u}(0) $; and the mean slip velocity \bar{u}_{slip} . (<i>b</i>) The belt velocity as a function of Φ	81
5.18 (<i>a</i>) The experimental time-averaged small-particle volume fraction field $\phi(x, z)$. (<i>b</i>) The time-averaged small-particle volume fraction field for the simulations. (<i>c</i>) Continuum BSS wave structure with an asymmetric flux function. The solid lines mark the boundaries of the recirculation zone, with two distinct ‘lens’ and ‘tail’ regions, marked by A and B respectively. Image adapted from [Gajjar et al., 2016].	82

List of Tables

- 3.1 Various parameters for the different experiments and simulations performed in Chapter 4 and 5. The parameters are: the small and large particle diameter d_s and d_l respectively, the size ratio $s = d_l/d_s$, the particle density ρ_p , the collision time t_c , the coefficient of restitution r_c , the magnitude of the gravitational acceleration g , and the inter-particle friction μ_p 36

1 Introduction

“Time you enjoy wasting, was not wasted.”

– John Lennon

EVERYDAY we come into contact with all sorts of different materials. Our surroundings are filled with objects with a broad spectrum of complex properties, ranging from mechanical properties such as hardness, chemical properties like pH to optical properties such as reflectivity. The most general classification of materials is to divide them into solids, liquids and gases. The materials that make up our everyday environment typically fall in one of these three categories. If you ask anyone they would probably not know that there are other forms of matter besides these three well known ones. Some examples of exotic forms of matter, that behave differently from solids, liquids and gases, are plasmas and liquid crystals, as are found in flatscreen TVs. Less well known by their name but exceedingly more common are *granular materials*, for example: sand, snow, flour, sugar, beans, cereals, rice, coffee, and pet food. The individual components of granular materials are usually ordinary solids, but by combining them in large aggregates remarkable properties emerge. This dissertation focusses on one of these properties: the ability to separate particles of different sizes during flow.

1.1 Context and Motivation

1.1.1 Granular materials

Granular materials consist of large assemblies of discrete macroscopic elements—which shall be referred to from here on as “grains” or “particles”—that interact through contacts and collisions. The individual grains that make up a granular material do not necessarily possess any special properties, but because of how they behave collectively a rich diversity of behaviour arises, that can be very different from the behaviour of common solids, liquids and gases [Jaeger et al., 1996; Duran, 2012]. To illustrate this, consider the example of pouring sugar on a flat surface. First of all, sugar is made of solid particles, but it can still flow as if it

Chapter 1. Introduction

were a liquid. When poured, a heap of sugar will form, as shown in Figure 1.1(a). This heap consists of a solid-like interior and liquid-like flowing layers on the slopes of the heap. When pouring is stopped, grains on the slopes will come to rest and the heap remains.

Granular materials occur on a vast range of scales, from a small heap of sugar to giant ice-belts in Saturn's rings that span hundreds of kilometres in size (see Figure 1.1). Because of their ubiquitous presence, granular materials are the second-most manipulated material in industry (second only to water) [de Gennes, 1999] and the processing of granular materials accounts for roughly 10% of all the energy produced on this planet [Duran, 2012]. Many challenges in industrial and geological contexts arise due to the complex and unpredictable properties of granular materials. For example, unwanted clogging of silo's [To et al., 2001] or devastating debris flows [Iverson, 1997]. Not surprisingly, the study of granular materials has a long history with Coulomb, Faraday and Reynolds being the earliest pioneers. Despite this, much of the physics that drives the behaviour of granular materials is still not fully understood. One of the reasons for this gap is that many of the existing mathematical tools in thermodynamics and statistical mechanics—which have been put to great use to model the behaviour of solids, liquids, and gases—are inapplicable to granular materials. As such, research on granular materials continues with more effort than ever before.



Figure 1.1: Granular materials occur on a vast range of scales and locations, from a pile of sugar grains in your kitchen (a), sand avalanches in the desert (b), boulders on the moon (c) to ice particles in Saturn's rings (d). Image (c) and (d) courtesy of NASA.

1.1.2 Particle Segregation

One of the special properties of granular materials is their ability to spatially separate grains of different properties when mechanically agitated. This process is called particle segregation. The most common types of particle segregation are density- and size-segregation, where larger/denser particles separate from smaller/lighter particles, but segregation due to differences in shape or surface properties also exists [Aranson and Tsimring, 2006].

Segregation is easily observable in a box of breakfast cereals: When opening the box all of the larger nuts will be on top. After a couple of servings when the box is nearly empty it will contain mostly smaller grains (see Figure 1.2(a)). The explanation for this behaviour is that during transport and handling of the box size-segregation has occurred; all of the finer grains have sunk to the bottom whilst all of the larger grains have risen to the top. Similarly, when pouring a mixture of different sized grains on a heap, large particles will end up on the outer regions and small particles will end up in the centre of the heap, as shown in Figure 1.2(b). Segregation takes place in the thin flowing layers on the surface of the heap. There the small grains fall through gaps between the large grains and are deposited, whilst the large particles flow to the bottom of the heap.

The process of segregation is dependent on many factors and therefore difficult to predict and control. Small differences in particle properties as well as the type of mechanical agitation (shaking, vibrating or shearing) have a different effect on the amount and direction of segregation. This complexity poses significant challenges in numerous industries where granular materials are processed, such as chemical and pharmaceutical engineering, agriculture, food-processing, and construction industries [Williams, 1976, 1968; Johanson, 1978; Shinbrot and Muzzio, 2000]. Often these industries require a completely homogeneous mixing of their products and even a small separation of the different ingredients can critically degrade the final product quality, leading to huge economic losses. Consider for example medicine or concrete: inaccurate mixing of these products can potentially cost lives. As a consequence segregation has been studied for many years in industrial configurations such as rotating drums [e.g. Nityanand et al., 1986; Shinbrot and Muzzio, 2000], silos [e.g. Schulze, 2008; Cellai

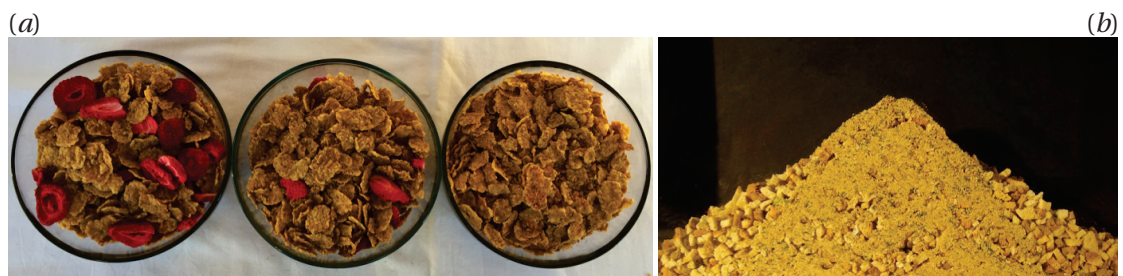


Figure 1.2: Examples of particle-size segregation. (a) Larger strawberry pieces end up in earlier poured servings of cereals. (b) Large croutons end up in the outer regions and fine grains end up in the center when pouring on a heap. Images courtesy of Jenike & Johanson, Inc.

Chapter 1. Introduction

et al., 2012], or chutes and hoppers [e.g. Khakhar et al., 1999].

Segregation is also commonplace in natural environments where it is most efficient in dense granular flows [GDRMiDi, 2004] such as snow avalanches [Bartelt and McArdell, 2009; McElwaine and Nishimura, 2000], debris flows [Iverson, 1997] and submarine grain flows [Dingler and Anima, 1989]. Because large particles rise towards the top of the flow, deposits of these flows often show inverse-grading, i.e., an upward coarsening of the particle-size distribution, as shown in Figure 1.3(a) [e.g. Fisher and Mattinson, 1968; Schmincke, 1967; Middleton, 1970; Hunter, 1985; Hunter and Kocurek, 1986; Cas and Wright, 1987]. The faster moving top layers can also carry large particles to the front of the flow, hence deposits often display coarse particle fronts (see Figure 1.3(b–c)) [e.g. Costa and Williams, 1984; Middleton and Hampton, 1976; Sohn and Chough, 1993]. The accumulation of coarse grains at the front creates a resistive margin, which is unstable and can break into a series of finger-like channels [Pouliquen et al., 1997; Pouliquen and Vallance, 1999; Woodhouse et al., 2012]. Such channels can be seen in



Figure 1.3: (a) Segregation in natural geophysical granular flows lifts large particles to the top of the flow. This results in inversely-graded layers in deposits. Two avalanches have occurred that have left two inversely-graded deposits where the particle-size distribution coarsens upwards. (b–c) Large particles can also be sheared towards the front of an avalanche, where they accumulate. This is shown in the debris flow deposit at Rif du Sap, Réserve Naturelle Haute Vallée de la Séveraisse, in the French Alps (b), and in an experimental debris flow deposit (c), USGS flume, Oregon, USA (August 2009). Image adapted from [Johnson et al., 2012]. (d) Coarse fronts are unstable and can break into a distinct channels that have large-particle levees lined with fine particles, as can be seen in pumiceous pyroclastic flow deposits from Mount St. Helens, 1980. Photograph courtesy of Dan Miller and USGS.

the pumiceous pyroclastic flow deposits from Mount St. Helens shown in Figure 1.3(d). The channels exhibit coarse-grained levees [Pierson, 1986; Johnson et al., 2012], which are lined with small particles that lubricate the flow [Kokelaar et al., 2014]. This allows the flow to run out further at higher velocities, potentially increasing its destructive power.

The ability to accurately predict and control segregation in both industrial and geophysical contexts is of great importance. Indisputably, the study of segregation within densely flowing granular materials is equally important. It is therefore the topic of this dissertation. The remainder of this introduction discusses the problem statement, summarizes the original contributions and outlines the organization of this dissertation.

1.2 Problem: Particle-Scale Analysis of Size-Segregation

A number of continuum models have been proposed for size-segregation in dense granular flows [e.g. Savage and Lun, 1988; Dolgunin and Ukolov, 1995; Gray and Thornton, 2005; May et al., 2010; Fan and Hill, 2011; Marks et al., 2012; Tunuguntla et al., 2014; Schlick et al., 2015]. These models are successful in capturing the separation of different sized particles and the final steady state, but fail to reproduce accurately the evolution of the segregation process in time [Wiederseiner et al., 2011b; Fan and Hill, 2011; Marks et al., 2011, 2012]. A possible reason for this is that some of the assumptions about the nature of size-segregation, on which these models are based, have thus far not been verified in experiments or simulations. For instance, the dependence of segregation flux on local species concentration; the precise partitioning of pressure between different sized particles; or, the in-dependence of particle drag on local species concentration. In fact, there remains a general gap in the understanding of size-segregation on the particle-scale level. This incomplete characterization of particle-scale dynamics will make the task of developing more accurate theoretical models most likely impossible.

The problem addressed in this thesis is the particle-scale analysis of size-segregation in dense granular flows. The reason this is still an open problem is that analyzing the motion of individual particles in granular flows is a major challenge. Granular materials are opaque and tracking of particles can only be done near sidewalls where, unfortunately, the particle behaviour is modified by the presence of the walls. In the case of size-segregation, smaller particles are preferentially positioned near the sidewalls. Particle simulations can easily circumvent this problem by using periodic walls and by recording the position and velocity of each particle. However, most work involving simulations has focussed on bulk properties such as pressure, stresses, segregation time, concentration, etc., thereby neglecting their full potential to study individual particle dynamics and gaining a deeper understanding of the segregation process.

This thesis contains a body of work which reveals new insights into particle-scale behaviour in size-segregating dense granular flows. Particle-scale dynamics are resolved using simulations and experiments where particles inside the bulk are visualised with non-intrusive

imaging techniques. The following section will summarize the original contributions of this dissertation.

1.3 Summary of Original Contributions

This dissertation provides three main contributions.

The first contribution, described in Chapter 3, is the development of a moving-bed channel setup for use in combination with the technique of refractive index matched scanning (RIMS) [Wiederseiner et al., 2011a; Dijkman et al., 2012] for the study of breaking size-segregation waves [Thornton and Gray, 2008]. Although the concept of a moving-bed channel existed before, its implementation with RIMS is novel. The final setup allows the continuous and indefinite visualization of the *interior* of a *gravity-driven* granular flow that remains stationary in the reference frame of the lab. The initial inspiration for the setup was provided by Nico Gray and Christophe Ancey. It was designed, planned and tested by Kasper van der Vaart.

The second contribution, described in Chapter 4, is the discovery and in-depth study of an asymmetry in large- and small-particle segregation velocities. The segregation velocities dictate how fast a large particle rises and a small particle sinks during segregation. When a large particle is surrounded by many small particles its segregation velocity is very low. Whilst a small particle surrounded by many large particles has a very high segregation velocity. This non-reciprocity is what we call *size-segregation asymmetry*. The complex dependence of the segregation velocities on the local concentration of large and small particles is rooted in the difference between the segregation mechanism for large particles and that for small particles. These mechanisms have distinct dynamics associated with them and their asymmetry affects the bulk segregation as well: The time for complete segregation and the time-evolution of the depth dependent concentration field depend on the asymmetry. These findings are important because they suggest why current state-of-the-art modeling approaches do not accurately capture the time-evolution of the concentration field and the segregation time.

The asymmetry phenomenon has been studied through both experiments as well as simulations. The experimental findings have been published in the letter titled “Underlying Asymmetry within Particle Size Segregation” that was published in 2015 in volume 114 of Physical Review Letters. The authors of the letter are Kasper van der Vaart (KvdV), Parmesh Gajjar (PG), Gael Epely-Chauvin (GEC), Nicolas Andreini (NA), Nico Gray (JMNTG) and Christophe Ancey (CA). The paper was jointly written by KvdV and PG. The experiments and analyses were conducted by KvdV, whilst the theory was developed by PG. Editorial comments to the manuscript were provided by JMNTG and CA. The initial experimental setup was jointly developed by GEC, NA, JMNTG and CA, whilst the inspiration for the asymmetric behaviour was provided by KvdV. The simulation work and analyses, conducted by KvdV, have not yet been published.

The third contribution, described in Chapter 5, is the study of breaking size-segregation

waves. A breaking size-segregation (BSS) wave is a complex recirculating structure of small and large particles near the front of a granular flow. It is a direct result of size-segregation and was predicted by Thornton and Gray [2008]. Since its prediction, BSS waves have only been indirectly observed in experiments. The work in Chapter 5 shows for the first time the actual structure of a BSS wave in experiments and simulations.

For this dissertation BSS waves have been studied through both experiments as well as simulations. Part of the experimental and simulation results have been published in the paper titled “Asymmetric breaking size-segregation waves in dense granular free-surface flows” that was published in 2016 in volume 794 of the *Journal of Fluid Mechanics*. The authors of the article are Parmesh Gajjar (PG), Kasper van der Vaart (KvdV), Anthony R. Thornton (ART), Chris G. Johnson (CGJ), Christophe Ancey (CA) and Nico Gray (JMNTG). The paper was written by PG, who also performed all of the theoretical work on asymmetric breaking wave structures and particle paths. The moving-bed flume experiments and analysis were performed by KvdV. The experiments and analysis were supervised by CA, whilst the numerical Discrete Particle Method simulations and analysis were performed by KvdV and ART. CGJ provided additional analysis of the experimental data. KvdV and ART both contributed text to the introduction section of the paper. Editorial comments were provided by KvdV, ART, CGJ, and JMNTG.

1.4 Organization of this Dissertation

This thesis is structured as 6 main chapters, two introductory chapters including this one, a chapter on the techniques and protocol, two chapters containing results and analysis, and a conclusion chapter.

Chapter 2 provides more context and discusses basic understanding and behaviour of granular materials and dense granular flows. Importantly, an overview is given of the current state-of-the-art in particle-size segregation in dense granular flows.

Chapter 3 describes the different experimental geometries used; the shear-box and moving-bed channel. The imaging technique Refractive Index Matched Scanning is explained and its implementation on each of the experimental setups is described. The protocol and general details of the numerical simulations are outlined here as well. A considerable part of the chapter is devoted to discussing the design challenges and solutions for the moving-bed channel.

Chapter 4 presents the results of shear-box experiments and chute flow simulations. The discovery of size-segregation asymmetry is described and quantified through the data obtained from shear-box experiments. The results of the chute flow simulations provide additional support for the existence of size-segregation asymmetry.

Chapter 5 reports observations from experiments and particle simulations in a moving-bed channel, which reveal the structure of breaking size-segregation waves and the effect that

Chapter 1. Introduction

size-segregation asymmetry has on this structure.

Finally, Chapter 6 draws together the research in this thesis with conclusive remarks and suggests future avenues to explore.

2 Fundamentals of Granular Materials and Size-Segregation

“We’re born with infinite possibilities, only to give up on one after another. To choose one thing means to give up on another. That’s inevitable. But what can you do? That’s what it is to live.”

– Hayao Miyazaki

THIS chapter begins with a discussion of the basic physics of granular materials and dense granular flows, which is followed by an overview of particle size-segregation in dense granular flows and the fundamental mechanisms that are thought to drive size-segregation.

The physics of granular materials are still under very active investigation and only partially understood. Many different behaviours and phenomena are known, of which particle size-segregation is but one. A complete treatment of the current understanding and available knowledge on granular materials and its behaviours lies outside the scope of this dissertation. The focus is on the fundamentals necessary to understand the remainder of the work presented here, which concerns particle-size segregation in dense granular flows. For an in-depth treatment of the physics of granular materials I strongly recommend “Granular media: between fluid and solid” by Andreotti, Forterre and Pouliquen [Andreotti et al., 2013]. For an overview of particle segregation I point the reader to the reviews of Ottino and Khakhar [2000] and Gray et al. [2015], as well as the excellent overview in the work of Tunuguntla et al. [2016].

2.1 Granular Materials

Granular materials can exhibit solid-, liquid- and gas-like behaviour. The keyword here is “like”. Certainly a heap of sand can be molten in a furnace to become a flowing glass, but then it would not be considered a granular material anymore. The solid-, liquid-, and gas-like states of an actual granular material, composed of many discrete macroscopic particles, are not the same as those well known forms of matter. The important difference is that, for granular

materials, mechanical forces take the role of temperature. Because granular materials are composed of macroscopic grains, temperature has no effect on their behaviour. For a granular material to transition from a solid to a liquid state energy needs to be supplied in the form of mechanical agitation or other forces, such as magnetic, hydrodynamic, aerodynamic or gravitational forces.

A quantitative way of looking at this is to determine the work required to move one grain of mass m a distance equal to its diameter d against gravity. For a typical 1 mm sand grain the work mgd is of the order of 10^{-8} Joule, with g being the gravitational acceleration. The typical thermal energies at room temperature are of the order of 10^{-21} Joule, as given by the Boltzmann constant k_B multiplied with the temperature. The difference is 13 orders of magnitude. As long as the grains in a mixture are larger than $1\ \mu\text{m}$ it can be considered a granular material.

A granular material at rest behaves like a solid. It is characterized by a dense state in which particles have many persistent contacts. The material can support its own weight and forces are distributed through a heterogenous percolating network of force chains [Majmudar and Behringer, 2005; Mueth et al., 1998], as shown in Figure 2.1. Even when very small forces are applied the behaviour of a granular material is reminiscent of that of solids. In this situation grain inertia is negligible and the bulk behaviour can be described in terms of plasticity [Nedderman, 2005; Schofield and Wroth, 1968]. When larger forces are applied a granular material starts to flow similarly to a liquid [GDRMiDi, 2004]. The material is still very dense with a solid fraction between random loose packing and random close packing. Particles have many intermittent-contacts with other grains and motion is highly correlated [Pouliquen, 2004]. Grain inertia becomes important but the force network persists and continuously

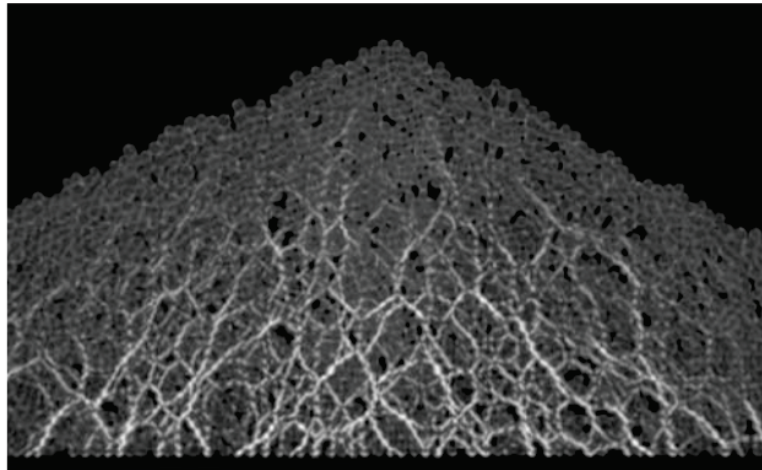


Figure 2.1: Force chains in a two-dimensional granular heap. The forces visualised using photo-elastic discs. Thicker white lines correspond to larger forces. The force network is highly heterogenous. Image adapted from [Zuriguel and Mullin, 2008].

evolves. The frictional contacts between the particles and their inelasticity dissipates energy, therefore if not enough energy is supplied the flow will come to rest. When even more energy is supplied a flowing granular material can become gas-like with particles spaced far apart such that only binary collisions occur. A typical way of creating a granular gas in a controlled environment is by shaking or vibrating it vigorously [e.g. Knight et al., 1993; Rosato et al., 2002; Huerta and Ruiz-Suárez, 2004].

Although the properties of granular materials depend primarily on the characteristics of the particles themselves and their interactions, the environment—surfaces, walls and the interstitial liquid—also plays a crucial role. The interstitial space is typically filled by a gas (usually air) or a liquid, which can give rise to hydrodynamic and aerodynamic forces. When the environment is very humid capillary bridges can form between particles, which result in attractive forces [Kohonen et al., 2004; Richefeu et al., 2006]. On the other hand, repulsive forces arise due to electric surface charges on the particles [e.g. Cross, 1987; LaMarche et al., 2009]. When all these effects due to the environment are absent, or small enough so that they can be ignored, we are dealing with a so-called “dry” granular material [Herrmann et al., 2013]. Non-dry granular materials can be far more complex than dry granular materials and exhibit a variety of behaviours depending on the media involved and the density of particles in the medium [Mitarai and Nori, 2006; Chong et al., 1971]. This field of study encompasses a broad range of materials, from dense suspensions to porous materials, that lie outside the scope of this dissertation, which focusses on a highly simplified situation in which interactions are purely due to sliding, rolling and collisions.

2.2 Dense Granular Flows

Dense granular flows are observed in many different configurations [e.g. Silbert et al., 2001; Ertaş et al., 2001; Forterre and Pouliquen, 2008; Pouliquen and Chevoir, 2002], ranging from shear cells, vertical chutes, hoppers, inclined planes and heap flows [GDRMiDi, 2004]. They are characterized by a high solids volume fraction $0.5 < \nu < 0.65$, where a contact network still exists, even though the material as a whole is moving [Andreotti et al., 2013; GDRMiDi, 2004]. These flows can be described using continuum quantities such as the local density $\rho(x, t)$, the local velocity $\mathbf{u}(x, t)$, the local pressure $p(x, t)$ and the local deviatoric stress $\boldsymbol{\tau}(x, t)$. These quantities are related through mass and momentum conservation

$$\frac{\partial \rho}{\partial t} + \nabla \cdot (\rho \mathbf{u}) = 0, \quad (2.1)$$

$$\frac{\partial}{\partial t}(\rho \mathbf{u}) + \nabla \cdot (\rho \mathbf{u} \otimes \mathbf{u}) = -\nabla p + \nabla \cdot \boldsymbol{\tau} + \rho \mathbf{g}, \quad (2.2)$$

where ∇ is the vector differential operator, \otimes is the dyadic product and \mathbf{g} is the gravitational acceleration vector. The deviatoric stress $\boldsymbol{\tau}$ is linked to other parameters via the constitutive

law [Jop et al., 2005; Pouliquen et al., 2006]:

$$\boldsymbol{\tau} = \mu(I) p \frac{\mathbf{D}}{\|\mathbf{D}\|}. \quad (2.3)$$

Here \mathbf{D} is the strain rate tensor defined as

$$\mathbf{D} = \frac{1}{2}(\nabla \mathbf{u} + \nabla \mathbf{u}^T), \quad (2.4)$$

where the superscript T indicates the transpose and $\|\mathbf{D}\| = \sqrt{\frac{1}{2}\text{tr}\mathbf{D}^2}$, with tr the trace. The friction coefficient μ is a function of the so-called inertial number I , a relation that is referred to as the $\mu(I)$ -rheology [Jop et al., 2005; Pouliquen et al., 2006], given by

$$\mu(I) = \mu_1 + \frac{\mu_2 - \mu_1}{I_0/I + 1}, \quad (2.5)$$

with I the non-dimensional inertial number and I_0 a constant:

$$I = \frac{2\|\mathbf{D}\|d}{\sqrt{p/\rho_p}}, \quad I_0 = \frac{5\beta d}{2L\sqrt{v}}. \quad (2.6a,b)$$

Here, d is the particle diameter, v is the solids volume fraction, β is an empirical constant, L is an empirical length scale, and ρ_p is the density of the particle material. The friction coefficients $\mu_1 = \tan\zeta_1$ and $\mu_2 = \tan\zeta_2$ are related to the minimum and maximum slope inclinations ζ_1 and ζ_2 for which steady uniform flow occurs [Pouliquen, 1999; Forterre and Pouliquen, 2008]. The lower angle ζ_1 is the angle below which a flowing granular material begins to slow down, whilst the upper angle ζ_2 is the angle above which the material will continually accelerate. In between these angles, the flow down an inclined plane has a constant steady velocity and a uniform height. In addition, a third angle exists, ζ_3 , which is the angle any stationary material must reach before it starts to flow [Pouliquen, 1999; Forterre and Pouliquen, 2008]. Interestingly, ζ_3 lies between ζ_1 and ζ_2 . This is a consequence of the fact that the friction coefficient of a flowing granular material is lower than that of a stationary one. Hence, a material can keep flowing even at angles below the angle of repose. Furthermore, if a flow becomes too shallow it will also stop flowing. Hence, for each inclination angle ζ a critical flow height $h_{stop}(\zeta)$ exists at which a granular material will stop flowing [Pouliquen, 1999].

The velocity profile of a dense granular flow depends on the flow geometry [GDRMiDi, 2004]. For inclined plane flows, which are the focus of this dissertation, the velocity typically follows the so-called Bagnold profile for thick layers, and varies with the depth to the power 3/2 [Bagnold, 1954; Silbert et al., 2001]. Whilst for thin layers, when the depth is close to the minimum thickness h_{stop} , the velocity profile is close to linear [Silbert et al., 2003; Rajchenbach, 2003]. Weinhart et al. [2012b] showed that the velocity profile for thick flows can actually be divided in three parts; a linear part near the bed and close to the free-surface, with a Bagnold scaling in between. When the flow becomes thinner, the Bagnold part is reduced, until the entire

velocity profile is linear.

2.3 Particle-Size Segregation in Dense Granular Flows

One of the unique properties of granular materials—dense or dilute—is their ability to sort particles based on their size, density, shape or frictional differences as a consequence of their movement. For size-segregation even small differences in the size-ratio can cause the grains to separate [Ottino and Khakhar, 2000; Stephens and Bridgwater, 1978a]. This occurs in flowing mixtures [e.g. Savage and Lun, 1988; Khakhar et al., 1999; Rognon et al., 2007] or those that are being shaken or vibrated [e.g. Knight et al., 1993; Rosato et al., 2002; Huerta and Ruiz-Suárez, 2004]. The research field of size-segregation can be divided in two distinct branches based on these two forms of mechanical agitation. The focus of this dissertation is on size-segregation in dense granular flows.

Size-segregation in dense granular flows typically takes the form of a vertical separation of large and small grains. Small grains are pulled down in the direction of gravity whilst large particles rise to the top of the flow. Depending on the flow geometry this separation has different end results. In rotating drums it gives rise to a small particle core surrounded by large particles [e.g. Williams, 1968; Baxter et al., 1998]. In heap flows it causes the large particles to accumulate at the outer regions [e.g. Gray and Hutter, 1997; Hill et al., 1999; Khakhar, 2011]. All such patterns of segregation are a consequence of the vertical separation of large and small particles during flow.

Opposing the process of segregation is particle diffusion or *diffusive remixing* as it is referred to in the context of segregation [Gray and Chugonov, 2006]. This of course concerns only diffusion along the direction of segregation because in other directions diffusion does not oppose segregation. Based on the relative strength of the amount of diffusive remixing, a granular mixture strongly or weakly segregates. The relative strength of diffusive remixing is captured by the segregation Peclet number [Gray and Chugonov, 2006].

2.3.1 Mechanisms for Size-Segregation

A number of different mechanisms have been proposed or identified to explain size-segregation for different forms of agitation [Williams, 1976; Schröter et al., 2006]. For dense granular flows it is generally accepted that the processes of *kinetic sieving* [Middleton, 1970; Savage and Lun, 1988] and *squeeze expulsion* [Savage and Lun, 1988] are the dominant mechanisms.

The process of kinetic sieving is explained as follows: As the particle mixture is sheared, the flow dilates and space is created in the grain matrix. Smaller particles are statistically more likely to move down into available space that opens up beneath them compared to large particles. Hence, the flow acts as a kinetic sieve that sorts the smaller particles downwards (i.e. in the direction of gravity). Although very similar, kinetic sieving is distinct from the process of

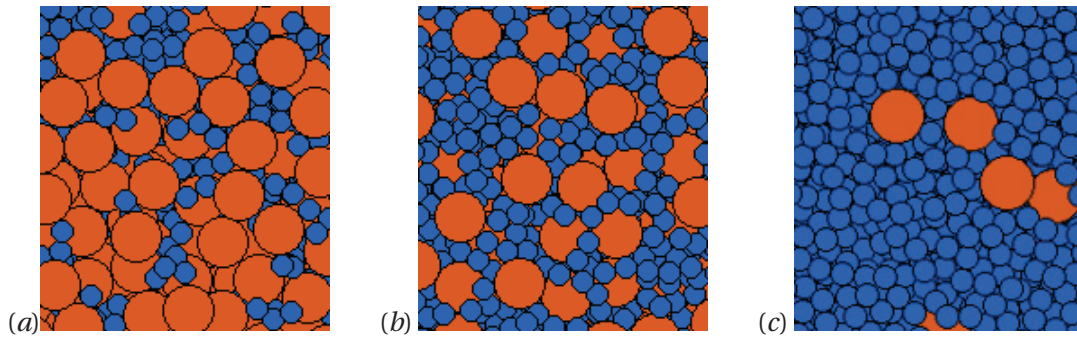


Figure 2.2: Kinetic sieving is easy to imagine when you consider the system in (a): plenty of space for small particles to fall into. The system in (b) has less space, but perhaps particles can still fall occasionally. But what happens in system (c)?

instantaneous or *spontaneous percolation*. Spontaneous percolation occurs when the size-ratio is bigger than 6.46 [Dodds, 1980]. In this case small particles are so tiny that they are able to fall through gaps in between large particles even without shearing the mixture [e.g Dodds, 1980; Bridgwater and Ingram, 1971; Bridgwater, 1994; Rahman et al., 2008]. An important aspect of spontaneous percolation is the fact that when the amount of small particles in the mixture is increased the percolation speed is reduced because the small particles are filling up the voids between the large particles and competing for the space to move down. Similarly, at lower size-ratio, when there is no spontaneous percolation, the process of kinetic sieving becomes less efficient when more small particles are present locally. The increased amount of small particles lowers the available space through which small particles can move down.

A different explanation for size-segregation is based on the kinetic stress associated with velocity fluctuations (known as granular temperature). This mechanism states that both small and large particles are driven towards regions of low fluctuating energy, but because small particles are more kinetic they are more effective at reaching this region through the process of kinetic sieving [Fan and Hill, 2011; Hill and Tan, 2014]. The important distinction between the mechanism described in the previous paragraph and the kinetic stress mechanism is that the pull of gravity is replaced by a force that drives particles to regions of lower granular temperature.

The process of kinetic sieving is easy to verify when studying segregating mixtures: One simply observes how small particles fall or bounce into the space between large particles. The rising of large particles is much less easily observed. To explain why large particles move up the mechanism of *squeeze expulsion* was proposed by Savage and Lun [1988]. This mechanism, as initially described by Savage and Lun, states: “[...] as a result of the fluctuating contact forces on an individual particle, there can occur force imbalances such that a particle is ‘squeezed’ out of its own layer into an adjacent one if an opening is available or the force imbalance is sufficiently large. This mechanism is not gravity driven and it is supposed that it is not size preferential.” It is important to note that the idea of squeeze expulsion in its original

form applies to both the small and large particles. But since the kinetic sieving mechanism promotes downward movement of small particles the end result is a net upward movement of large particles.

Since its first introduction, the meaning and interpretation of the processes of squeeze expulsion has been changed and modified in various works. This is a strong indication as to the qualitative nature of these mechanisms. Since there is little quantitative data or fundamental understanding, different interpretations exist. Some variations are:

- Kinetic sieving allows small particles to move down. In turn, these small particles push the large particles up.
- Kinetic sieving allows small particles to move down and as a result of the constant solids fraction throughout the flow the large particles are forced upwards.
- Kinetic sieving allows small particles to move down. Simultaneously, force imbalances, lever/squeeze large particles towards the surface.

The process of kinetic sieving, whether driven by gravity or kinetic stress, seems at first hand difficult to argue with when thinking of a small particle surrounded by many large particles, such as shown in Figure 2.2(a). It is however put to the test when considering a mixture where relatively more small particles are present compared to large particles and space is limited, as shown in Figure 2.2(b). In the extreme case when only a few large particles are present, as in Figure 2.2(c), it is hard to imagine space opening up in the grain matrix for small particles to move into.

2.3.2 Theory and Modelling of Size-Segregation

One could say that the theoretical developments in the field of size-segregation in dense granular flows far surpass the experimental developments. Theoreticians have taken what limited understanding we have of size-segregation and developed a range of continuum models [e.g. Savage and Lun, 1988; Dolgunin and Ukolov, 1995; Gray and Thornton, 2005; Fan and Hill, 2011; Marks et al., 2012; Tunuguntla et al., 2014; Schlick et al., 2015]. In recent years most of the developments centre around an approach based on mixture theory [Morland, 1992]—first introduced to the size-segregation community by Gray and Thornton [2005]—where every point in space is simultaneously occupied by all particle species.

The mixture-theory framework has proven well suited for modeling size-segregation and has been generally embraced. The models using this framework are based on an advection diffusion equation incorporating a segregation flux which drives different particle species in different directions. This segregation flux is formulated based on the assumption of stress partitioning between the different species. If the driving force behind the segregation is thought to be kinetic stress, the partitioning is done such that small particles carry more of the

kinetic stress than their local concentration. If the driving force is thought to be gravity, the contact stress or pressure is partitioned such that small particles carry less of the pressure than their local concentration. In simulation studies it has been found that the former assumption is true whilst the latter is not [Weinhart et al., 2013; Hill and Tan, 2014; Staron and Phillips, 2014; Tunuguntla et al., 2016]. It is unclear, however, whether the confirmation of a kinetic stress partitioning in simulations, instead of a contact stress partitioning, suggests that gravity is not a driving force for segregation. It is not unreasonable to argue that both gravity and temperature gradients can set the direction for the segregation, and that subsequently, the more kinetic small particles more easily travel in the direction of the gravitational pull or a lower temperature region.

2.4 Terminology

Unless explicitly mentioned as otherwise “segregation” always means “size-segregation”. Similarly “dense granular flows”, “granular flows”, “dense shear flows”, or any other variation are used interchangeable but all refer the same type of flow. Furthermore, “concentration” and “volume fraction” are used intermittently, but always refer to the small-particle volume fraction, ignoring the inter-particle void space.

3 Methods and Techniques

“I’ve missed more than 9.000 shots in my career. I’ve lost almost 300 games. 26 times I’ve been trusted to take the game winning shot and missed. I’ve failed over and over and over again in my life. And that is why I succeed.”

– Michael Jordan

THIS chapter discusses the techniques and methods that are used in the studies described in this thesis. First, the experimental imaging technique *refractive index matched scanning* (RIMS) is explained, followed by a short outline on the approaches used for particle detection and tracking. Then the experimental geometries are discussed and the geometry specific implementation of RIMS. This is followed by a more detailed discussion on the design and construction of one of the geometries: the moving-bed channel. Next, the numerical simulations are discussed. The chapter ends with a short section devoted to the parameters for the experimental and simulation work.

3.1 Experimental Techniques

3.1.1 Refractive Index Matched Scanning

Measuring the particle-scale motion in a 3D granular material is not straightforward. The material is usually opaque and even when it does consist of transparent grains incoming light will be refracted inside the mixture. As a consequence, individual grains are only visible on the surface of the material. To overcome this challenge, several techniques have been developed to visualize the interior of 3D granular materials, such as magnetic resonance imaging (MRI) [Nakagawa et al., 1993], x-ray tomography [Wang et al., 2004], confocal microscopy [Brujić et al., 2003] and positron emission particle tracking (PEPT) [Parker et al., 1997]. The imaging technique used in the experimental studies presented in this thesis is refractive index matched scanning (RIMS) [Wiederseiner et al., 2011a; Dijkstra et al., 2012]. The advantages of RIMS over the aforementioned techniques are: a relatively lower cost; ease

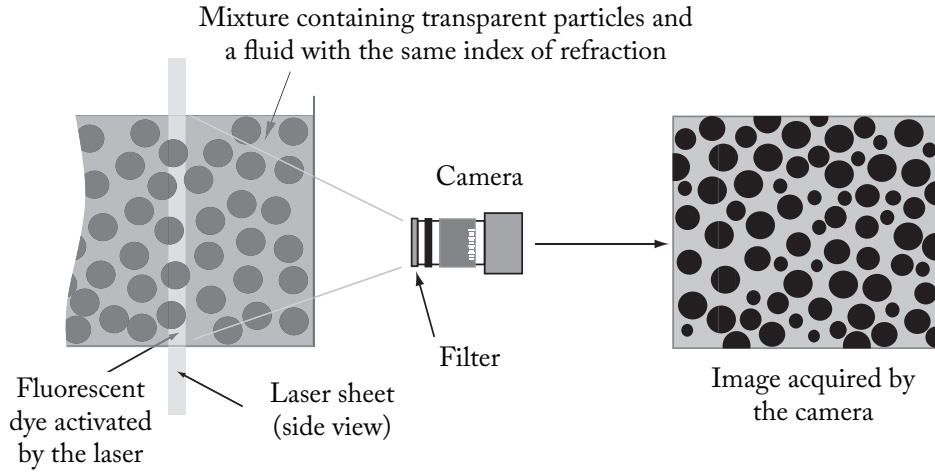


Figure 3.1: Schematic of the RIMS technique. A mixture of transparent spherical grains is submerged in a liquid of the same refractive index as the grains. As a consequence the mixture becomes transparent. By adding a fluorescent dye and exciting this dye in a narrow plane with a laser sheet a cross-section of the mixture becomes visible. This cross-section can be imaged using a camera to obtain images with dark disks on a bright background. A filter in front of the camera blocks out the laser light and only permits the light emitted from the dye to reach the camera. Image adapted from [Andreini, 2016].

of tracking multiple particles; and the possibility of using macroscopic particles, which is not an option with confocal microscopy.

The principle of RIMS is illustrated in Figure 3.1. The main idea consists of matching the refractive index of the granular material of interest with that of an interstitial fluid. If done correctly a granular mixture made up of transparent grains will become transparent as a whole, i.e., invisible in the fluid. An example of this effect is shown in Figure 3.2. If a fluorescent dye is added to the fluid, a laser sheet at the right wavelength can illuminate a planar cross section within the granular material, which can then be captured by a camera. Since only the fluid emits light—the dye is not inside of the particles—the image obtained will contain dark disks on a bright background, as shown in the example in Figure 3.2. The laser sheet can be moved to obtain a ‘scan’ of cross sections of the granular mixture. This set of images is used to construct the 3D positions of the particles in the mixture.

In order to successfully apply RIMS, i.e., to obtain the highest quality and most accurate images, a number of aspects need to be carefully considered. A precise matching of the refractive index n_f of the liquid and material n_p is required, taking into account fluctuations in temperature, which change the value of n_f , and the inertness of the liquid, i.e., does the liquid evaporate, un-mix or change in other ways over time? In addition, any dirt, dust or other unwanted material should be prevented from entering the RIMS liquid because it can change the value of n_f . The quality of the laser sheet is also critical: it has to be thin relative to the particle size, in order to sharply cut the cross-section. If the laser sheet is too thick, the

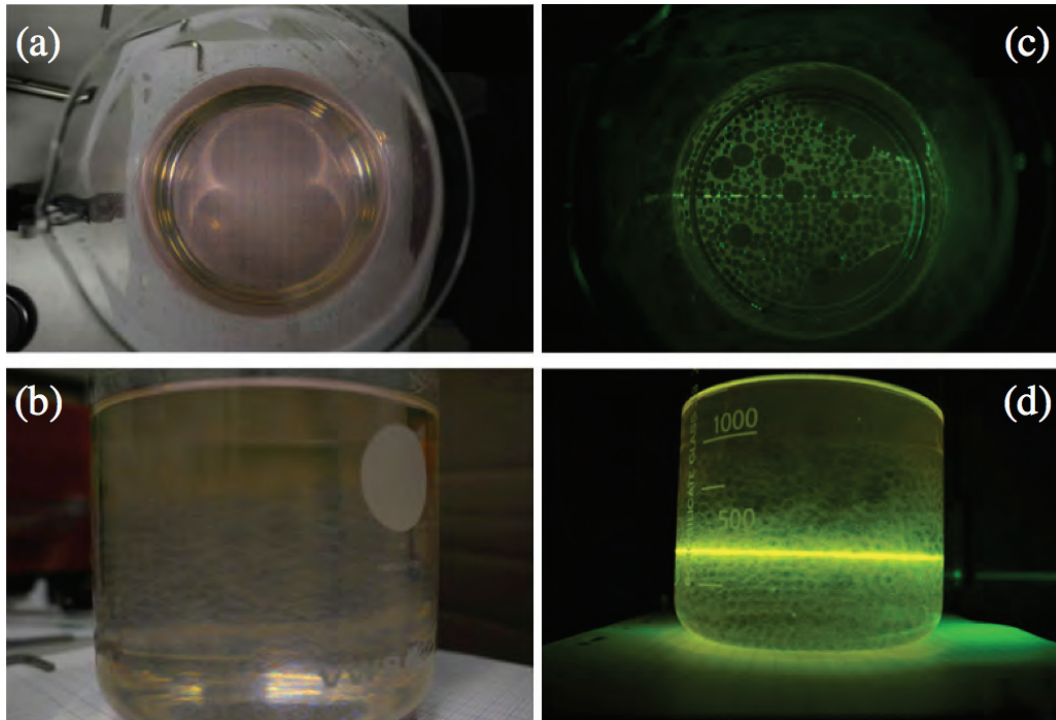


Figure 3.2: An example of the effect of refractive index matching and exciting a fluorescent dye in the mixture with a laser sheet. (a–b) This cup contains borosilicate beads and a liquid that is index matched. One can easily see the lines on the paper below the cup. (c–d) Here the same cup is illuminated with a laser sheet. The fluorescent dye is excited and emits light from within the cross-section.

edges of the dark disks on the image will be blurred.

Ideally the presence of the fluid should not change the behavior of the granular material. Otherwise, the system is no longer a purely ‘dry’ granular system, but rather some form of dense suspension. The presence of a fluid affects the interstitial pore pressures, but also couples the stress carried by the particles to that carried by the fluid [Iverson and LaHusen, 1989; Iverson, 1997, 2005]. This coupling is particularly strong in unsteady flows, where local changes in the particle volume fraction allow large excess pore pressures to develop, which in turn influence the grain motion [Muite et al., 2004; du Pont et al., 2003a; Pailha et al., 2008; Pailha and Pouliquen, 2009]. However, for steady dense granular flows, it is expected that due to the large number of particle-particle contacts the frictional interactions are still dominant in determining the rheological behaviour even when an interstitial fluid is present [Anciae et al., 1999]. Cassar et al. [2005] showed that, in steady flows submerged in water, at least 75% of the overburden pressure is borne by the contact network. They also showed that the same rheology used to describe dense steady flows in air [GDRMiDi, 2004] also applies to immersed flows, with the interstitial fluid changing the time-scale of the particle rearrangements. This is consistent with the experimental results of Vallance and Savage [2000] and the theory of Thornton et al. [2006] who both showed that adding an interstitial fluid to flows containing

different sized constituents is to reduce segregation rate. Effectively, the addition of a fluid lowers the particle density, and thereby the segregation rate. One must be careful, however, if the fluid is too dense compared to the particles, or if the viscosity is too high, fluid inertial effects can easily disturb the segregation process.

3.1.2 The RIMS Technique Applied

The RIMS technique is used in the experimental studies described in Chapters 4 and 5. The experimental geometries that are studied using the technique are discussed in Section 3.2 and the geometry dependent details of the RIMS technique are discussed in Section 3.2.2 and Section 3.2.4.

In all experiments the index-matched liquid is a mixture of benzyl-alcohol and ethanol. The combination of which results in a RIMS liquid with viscosity $\mu_{RIMS} = 3 \text{ mPa s}$ and density $\rho_{RIMS} = 995 \text{ kg m}^{-3}$. The particles used are made of borosilicate glass with a density of $\rho_p = 2230 \text{ kg m}^{-3}$ and a refractive index $n_p = 1.473$. This combination of materials has the advantage of a low viscosity fluid and large density ratio and is the main reason for choosing this exact combination in favor of others, for instance, PMMA particles in combination with Triton X-100 ($\mu = 270 \text{ mPa s}$). The parameters of our RIMS liquid ensure that the Stokes number $\gg 1$ [Batchelor, 1989; du Pont et al., 2003b], hence fluid drag forces are small compared to both gravitational forces and the forces due to shear. In order to maintain an accurate matching between n_f and n_p the temperature of the room is controlled and held at $18^\circ\text{C} \pm 0.2$.

The fluorescent dye that is added to the RIMS liquid is Rhodamine 6G, which has its peak excitation wavelength at 528 nm and peak emission wavelength at 553 nm. The laser sheet is created with a 4 Watt diode pumped solid state laser with a wavelength of 532 nm. The difference between the wavelength of the laser and the emission of the dye is of practical use because it allows us to filter out the light from the laser and only capture the emitted light. The laser sheet is created using a rod lens or a laser line generator lens. The advantage of the latter is a constant intensity profile over the entire length of the sheet, contrary to the gaussian profile created by a rod lens. The sheet is focussed using a combination of two convex lenses with a focal length of 120 mm and 90 mm. The 120 mm lens focusses the beam just before the 90 mm lens, subsequently the 90 mm lens focusses the diverging beam again resulting in a beam that has a constant minimal thickness over a range of approximately 20 cm at a distance of roughly 50 cm from the two lenses.

3.1.3 Image Analysis and Tracking

The reconstruction of 3D particle positions and radii based on a set of 2D cross-sections is a complex process. Indeed, independently of the type of experiment or the granular mixture the RIMS technique provides the experimentalist with grayscale images with dark disks on top of a bright background. However, from here onward there exists no method for detecting circles

or spheres that does not require a significant amount of customization. There are various algorithms that can be used to find circles and spheres in this context. These techniques include convolution [Haralick et al., 1987], Hough transforms [Ballard, 1981], and watershed algorithms [Gauch, 1999]. All such algorithms work almost flawlessly only if the correct image is supplied: a high contrast image with homogenous brightness where the shapes are near perfect discs, have sharp boundaries and do have minimal overlap. The raw images obtained by the RIMS technique require significant pretreatment in order to approach this requirement. Our pretreatment consists of a combination of different steps of brightness correction, contrast enhancement, thresholding, and different morphological operations (erosion, dilation, etc.). The result is a binary image that can be supplied to the particle finding algorithm.

For the studies reported in this thesis different particle finding algorithms have been tested and used throughout the duration of the work. The method of convolution [Franklin and Shattuck, 2016] is used to obtain disk radii and center positions. Based on these data the center and size of the particle could be constructed using simple geometrical calculations. A much slower but more robust method is 3D convolution, which I use to find particle centers and radii directly [Crocker and Weeks, 2000]. Another method that was developed in-house consists of shrinking the disks to dots in order to find their center. The dots form strings in 3D space perpendicular to the imaging plane. The center of the string corresponds to the particle position and the particle radius is related to the length of the string. This method is extremely fast and although the 3D convolution method should be more accurate, with our image quality the accuracy was comparable.

Note that the experimental work discussed in Chapter 5 does not use RIMS to obtain 3D scans, only 2D images are recorded. Hence I use 2D convolution and Hough transforms to obtain disk radii and positions.

Determining the movement of particles between different time-steps is done via particle tracking algorithms. The challenge of particle tracking is not to lose particles or switch their identity. Two different approaches are used for the studies presented in this thesis. For the tracking of disks on 2D images in Chapter 5 the voronoï tracking algorithm of Capart et al. [2002] is used. This algorithm has two parameters for tracking: (1) the distance between a particle at time t and $t + 1$ and (2) the change in the local voronoï diagram based on the Delaunay star that is centered at each particle. A threshold is set for the maximum displacement and the maximum change in the Delaunay star. The advantage of this algorithm is that works well for the relatively fast flow that is studied in Chapter 5.

For the tracking of particles in 3D in Chapter 4 I use the Hungarian algorithm [Kuhn, 1955]. The Hungarian algorithm is a combinatorial optimization algorithm that solves the assignment problem—matching particles between subsequent time-steps—by minimizing cost. The cost in this case is the displacement. The algorithm tries to find the best way to associate all particle positions at time t with all particle positions at time $t + 1$ by minimizing the distance covered by each particle. This is not the same as a nearest neighbor search since all particles

are considered together in this optimization. Consequently, it is not necessarily so that each particle at t is matched to the nearest particle at time $t + 1$. Indeed, I find that the results of the algorithm are a significant improvement with respect to a simple nearest neighbor search.

3.1.4 Complications and Uncertainties

RIMS is a delicate technique. Slight imperfections in the index-matched system can significantly reduce the image quality, thereby making it impossible to accurately determine particle positions. In our system, the quality of index-matching was reduced by: (1) the particles having a slightly different index of refraction at their surface; (2) evaporation of ethanol; (3) dust in the fluid. Evaporation and contamination of the RIMS liquid was reduced by covering the experiments, having as little available space above the fluid and saturating the available space with ethanol in gas form. Before each experiment the liquid is cleaned and the index-matching is redone.

Unfortunately the problem with the surface of the particles could not be completely solved. Particles smaller than 4 mm had significant surface defects in the form of air bubbles, making them unusable. Particles of 4 mm and larger had no air bubbles near the surface, but the surface still had a slight difference in the index of refraction.

3.2 Experimental Geometries

The experimental flow geometries used in the studies presented in this thesis are the *moving-bed channel* and the *shear-box*. This section will discuss these geometries and their specific RIMS implementation. Because the design and construction of the moving-bed channel posed significant challenges its design process is discussed in detail in the next section.

3.2.1 Shear-box

The shear-box consists of a narrow rectangular box, with transparent front- and back-walls and Polyoxymethylene (POM) side-walls. These side-walls are special in that they can incline whilst remaining parallel. The inclination of the side-walls applies a linear shear to the mixture. Typically a continuous back and forth motion is applied to the walls, which results in an oscillating sinusoidal linear velocity profile. A schematic of the shear-box geometry and the applied velocity field is shown in Figure 3.3(a). The width between the oscillating walls is 37 mm, the width between the front- and back-walls is 51 mm, and the height is 90 mm.

Two slightly different shear-box geometries are used. The difference being the position of the rotation axis around which the oscillating walls tilt. In the first shear-box design, shown in Figure 3.3(a), the axis is at the bottom end of the wall. This placement of the axis creates a 2 mm dead-zone where no shear is applied. In the second setup, the axis is placed at a higher position, as shown in the schematic in Figure 3.3(b). This modification results in linear shear

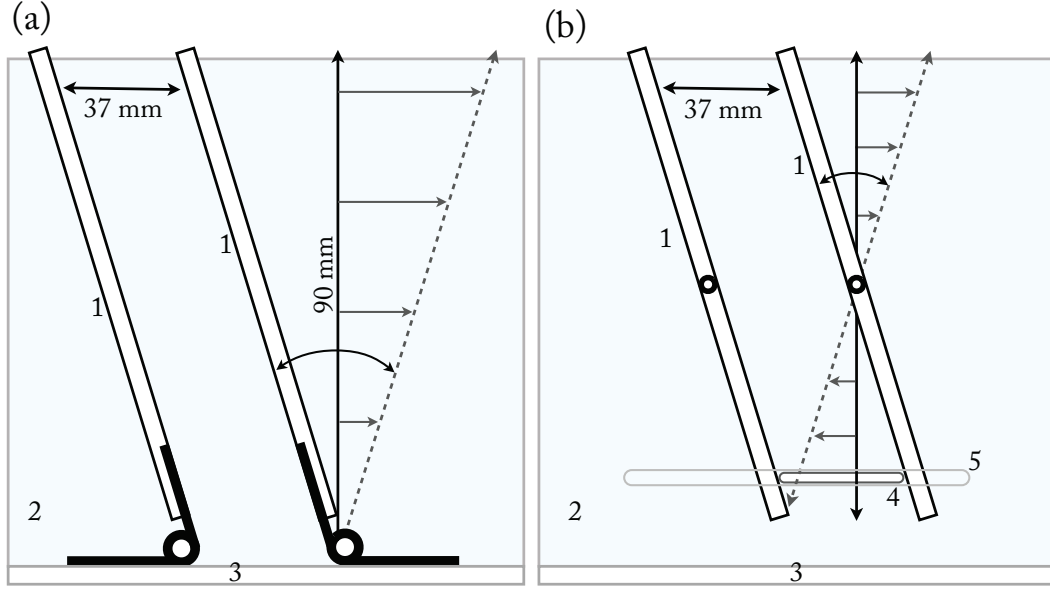


Figure 3.3: Schematics of the two shear-box geometries that are used. (a) Traditional shear-box with rotation point at the bottom. (b) Improved shear-box with rotation point midway. The numbers indicate: (1) Side-walls made of Polyoxymethylene (POM); (2) Front- and back-walls made of glass; (3) Bottom-wall made of glass; (4) Additional glass bottom-wall; (5) Groove in the glass side-walls through which the additional glass bottom-wall (4) slides. Not depicted: the connection between the top of the oscillating side-walls and the driving motor.

all the way to the bottom of the shear-box.

Through their oscillation the side-walls apply a periodic shear $\gamma(t) = \gamma_0 \sin(\omega t)$. An oscillation cycle starts with the sidewalls straight, i.e., an inclination angle $\theta = 0^\circ$, the walls are then displaced towards the left to the maximum angle θ_{max} , subsequently towards the right to θ_{max} , and finally back to the center at $\theta = 0^\circ$. The shear rate is given by $\dot{\gamma}(t) = \gamma_0 \omega \cos(\omega t)$, the frequency by $\omega = 2\pi/T \text{ rad s}^{-1}$, and the strain amplitude by $\gamma_0 = \tan \theta_{max}$, with T the oscillation period for a cycle. The maximum grain displacement amplitude is $A = h\gamma_0$, where h is the flow depth.

The shear-box was first used by Bridgwater and co-workers [Scott and Bridgwater, 1975, 1976; Stephens and Bridgwater, 1978a,b] to study particle-size segregation. This was a long time ago and the setup has only been used sporadically since [Tang et al., 2002; Johanson et al., 2005]. It is not clear why this configuration is so much less used compared to similar geometries that enforce the flow through the movement of side-walls, such as the couette [Forterre and Pouliquen, 2008] or split-bottom [Dijksman and van Hecke, 2010] geometries. The reason for the use of the shear-box geometry in the studies presented here is that it lends itself excellently for the study of particle-size segregation. Size-segregation occurs readily in gravity-driven flows and the linear shear profile applied by the shear-box comes close to this situation. The linear shear profile gives rise to a constant shear rate along the depth of the flow. This is

important for our investigation because it removes any shear gradient dependencies in the segregation flux. In addition, size-segregation manifests itself predominately in the vertical direction—the separation of constituents takes place in the vertical direction—making the narrow and high shear-box geometry well suited. Temperature gradients, however, can still be present in the shear-box, arising from the lithostatic pressure. Fortunately, these can be expected to be very small if a very low shear-rate is used.

3.2.2 Shear-box RIMS Implementation

The implementation of RIMS in the shear-box is illustrated in Figure 3.4. The entire setup is submerged in an aquarium and lit from the bottom with a laser sheet perpendicular to the oscillating walls. The laser and lenses are attached to a stepper motor that moves them back and forward in order to scan the mixture. Two Basler A406k camera's equipped with orange filters are used to image the mixture. A problem that arises with RIMS is that image quality is reduced the further the emitted light has to travel through the mixture. This is a consequence of imperfections in the index-matched system that diffuse the light. In order to improve image quality one camera records images for one half of the mixture, whilst the second camera records the other half. The camera's switch recording when the laser sheet

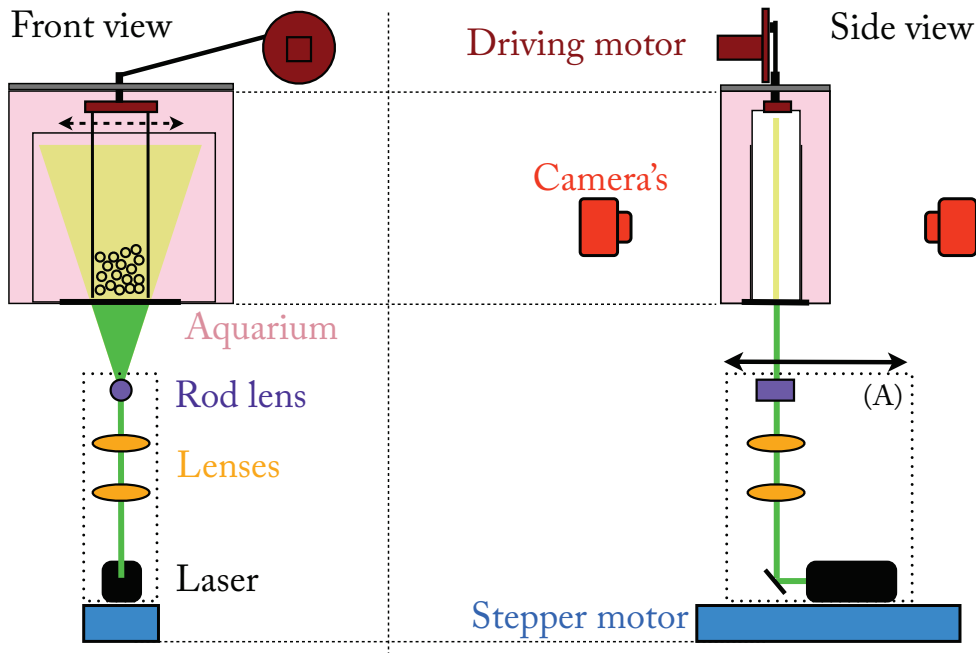


Figure 3.4: A schematic of the RIMS implementation with the shear-box geometry. On the left is a front view and on the right is a side view. The shear-box is submerged in an aquarium filled with the RIMS liquid. A laser sheet is directed at the mixture from the bottom. The mixture is imaged from the front with one camera and from the back with another camera. Section (A) containing the lenses and the laser is moved by a stepper motor in order to scan the mixture.

crosses the center of the mixture. This modification allows us to keep the camera's stationary, which significantly reduces the complexity of the setup. If the mixture is very thick and a single camera is used the camera has to be moved to remain focussed on the position of the sheet. Since in our situation the thickness of the mixture that is imaged by each camera is no more than 25 mm, and I focus the camera in the center of this region, the reduction in sharpness of the images is negligible compared to other effects. In other words, the gain in image quality due to the use of two camera's is more than the loss in quality due to their fixed position.

3.2.3 Moving-bed Channel

In a moving-bed channel the bottom layers of the flow are dragged upslope by a moving conveyor-belt, whilst the top layers avalanche downslope as result of gravity. On all four sides the flowing mixture is contained by walls in order to prevent it from flowing out of the channel. Figure 3.5(a) illustrates the difference in the velocity profile parallel to the bed between the flow in a normal inclined channel and in a moving-bed channel: the velocity profile in the moving-bed channel is shifted by the belt velocity.

The moving-bed channel was first used by Davies [1990] for the study of debris flows. It was later used by Armanini et al. [2005], Leonardi et al. [2015] and Mahapatra et al. [2016] to study granular flows and by Chambon et al. [2009, 2014] for the study of dense viscoplastic fluids. A variation on the moving-bed channel is a rotating drum with a very small amount of material as was used by Kaitna and Rickenmann [2007]. This gives a more complex flow profile as a result of the curvature of the drum, but has in general the same effect. The advantage of a moving-bed channel over a conventional channel is that it allows the study of granular flow

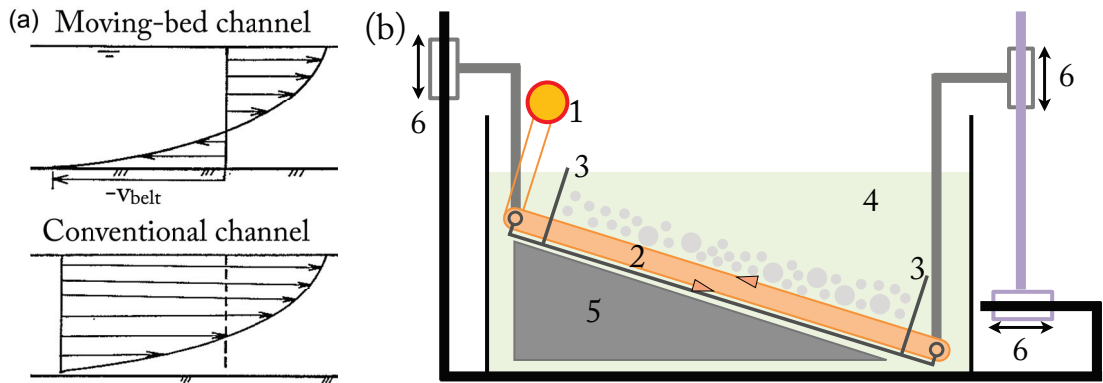


Figure 3.5: (a) Schematic showing the general change in velocity field between a conventional channel and a moving-bed channel. The velocity field in the moving-bed channel is shifted to the left with the belt velocity. Image adapted from [Davies, 1990]. (b) A schematic of the moving-bed channel submerged in the aquarium. The numbers indicate: (1) the motor; (2) the belt; (3) the upper and lower wall that keep the granular mixture in the channel; (4) the aquarium filled with RIMS liquid; (5) a plastic box that lowers the total volume of RIMS liquid in the aquarium; (6) The inclination of the belt is changed by sliding along these points. Image courtesy of J.-L. Pfister.

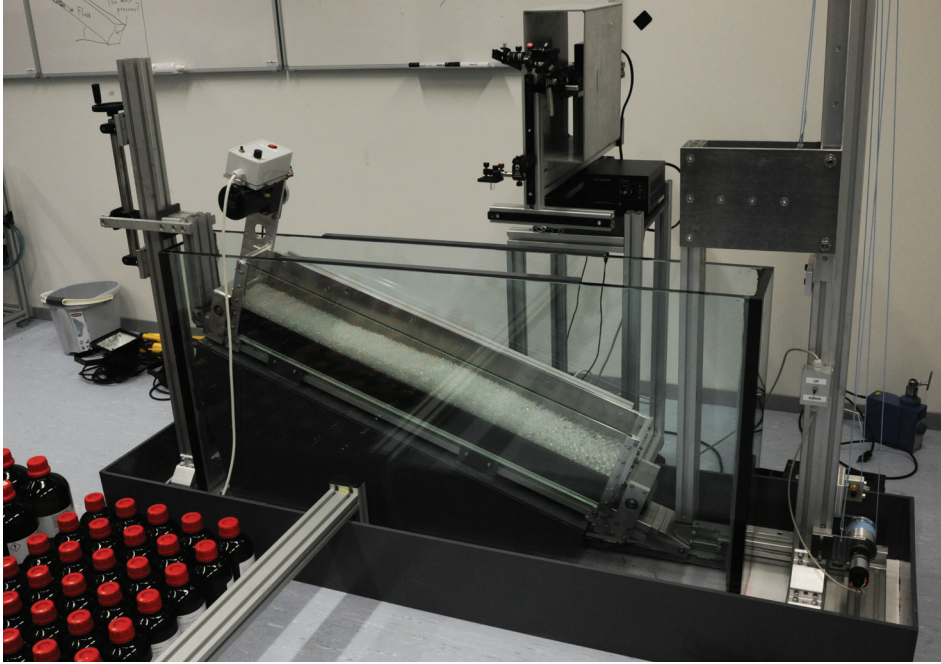


Figure 3.6: A photograph of Channel A. See the schematic in Figure 3.5(b) for details. Image courtesy of J.-L. Pfister.

driven by gravity for long periods of time. In a typical channel the duration of the experiment is only as long as the channel is long. With a moving-bed channel a gravity driven flow can be studied indefinitely. This feature makes the moving-bed channel the most practical way to study *breaking size-segregation waves* as will be explained in detail in Chapter 5.

Two moving-bed channels have been constructed during the work done for this thesis. I will refer to them as Channel A and Channel B. Channel A is a prototype, which nonetheless has been used to obtain the results discussed in Chapter 5. Channel B has a number of improvements over Channel A but is still under construction at the time of writing. Figure 3.5(b) shows a schematic of Channel A and Figure 3.6 shows a photograph. Figure 3.8 shows a photograph of Channel B. In the schematic of Channel A the setup is submerged in an aquarium in order to use it in combination with RIMS, as will be explained in the next section. The channel can be inclined from 0° to 25° . At the top and bottom ends of the channel gates are positioned. The belt moves underneath these gates whilst the granular material is blocked. The channel length is 104 cm and its width is 10 cm. The side-walls and gates rise 15 cm above the bed. One of the side-walls is transparent to allow imaging. The belt speed can be varied continuously from 14 mm s^{-1} to 242 mm s^{-1} .

Depending on the inclination angle of the channel and bed velocity the flow depth along the channel varies. After setting an inclination and bed velocity the flow depth evolves until the upstream and downstream mass flow rates are balanced. The result can be a uniform depth

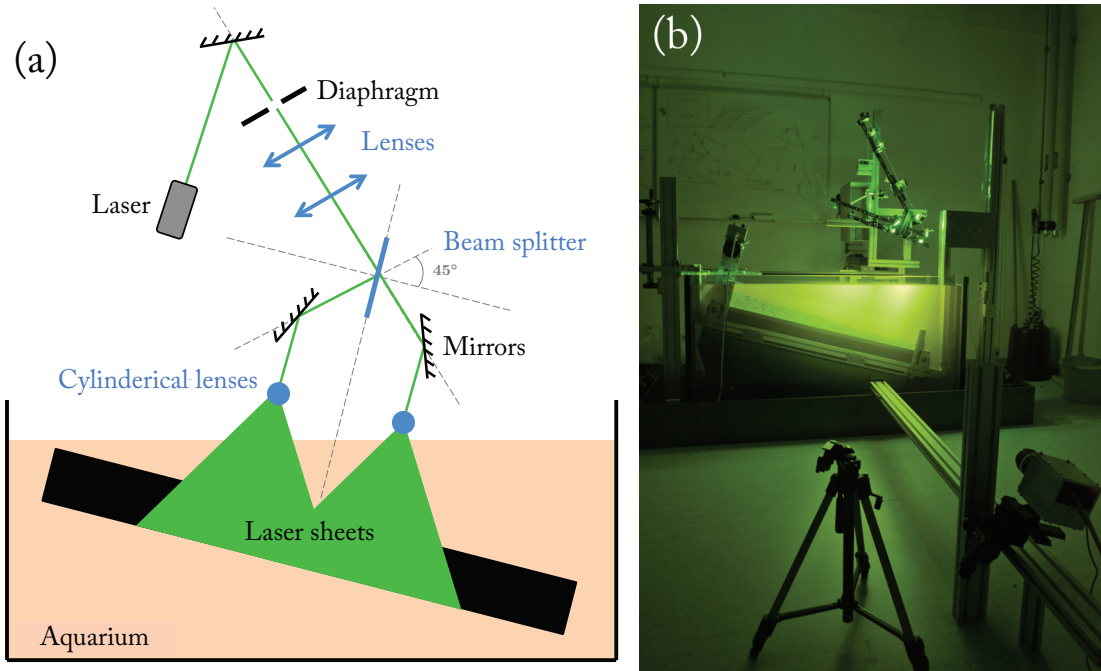


Figure 3.7: (a) A schematic of the laser setup for the moving-bed channel. (b) A photograph of the setup in the lab. Both images are courtesy of J.-L. Pfister.

along the length the channel, or a higher depth in the upslope part and a lower depth in the downslope part, or vice-versa. A higher inclination requires a higher bed velocity to maintain a uniform flow height.

3.2.4 Moving-Bed Channel RIMS Implementation

Figure 3.7 shows a schematic and photograph of the laser implementation on Channel A. The entire channel is submerged in an aquarium filled with RIMS liquid. The volume of the aquarium is approximately 200 liter. In order to reduce the required volume of RIMS liquid a large plastic box is attached to the bottom of the belt, as shown in the schematic in Figure 3.5 (b). Two laser sheets are installed in order to visualize a large part of the flow. The two laser sheets are created from a single laser source using a beam splitter and two cylindrical lenses. The beam is split after the convex lenses, which simplifies the implementation. The two beams are directed at two rod lenses via mirrors in order to create two laser sheets. The sheets are positioned perpendicular to the bed in the center of the flow. Since the flow in the experiments conducted with this setup is continuous no scanning is performed and the sheets are fixed. A Basler A406k camera is used to image the flow through the glass side-wall of the setup.

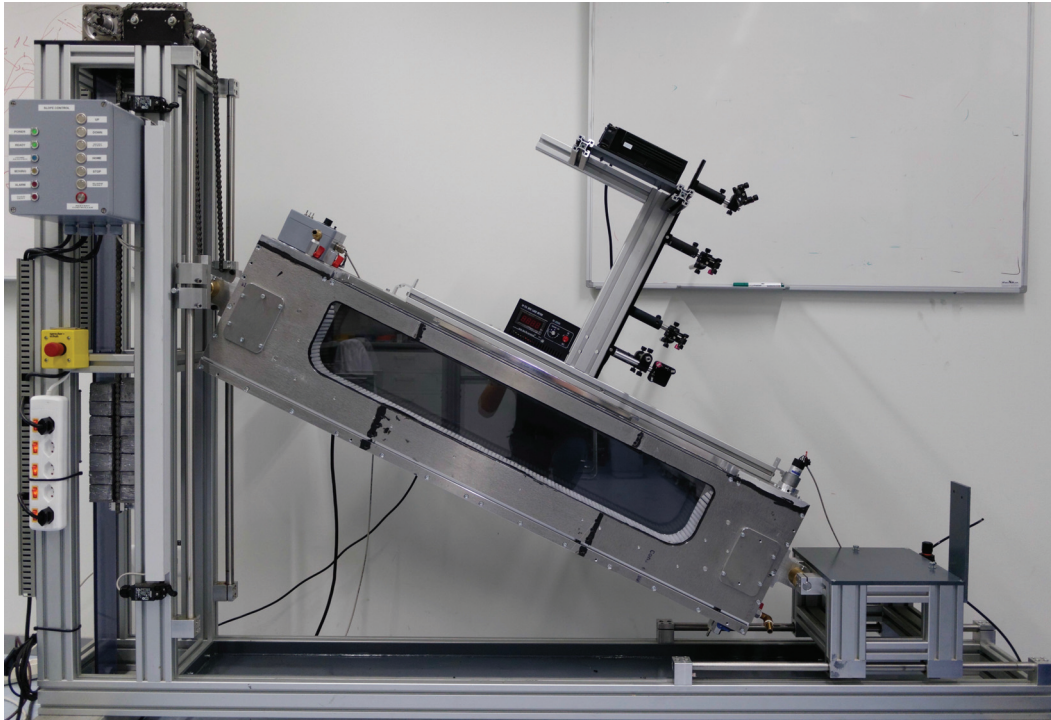


Figure 3.8: A photograph of Channel B mounted on the carriage to facilitate a change in inclination. See the text for details.

3.2.5 Design Challenges of the Moving-Bed Channel

One of the primary endeavors for this thesis is the design and use of a moving-bed channel in combination with RIMS in order to study the phenomenon of breaking size-segregation (BSS) waves [Gajjar et al., 2016; Thornton and Gray, 2008]. In general, the design and construction of a moving-bed channel is in and of itself not a straightforward task, but it has been proven to be possible [Davies, 1990; Armanini et al., 2005; Leonardi et al., 2015; Mahapatra et al., 2016; Chambon et al., 2014]. The RIMS technique is well documented [Dijkman et al., 2012; Wiederseiner et al., 2011a] and the Environmental Hydraulics Laboratory is a pioneer in the technique. However, the combination of these two techniques poses new challenges. On top of this, the phenomenon that we want to study, the BSS wave adds a number of additional requirements.

The specifics of Channel A have been discussed in the previous sections. Here I outline the design challenges of this setup and the solutions to these challenges that we have implemented in its successor Channel B.

1. BSS waves are very long with respect to their flow depth. Typically the flow length has to be 20 to 30 times the flow depth in order to fully realize the wave (see Chapter 5). Both the mechanical nature of the moving-bed channel and the use of the RIMS technique

put a lower limit of several mm on the particle size. Hence, with a particle size of 8 mm for the large particles and 4 mm for the small particles, a flow depth of 8 large particles requires a minimal flow length of 160 cm. Knowing that the BSS wave will stretch over roughly 80% of the flow length makes this a very big system to construct and to visualize using RIMS.

2. The channel needs to be submerged in a RIMS liquid. Given the flow length requirements and the fact that the channel will be inclined (see the schematic in Figure 3.9(a)), a large aquarium is necessary, containing close to two-hundred liters of RIMS liquid. This will make the preparation of the RIMS liquid and maintaining its quality very challenging.
3. If the setup is submerged in an aquarium and inclined, as depicted in Figure 3.9(a), the laser sheet will have to be directed at an angle with respect to the fluid free-surface in order to be perpendicular to the granular mixture surface. This will result in loss of energy due to reflection. Moreover, the laser sheet will travel a long distance through the fluid before reaching the granular flow, which, as a consequence of diffusion, reduces the thinness of the laser sheet and the quality of the images obtained through RIMS.
4. The gates that are positioned at the upslope and downslope ends of the channel, to block the flowing mixture from moving off the belt, impose a strict relation between the bed roughness, particle size, gate height and amount of slip between the bed and the mixture. Let us assume a gate height and bed roughness such that the bed perfectly fits underneath the gate. If particles are too small with respect to the bed roughness, they will move underneath the gate or get stuck under it. On the other hand, if particles are bigger the roughness of the belt might not be sufficient and the material will slip. Since the goal is to study a bidisperse mixture with a size ratio of around 2.0, the small particles are either too small, or the large particles too big and slip of the large particles seems unavoidable. Moreover, a BSS wave separates the large particles from the small particles horizontally along the length of the channel. The pure phase of large particle will experience significant slip with the bed, as discussed in Chapter 5.
5. All components of the channel need to be resistant to the RIMS liquid. Because of the use of benzyl-alcohol and ethanol most soft rubbers, plastics, glues and sealants are prohibited. This severely limits the options for the belt material, which has to be strong and flexible such that it can bend around an axis.
6. The conveyor-belt is driven by rotating axes. In a dry situation, with a rubber belt, friction is enough to transfer a force from the axes to the belt. In our situation, where the setup is submerged, slip can occur between the axes and the belt because of fluid lubrication.

Except for point 5 and 6, all of these challenges became clear to us only after testing with Channel A. As such nearly all of the solutions described below are implemented in Channel B.

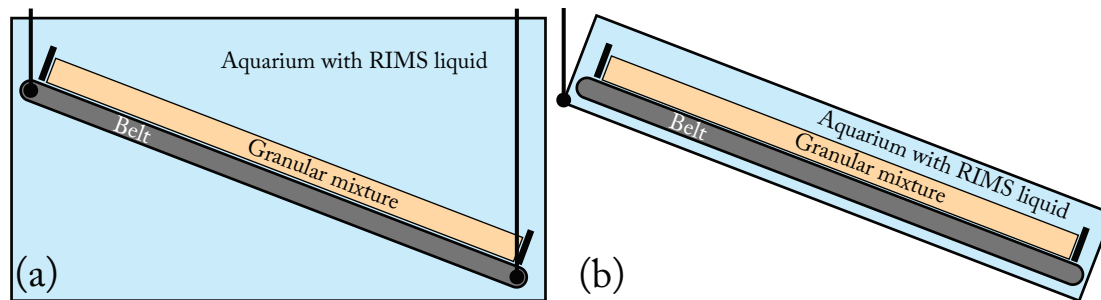


Figure 3.9: (a) Channel A submerged in an aquarium with RIMS liquid. This is a simple solution, which unfortunately brings with it a host of challenges, namely; a large amount of liquid, which is difficult to control and accurately tune for RIMS; the laser sheet needs to travel to a large amount of liquid before it reaches the particle mixture, which, as a consequence of diffusion, reduces the thinness of the sheet. (b) Channel B with the aquarium build around the channel. This solution has a number of advantages, however its construction and design is much more challenging.

Challenge 1. Our study of the physical behavior of BSS waves (discussed in Chapter 5) indicates that their length scales with the flow depth and the segregation rate. Hence, the length scales indirectly with the size-ratio of the particles in the mixture, because the size-ratio effects the segregation rate. These parameters need to be balanced with a desire to have a system that is physically interesting. For example, reducing the flow height to the size of a single large particle decreases the length of the BSS wave, but it creates a system that can no longer be considered a dense granular flow. A length of 100 cm was chosen for Channel B. A longer channel would have been better in light of the above, but production time, structural strength requirements and financial cost of the setup put an upper limit on the length.

Challenge 2 and 3. A solution to the requirement of large quantities of RIMS fluid is to build the aquarium tightly around the channel instead of submerging the channel in an aquarium. This is illustrated in Figure 3.9(b). Both challenge 2 and 3 are addressed by this solution, but challenge 4 becomes more difficult to meet, because the entire channel now has to be water-proof. A sealant is required that is not destroyed by the RIMS liquid. Another major advantage of having the aquarium around the channel is that it can be hermetically sealed and thereby prevent evaporation of ethanol from the RIMS liquid or any contamination.

Challenge 4. The challenge concerning the gate height, particle size, bed roughness and slip, is addressed by removing the gate altogether and having the belt curve upwards, as shown in Figure 3.10(a). I call this a U-belt. By removing the gates the choice of bed roughness and particle size becomes flexible and the slip with the bed can be reduced. Theoretically, if no RIMS was required and the gap between the side-walls and the belt is tight enough, particles as small as 1 mm could be used. Another advantage of the U-belt is that the velocity field near the upstream wall is more continuous because the material is sheared upwards when reaching the end of the channel instead of impacting the wall at high velocity. Such high impact velocity causes an unwanted increase in pressure near the upstream wall, which might

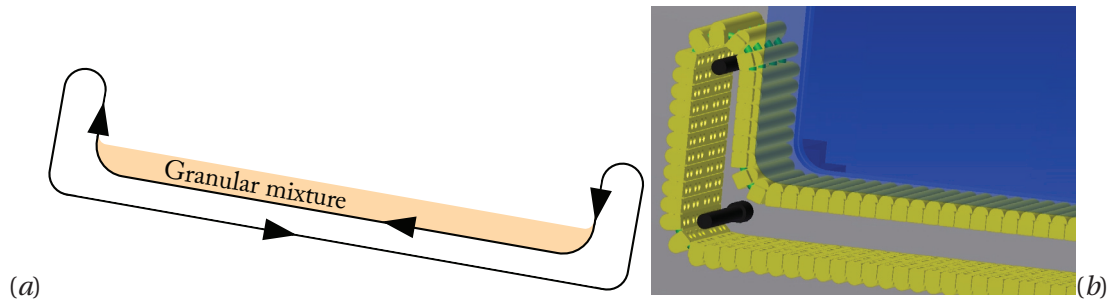


Figure 3.10: (a) The gates at the upslope and downslope ends of the channel can be removed by letting the belt curve upwards, a so-called U-belt. (b) Schematic of a U-belt consisting of individual bars.

lead to jamming or other problems.

One downside of the U-belt design is that it increases the complexity of the construction significantly. The concave curvature of the belt is difficult to implement. The convex curvature of the belt is caused by wrapping it around an axis, but the concave curvature can only be attained by pushing the belt down. In Channel B the belt follows a groove in the side-walls, which forces the concave curvature. A problem with this solution is that a very high friction occurs where the belt moves through the concave part of the groove, which can cause the belt to jam. Unfortunately, we have so far not found a solution for this problem.

Challenge 5. Few options exist for a flexible belt that resists both benzyl-alcohol and ethanol and finding a manufacturer who will make a belt from one of these materials is even more challenging. For Channel A a metal belt is used. To add roughness to the belt rectangular metal bars 1-mm-high and 2-mm-thick are soldered transversally on the belt at 6 mm intervals. Unfortunately these strips break off easily as a result of particle jamming under the gate. For this reason and the relatively low flexibility of the metal belt a different design is used for the U-belt in Channel B. The belt is constructed out of individual rectangular pieces made of polyoxy-methylene (POM). Figure 3.10(b) shows a schematic of a U-belt made of such

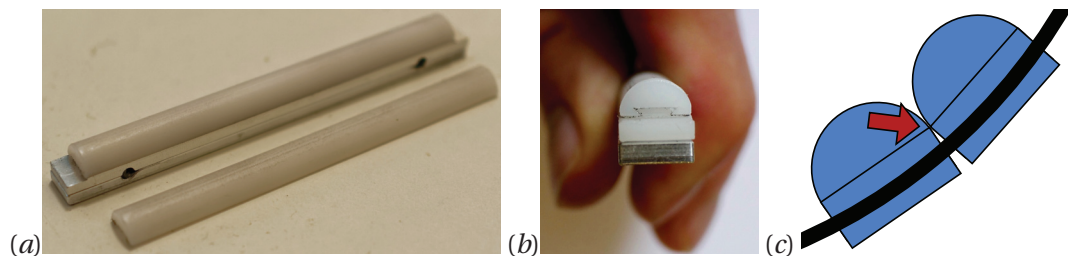


Figure 3.11: (a) Photograph of a belt piece consisting of a metal construction with a plastic piece on top. The plastic piece can be slid off. (b) Side-view of a belt piece. (c) A schematic side-view of belt pieces. When they pass the concave corner the bars are pushed into each other. The distance between bars and their height must be carefully tuned to prevent jamming.



Figure 3.12: View inside Channel B, looking at the upstream wall. Don't be misled by the reflection of the belt in the right wall.

pieces. The discrete belt pieces are reinforced with metal at the bottom and allow for an easily changeable roughness by sliding on different top parts, as shown in Figure 3.11 (*a–b*). The second advantage is that, because the belt pieces are sturdy, they easily follow the grooves in the wall that lead them through the convex and concave corners. Figure 3.12 shows a photograph taken of the inside of Channel B looking in the direction of the upstream wall.

When the belt pieces travel through the convex corners they slightly separate. The separation in the convex corner is not a problem because particles do not come near the convex corners. Nonetheless, serious problems can arise if particles get carried up to the convex corner at the upslope end of the channel. If particles are small enough they can get stuck in between the pieces, which will cause the belt to jam. This problem has occurred in our tests, when the system was partially wetted and small particles stuck to the belt due to liquid surface tension and were carried up the vertical section of the belt. When the belt pieces travel through the concave corners they are squeezed together by large forces, as depicted in Figure 3.11 (*c*). Depending on the available space between bars and their height, jamming can occur and as such their shape has to be designed carefully.

Aside from the POM belt pieces all material in Channel B is either metal or glass. The sealant that is used is Loctite SI 5910 which is fully resistant to the RIMS liquid.

Challenge 6. The metal belt in Channel A is driven by two metal axes. The axes are wrapped in Viton rubber and there is no slip because a tension is applied to the belt preventing any

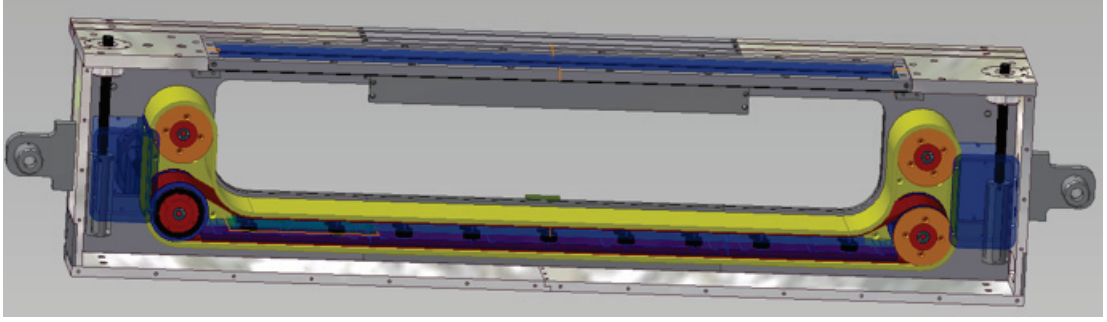


Figure 3.13: Schematic of the interior of Channel B, with the front panel removed. The yellow belt is drawn here as a continuous belt, whilst in fact it is made of discrete pieces. The red belt that is wrapped around the bottom two axis is a solution to drive the yellow belt. Friction is applied along the entire length of the channel instead of only at the axes.

liquid from getting between the belt and the axes. In the Channel B with the U-belt made of discrete pieces, the belt is driven by four axes wrapped in Viton. The belt pieces are pressed against the axes by being placed in the grooves in the side-wall and all pieces are strung on two kevlar ropes. Unfortunately, this has turned out to be a bad solution, because the forces pushing the pieces on the axes are too big and jamming occurs. The tension has been lowered by reducing the thickness of the pieces, but this results in slip. A new solution currently under investigation is to allow quite considerable space between the axes and the belt and drive it via a separate Viton belt wrapped around the lower two axes, as shown in the schematic in Figure 3.13. This second belt transmits force along the entire length of the channel instead of only at the axes.

Although the discrete belt pieces have a number of advantages they currently erode the Viton through mechanical friction. A solution under investigation is to add protective strips along the Viton belt.

3.3 Numerical Simulations

The work described in this thesis also involves discrete particle method (DPM) simulations. These are performed through MercuryDPM code [MercuryDPM.org; Thornton et al., 2013a,b]. In all cases dry bi-disperse mixtures of spherical particles are used, with all of the particles of the same non-dimensional density $\rho_p = 6/\pi$, but of two different non-dimensional diameters d_s and d_l for small and large particles, respectively. All of the simulation parameters are non-dimensionalised so that the gravitational acceleration $g = 1$.

A frictional spring-dashpot model [Cundall and Strack, 1979; Luding, 2008; Weinhart et al., 2012a] with linear elastic and linear dissipative contributions is used for both the normal and tangential forces. This model accounts for sliding, rolling, and torsional interactions between particles. The tangential force models the effects of particle surface roughness, and its spring

stiffness was taken to be $2/7$ of the spring stiffness for the normal direction. For Hertzian contacts, this ratio depends on the Poisson ratio of the material, and is about $2/3$ for most materials [Silbert et al., 2001]. However, Silbert et al. [2001] showed that the contact dynamics are not very sensitive to the precise value of this ratio, and $2/7$ is more practical because the frequency of normal and tangential contact oscillation and the normal and tangential dissipation are equal [Weinhart et al., 2012b]. The particles have the same coefficient of restitution $r_c = 0.1$, which was chosen to be less than typical known values for glass (~ 0.9) in order to model the dissipative effects of the interstitial fluid. The inter-particle friction is $\mu_p = 0.5$.

This linear spring dashpot model allows to view the particle contact as a damped harmonic oscillator, for which the half-period of a vibration around an equilibrium position is the typical response time on the contact level, also called the collision time. Here, the collision time is fixed at $t_c = 0.005$, with the collision properties (dissipation and stiffness) chosen to be different for small/small, small/large and large/large collisions so that both the contact time and the coefficient of restitution are the same even in the case of a mixed collision. The simulation time step, chosen to be much smaller than the collision time, is $\Delta t = 10^{-4} \sqrt{d_s/g}$. Full details of the precise DPM implementation and contact model can be found in [Weinhart et al., 2012a; Thornton et al., 2012].

All simulations make use of a rough base made of particles, which is created in several steps: Firstly, particles of diameter $d_{base} = 1.7$ are stuck randomly to a horizontal plate. Next, more particles are slowly dropped onto this plate and allowed to settle. Once a thick layer of height $12d_{base}$ is produced, a slice of particles is taken whose centers lie between $9.3d_{base}$ and $11d_{base}$. These particles are endowed with infinite mass and form the rough base. More details of this base creation process can be found in [Weinhart et al., 2012a].

When comparing the predictions of continuum models for particle-size segregation with experiments and particle simulations a problem arises with the discrete nature of the experimental and simulation data. In order to map this discrete data (positions, velocities, orientations, interaction forces, etc.) to continuum fields that can be evaluated at every point in space (such as density, momentum, stress, etc.) a micro–macro transition method is required. Various different techniques have been developed to perform such a micro–macro transition (see [Weinhart et al., 2013] and references therein).

The technique used in the studies presented in this thesis is *coarse-graining*, as described in [Weinhart et al., 2013; Artoni and Richard, 2015; Babic, 1997; Glasser and Goldhirsch, 2001; Goldhirsch, 2010; Weinhart et al., 2012b,a]. This technique is chosen because it is implemented and easily accessible in MercuryDPM. The precise implementation is that of Tunuguntla et al. [2015] because it is adapted for bidisperse systems. Compared to other methods coarse-graining has the following advantages in the context of the studies presented here [Goldhirsch, 2010]: (i) the resulting macroscopic fields exactly satisfy the equations of continuum mechanics, even near the base of the flow, (ii) the resulting fields are even valid

for a single particle, since no averaging over an ensemble of particles is required and (iii) the fields are determined at every point in space, not just at the center of averaging cells as in the case of binning. The coarse-graining method does assume that (i) each particle pair has a single point of contact, as such the particles need to be convex in shape; (ii) the contact area can be replaced by a contact point, implying the particles are not too soft; (iii) collisions are not instantaneous (i.e., particles cannot be perfectly rigid).

A critical parameter of the coarse-graining method is the coarse-graining width w , which can not be chosen arbitrarily. For bidisperse mixtures it has been found that a width $w = 1.0/d_m$, where d_m is the mean particle diameter, is appropriate [Tunuguntla et al., 2015], which is what has been used throughout this dissertation.

The simulations described throughout this dissertation have not been calibrated so as match particle properties between simulations and experiments. The reason for this is that a fully quantitative comparison was not the initial aim of this work.

3.3.1 Simulating the moving-bed channel

Simulating a moving-bed channel poses similar challenges as in the experimental system, however these are all more easily solved. The most important challenge, that of the RIMS fluid, is entirely removed, by virtue of the continuous tracking of particles in simulations. The challenge of the gate height and bed roughness is also easily solved: the moving bed travels through a wall that blocks the particles. To prevent a large buildup of stress at the point where the particles get pushed into the wall, a small slope is positioned too guide particles up and decrease their impact velocity. The challenge of the system size and particle size remains due to computational time.

3.4 Summary of Particle Parameters

	Chap.	d_s, d_l	s	ρ_p	t_c	r_c	g	μ_p
Shear-box experiment	4	4, 8 mm	2.0	2230 kg m^{-3}	-	-	9.81 m s^{-2}	-
Chute flow simulation	4	1.0, 2.4	2.4	$6/\pi$	0.005	0.1	1	0.5
Breaking-wave experiment	5	5, 14 mm	2.8	2230 kg m^{-3}	-	-	9.81 m s^{-2}	-
Breaking-wave simulation	5	1.0, 2.4	2.4	$6/\pi$	0.005	0.1	1	0.5

Table 3.1: Various parameters for the different experiments and simulations performed in Chapter 4 and 5. The parameters are: the small and large particle diameter d_s and d_l respectively, the size ratio $s = d_l/d_s$, the particle density ρ_p , the collision time t_c , the coefficient of restitution r_c , the magnitude of the gravitational acceleration g , and the inter-particle friction μ_p .

3.5 Differences between the simulations and experiments

For the DPM simulations I used a moving-bed channel and an inclined chute geometry. I did not use the shear-box geometry because this configuration was not readily available at the time. More importantly, I was not planning on making the simulations a significant part of my dissertation nor to perform a systemic comparison between experiments and simulations. This is also the reason for the different particle-size ratios between the experiments and simulations.

I initially set out to use the moving-bed channel simulations to investigate suitable system parameters to use in the experimental Channel B. The particle-size ratio I chose was the one I intended to use in Channel B. As for the inclined chute simulations, I began to perform these in order to investigate the rising mechanism of large particles. This was a side project that I started because of major delays in the development of Channel B. Here I also chose the size ratio of 2.4.

Eventually, I was forced to make the simulation results a significant part of my dissertation, because of further delays in the construction of Channel B. Unfortunately at the time of writing the rising mechanism of large particles still eluded me, and thus I decided to use the simulation results to support my experimental findings.

4 Size-Segregation Asymmetry

“Reduction! One wants to say more than nature and one makes the impossible mistake of wanting to say it with more means than she, instead of fewer.”

– Paul Klee

UPON closer inspection of a segregating bi-disperse granular flow we can observe that small particles fall down quite efficiently through the holes in the large particle matrix. As a consequence the lowest regions of the flow will quickly be filled up with small particles. The large particles, on the other hand, need more time to reach the top of the flow. We might also observe that some large particles remain in the lower regions of the flow for a long time before catching up with those large particles that have already segregated to the higher regions. This behavior suggests that in Figure 4.1, the segregation dynamics of particle A, which is surrounded by larger neighbours, and particle B, which is surrounded by small neighbours, are different from each other.

The main topic of this chapter is precisely this difference in segregation dynamics of large and small particles and its relation to the local environment. The work discussed is largely based on the letter titled: “*Underlying Asymmetry within Particle Size Segregation*” by K. van der Vaart, P.

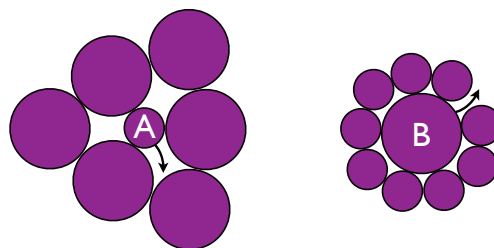


Figure 4.1: Particle A is smaller than its neighbours and will sink. Particle B is larger than its neighbours and will rise. Does particle A sink at the same velocity as B rises?

Gajjar, G. Epely-Chauvin, N. Andreini, J. M. N. T. Gray, and C. Ancey, published on page 238001, volume 114 of Physical Review Letters in 2015. Copyright 2015 by the American Physical Society. The digital object identifier (DOI) for this article is: <http://dx.doi.org/10.1103/PhysRevLett.114.238001>. In addition to this content, the results of discrete particle simulations have been added to this chapter.

4.1 Introduction

Several theoretical models exist for particle-size segregation of bi-disperse mixtures in dense granular flows [e.g. Savage and Lun, 1988; Bridgwater, 1994; Dolgunin and Ukolov, 1995; Gray and Thornton, 2005; May et al., 2010; Fan and Hill, 2011; Marks and Einav, 2011; Tunuguntla et al., 2014; Schlick et al., 2015]. In these models the segregation velocity of particles—whether up or down, depending on their size—is assumed to be partly dependent on the local particle volume fraction. This dependency is given by the so-called *flux function* $F(\phi)$, where ϕ is the local small-particle volume fraction. The large-particle volume fraction is given by $\phi - 1$ because the inter-particle void space is ignored in the continuum treatment.

So far there has been little investigation into the actual functional form of the flux function. As such it is based almost exclusively on theoretical assumptions. The form of $F(\phi)$ is dependent on the choice of the pressure scaling functions that define the partitioning of the stress between the large- and small-particle species as a function of ϕ . Historically the stress partitioning is assumed to be such that large particles carry more of the pressure than small particles, with respect to their local volume fraction [Gray and Thornton, 2005]. Only in the model of Marks and Einav [2011] the flux function is actually based on physical measurements of these pressure scaling functions [Einav, 2007]. The stress partitioning has also been investigated in numerical simulations [Weinhart et al., 2013; Hill and Tan, 2014; Staron and Phillips, 2015a; Tunuguntla et al., 2016]. An altogether different way to gain insight into the functional form of the flux function is to measure the segregation flux or velocities directly. Particle velocities, in contrast to particle stresses, can be more easily obtained from experiments. This is the approach I take in this chapter.

At this point it is useful to discuss the inspiration for the work in this chapter. In the year 1995 Dolgunin and Ukolov [1995] proposed that the flux function was a product of the local large- and small-particle volume fractions, i.e. $F(\phi) = \phi(1 - \phi)$. This form was later adopted by the general continuum framework for size-segregation in bi-disperse mixtures of Gray and Thornton [2005] and remained generally unchanged until 2011 [Marks and Einav, 2011]. A crucial aspect of the flux function postulated by Dolgunin and Ukolov [1995] is that it gives rise—in theory—to identical behaviour for large and small particles, characterised by the following two key features: (i) when more particles of a particular species are present locally, the slower this species segregates; (ii) the increase or decrease of the segregation velocities is linear with ϕ ; (iii) the maximum segregation velocities for the two species are equal and occur at the extrema $\phi = 0$ and $\phi = 1$ for small and large particles respectively. This identical and

opposite behaviour is referred to as *symmetric*—a naming convention that is based on both the physical behavior and on the fact that $F(\phi) = \phi(1 - \phi)$ is symmetric in ϕ .

For small particles the above described dependency on ϕ has already been observed indirectly in percolation studies, where the throughput of small particles is measured in a large particle mixture [Jha et al., 2008; Rahman et al., 2008; Remond, 2010]. Single small particles traverse the mixture at the highest speed. If more small particles travel down together, clogging results in a lower segregation rate. For large particles the dependency predicted by the symmetric flux function has not been experimentally investigated. However, Golick and Daniels [2009] reported an observation that in their annular shear cell experiments large particles were segregating very slowly in regions of many small particles. Much slower than small particles sank in regions of many large particles. They did not further investigate, but their observation indicated a more complex dependence of segregation velocity on the local concentration.

As we will see in this chapter, the flux function is indeed not symmetric and the behavior of large and small particles is entirely distinct. I demonstrate that utilizing this fundamental insight by means of an asymmetric flux function in the theory has a significant impact on the accuracy of theoretical predictions.

The following section will explain in more detail the difference between a symmetric and asymmetric flux function. Section 4.3 will outline the experimental and numerical simulation setup and protocol. Sections 4.4 and 4.5 will discuss experimental and simulation results respectively.

4.2 Theory and Modeling of Size-Segregation Asymmetry

Continuum models for segregation in sheared dense bi-disperse flows all share a similar advection-diffusion structure

$$\frac{\partial \phi}{\partial t} + \nabla \cdot (\phi \mathbf{u}) - \frac{\partial}{\partial z} (q F(\phi)) = \frac{\partial}{\partial z} \left(D \frac{\partial \phi}{\partial z} \right), \quad (4.1)$$

where the z coordinate is the upward pointing normal to the bed, the x coordinate points in the flow direction, the y coordinate points horizontally perpendicular to the flow direction and $\nabla := [\partial/\partial x, \partial/\partial y, \partial/\partial z]^T$. The bulk velocity field $\mathbf{u} = (u, v, w)$ has components in the above directions. The small particle concentration is $\phi(x, y, z, t)$, and q and D are the mean segregation and diffusion rates respectively. The first term on the left-hand side in equation (4.1) describes the temporal evolution, whilst the second term describes the advection with the bulk flow. The segregation in the z direction is captured by the third term, which contains the flux function $F(\phi)$. The right-hand side of the equation models the diffusion along the direction of segregation.

The flux function determines the dependence of the segregation flux on ϕ . It has the property that segregation ceases when the concentration reaches zero (pure large phase) or unity (pure

small phase). The simplest mathematical form of a flux function is quadratic

$$F(\phi) = \phi(1 - \phi) \quad (4.2)$$

More complex forms have been proposed, but to illustrate the modeling of size-segregation asymmetry, we will focus on this simple form. The quadratic flux function is symmetric about $\phi = 0.5$, as shown in Figure 4.2(a). The segregation velocities w_v ($v = l, s$) of large and small particles associated with the segregation equation (4.1) are

$$w_l(\phi) = w + q \frac{F(\phi)}{1 - \phi}, \quad w_s(\phi) = w - q \frac{F(\phi)}{\phi}, \quad (4.3a, b)$$

where w is the bulk flow velocity. Both velocities are uniquely determined by the flux function $F(\phi)$ (see Appendix A for the derivation). The quadratic flux function (4.2) gives the following segregation velocities as a function of ϕ for the large and small particles

$$w_l(\phi) = w + q\phi, \quad w_s(\phi) = w - q(1 - \phi). \quad (4.4a, b)$$

These velocities are plotted in Figure 4.2(b). We observe that the symmetry of the quadratic flux function dictates that small- and large-particle segregation velocities have an identical but opposite dependence on ϕ . The small-particle velocity increases from $w_s = 0$ at $\phi = 1$ to its maximum at $\phi = 0$, whilst the large-particle velocity exhibits exactly the opposite behavior, and with the same maximum velocity as for the small particles. Their velocity dependence on ϕ is symmetric.

In order to model a non-symmetric velocity dependence a flux function can be used that is asymmetric around $\phi = 0.5$ [Gajjar and Gray, 2014]. The simplest asymmetric flux function is

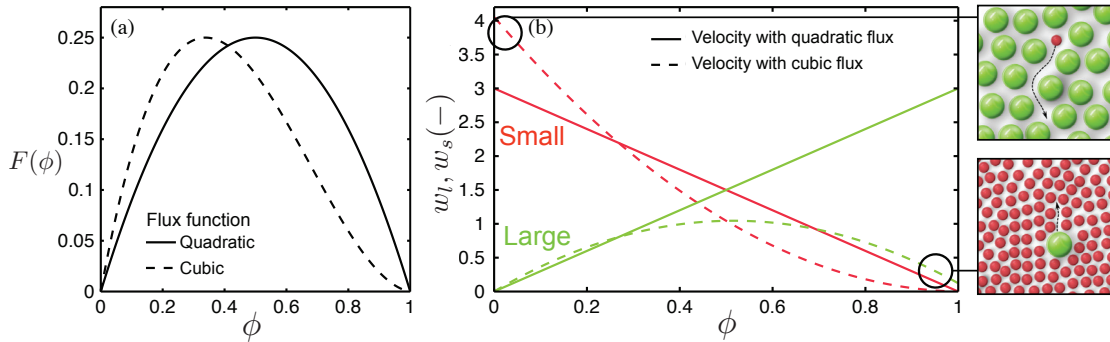


Figure 4.2: Flux functions and segregation velocities. (a) Cubic (dashed line) with $\kappa = 0.97$ and quadratic (solid line) flux function. The cubic flux function is skewed to the left and asymmetric around $\phi = 0.5$. (b) Segregation velocity w_v ($v = l, s$) of large (green) and small (red) particles as a function of volume fraction ϕ for the quadratic (solid line) and cubic (dashed line), with $\kappa = 0.97$, flux functions. For the quadratic flux function the small and large particle velocities are identical but opposite, whereas for the cubic flux function the maximum of the small particle velocity is much higher than for the large and the maximum of large particles is shifted to intermediate ϕ .

the cubic form

$$F(\phi) = A_\kappa \phi(1 - \phi)(1 - \kappa\phi), \quad (4.5)$$

where $0 \leq \kappa < 1$ is the asymmetry parameter and A_κ is a normalisation constant that gives the same area under the curve as the quadratic flux function. In the limit $\kappa \rightarrow 0$ the symmetric quadratic flux (4.2) is recovered. As shown in Figure 4.2(b), the cubic flux function (4.5) produces an asymmetry in w_v between small and large particles: the maximum velocities are different. A small particle will percolate down more quickly at $\phi = 0$ than a large particle rises at any $\phi = 1$. Interestingly, the cubic flux function shifts the maximum in the large particle velocity w_l to an intermediate value of ϕ , suggesting that large particles rise faster when they are in mixed region.

4.3 Setup and Protocol

I have performed experiments and numerical simulations. The experimental geometry is an oscillating shear-box and the simulation geometry is a chute flow. In the shear-box a linear oscillating shear is applied with a fixed amplitude and period. In the chute the flow is driven by gravity. The aim is to study the dynamics of particles during segregation in bi-disperse mixtures with roughly equal volumes V_s^p and V_l^p of small and large particles respectively. In order to prepare such mixtures the volume of large particles is placed at the bottom of the geometry, with the small particles on top. This is referred to as a normally graded mixture. Whilst the global volume fraction of small particles $\Phi(\%) = V_s^p / (V_l^p + V_s^p)$ was varied between different runs the total particle volume $V^p = V_l^p + V_s^p$ was kept constant. Three-dimensional concentration fields are produced by employing coarse-graining [Tunuguntla et al., 2015] (see Section 3.3).

4.3.1 Experiments: Shear-box

Full details of the shear-box geometry and the applied shear can be found in Section 3.2. A schematic is shown in Figure 4.3. The geometry is filled to a height $h = 87 \pm 3$ mm with a bi-disperse mixture of borosilicate glass spheres ($\rho_p = 2.23$ g/cm³) with diameters $d_l = 8$ mm and $d_s = 4$ mm. The large particles are placed at the bottom of the geometry, after which the surface is flattened and the small particles are carefully placed on top. During filling it is impossible to prevent that some small particles already penetrate the large particle matrix, hence the interface between the small particles and the large particles is not sharp. This however, does not give rise to any further problems. As noted above, the global volume fraction of small particles $\Phi(\%)$ is varied between different runs, whilst the total particle volume $V_p \approx 100$ cm³ is kept constant. In practice, V^p is fixed by keeping the weight of the total mixture at $m^p = 226 \pm 1$ g.

The oscillation period for a cycle is chosen $T = 13$ s in order to have a low shear rate. With a

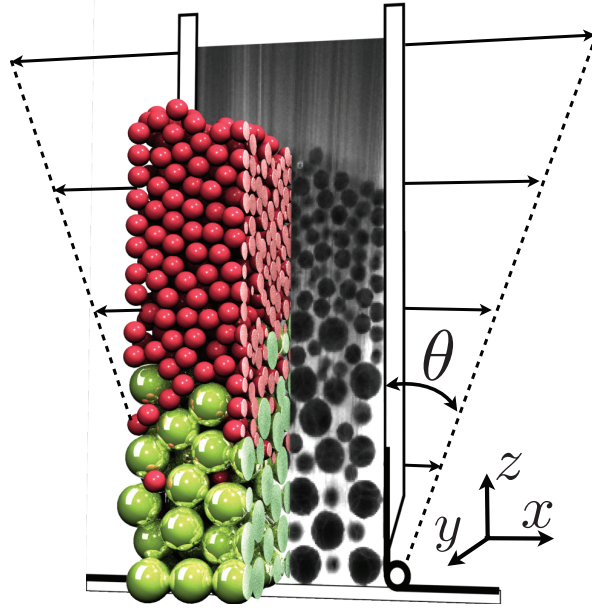


Figure 4.3: Schematic of the experimental setup. Full details can be found in Section 3.2. A raw data image is shown in grayscale and a cross-section of a reconstructed particle mixture in the setup. The colors are added for clarity, since the actual particles are transparent. This particular mixture is composed of particles of diameter 3 and 6 mm, which were used in preliminary testing. Image courtesy of G. Epely Chauvin.

maximum inclination angle $\theta_{max} = \pm 30^\circ$, this gives a maximum shear rate of $\dot{\gamma}_0 = 0.279 \text{ s}^{-1}$ and a maximum grain displacement amplitude $A = \gamma_0 h = 50 \pm 2 \text{ mm}$. In a separate set of experiments the inclination angle θ_{max} is reduced to $\pm 10^\circ$. This decreases the speed of segregation by both lowering the maximum grain displacement and the shear rate. This permits a more accurate tracking of particles with a higher time-resolution. The maximum shear rate for this θ_{max} is $\dot{\gamma}_0 = 0.085 \text{ s}^{-1}$.

The particle positions are obtained in three-dimensional space using refractive index matched scanning (RIMS) [Dijksman et al., 2012; Wiederseiner et al., 2011a]. The RIMS method and implementation are explained in detail in Sections 3.1.2 and 3.2.2. A scan is performed after each full cycle with the shear-box in the upright position at $\theta = 0$, hence I define a non-dimensional time $\hat{t} = t/T$ corresponding to the number of elapsed cycles.

Side-wall effects exist, with small particles preferentially located near the stationary vertical walls, but this does not affect the overall segregation. This phenomenon underlines the importance of using RIMS to obtain all particle positions, instead of only imaging the layer that is visible through the side-wall. The horizontal particle motion is diffusive, hence the concentration can be spatially averaged in x - y plane. I observe convection rolls [Royer and Chaikin, 2015] at high angles $|\theta_{max}| > 45^\circ$ that seem to originate from a geometrical squeezing effect: as the inclination angle of the walls increases the distance between them decreases.

This effect is small at low angles, but increases rapidly above $\theta = 40^\circ$. Convection is also influenced by the width between the oscillating walls, with more convection if the walls are far apart or very close together. I optimised the distance between the walls in order to reduce this effect to a minimum.

In the analysis of the particle motion I was careful to not include any particles that spend more than 80% of the time close to the walls. This was particularly important for the small particles, which found it easier to segregate when close to the wall. In addition, because of the difficulty in image analysis particles are often lost between oscillations and hence trajectories are seldom complete for the entire duration of the experiment. I decided it is better to be too strict and have less complete trajectories, instead of having the risk that a trajectory is continued by another particle. Fortunately, this was not a problem when studying single large or single small particles in mixtures of purely large or small particles, respectively, because the identity of the single intruder can not be mistaken.

4.3.2 Numerical Simulations: Chute Flow

The simulation details can be found in Section 3.3. A dry bi-disperse mixture of spherical particles is used, with all of the particles of the same non-dimensional density $\rho_p = 6/\pi$, but of two different non-dimensional diameters, $d_s = 1$ and $d_l = 2.4$, for small and large particles

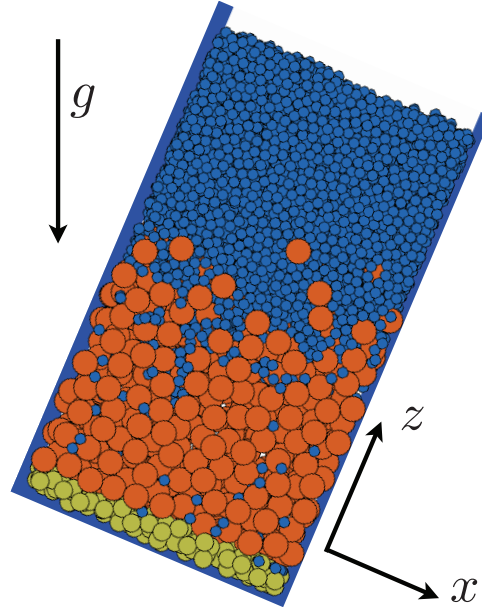


Figure 4.4: Chute flow simulation of a bi-disperse mixture, shortly after startup, for $\Phi = 0.5$. The inclination is $\theta = 23^\circ$. The diameters of the large (orange), small (blue) and bed (yellow) particles are $d_l = 2.4$, $d_s = 1.0$ and $d_{base} = 1.7$, respectively. Gravity direction g and coordinates (x, z) are indicated, with the direction- y perpendicular to the xz -plane. The domain is periodic in the x - and y -directions.

respectively. All of the simulation parameters are non-dimensionalised so that $g = 1$. A larger size ratio between the particles is chosen compared to the shear-box experiments because segregation in the chute-flow is slower; having a larger size ratio compensates for this.

The three-dimensional simulation, see Figure 4.4, is periodic in the x and y directions and has dimensions $(x, y) \in [0, 25] \times [0, 9.8]$. The chute is inclined at $\theta = 23^\circ$ and the bed consists of a disordered, irregular boundary created from fixed particles with size $d_{base} = 1.7$ (see Section 3.3 for details on the creation of the base).

At the start of the simulation the large particles are positioned at the bottom of the chute and the small particles on top. The total volume was held constant between runs by fixing the flow height $h = 45 \approx 18d_l$. After deposition of all the particles, the inclination is set to $\theta = 26^\circ$ to facilitate a fast fluidization of the entire mixture. This angle is held for a short period after which it is decreased to $\theta = 23^\circ$. The angle $\theta = 23^\circ$ is chosen because it gives rise to a low flow velocity resulting in a dense flow, whilst still having a practical segregation speed.

4.4 Experimental Results: Shear-box

4.4.1 Phenomenology

The shear that is applied to the mixture by the oscillating walls of the shear-box gives rise to segregation and small particles sink to the bottom of the flow whilst large particles rise. Figure 4.5 shows how the mixture typically evolves in time: The initial normally graded state—with large particles on the bottom—becomes homogeneously mixed, after which the mixture develops a state where roughly 99% of the large particles are on top. Interestingly, some large particles remain in the lower regions of the flow close to the bottom of the geometry, when all the other large particles have reached the top. I determined that these particles are not stuck but rise at a slower rate than the ones that have reached the top before them. A similar observation was made by Golick and Daniels [2009] who reported that a small particle falling through a mixture of mostly large particles does not progress at the same rate as a large particle rising through a mixture of both large and small particles.

This behavior, the lagging of large particles in regions of many small particles, should have an effect on the global segregation time. That is, full segregation of the system is likely to be delayed by these lagging large particles. Therefore, I define a segregation time \hat{t}_{seg} as the time needed for the vertical centers of mass $z_m = \frac{1}{n_p} \sum_{i=1}^{n_p} z_i$ of the two species to reach a steady state, i.e., a constant vertical position in time. I record \hat{t}_{seg} for mixtures with varying global volume fraction of small particles $\Phi(\%)$, whilst keeping the total mixture volume constant. The centers of mass for large and small particles for three different values of Φ are plotted in Figure 4.6(a). Figure 4.6(b) shows that \hat{t}_{seg} scales linearly with Φ , demonstrating that with more small particles in the mixture the segregation is slower and the segregation time is longer, a trend that has also been observed in 2D chute flow simulations [Staron and Phillips, 2014].

A linear increase of segregation time at low Φ has also been reported in studies of percolation [Jha et al., 2008; Rahman et al., 2008; Remond, 2010], where a few small particles that sink in a sheared mixture of large particles have to compete over void spaces, slowing down the segregation as a consequence. Staron and Phillips [2014] proposed the following explanation for the linear dependence of \hat{t}_{seg} on Φ : At low Φ , small particles move slower when there are more small particles, because there is less available void spaces. At high Φ , it takes a longer time for large particles to travel to the top of the flow when the layer of small particles above them is thicker [Golick and Daniels, 2009; Staron and Phillips, 2014]. In this explanation the behaviour of species that has the dominant presence, is ignored. Which raises the question as to how do these explanations combine at an intermediate Φ ? A clue is given by the work of Golick and Daniels [2009] which reported that for a $\Phi = 50\%$ mixture the transition from the unsegregated state with small particles on top to a mixed state is faster than the subsequent transition from the mixed state to the final segregated state. This points to two separate processes, one fast and one slow, that are likely to be related to the distinct behaviour of small and large particles and their local environment.

4.4.2 Particle Dynamics

We are thus motivated to study the dynamics of a single small particle (SSP) segregating in a mixture of large particles and a single large particle (SLP) segregating in a mixture of small particles, which I refer to as $\Phi = 0^+\%$ and $\Phi = 100^-\%$ mixtures respectively. Following this investigation we will see how these dynamics combine at intermediate Φ . Note that, at this

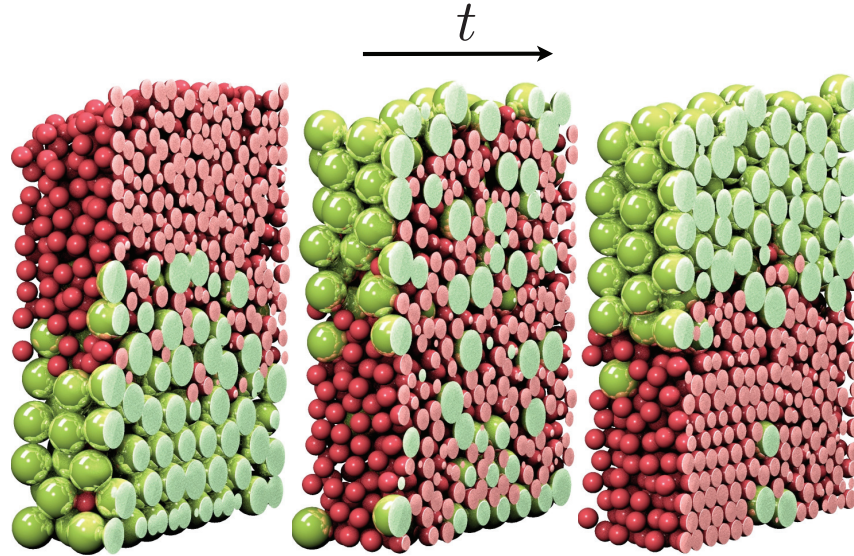


Figure 4.5: Cross-sections at different times during an experiment. Particle positions are reconstructed from the experimental data. This particular mixture is composed of particles of diameter 3 and 6 mm, and is one of the preliminary tests. Image courtesy of G. Epely Chauvin.

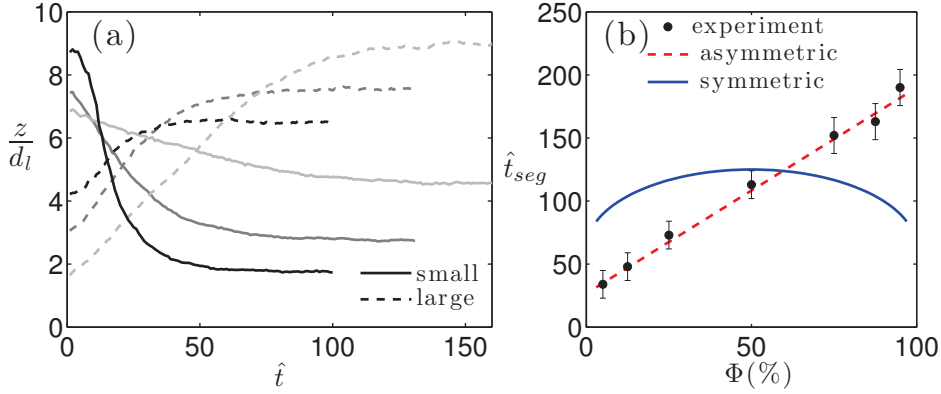


Figure 4.6: (a) Time evolution of the vertical center of mass position z_m for large and small particles in $\Phi = 25\%$ (black), 50% (dark gray) and 75% (light gray) mixtures. $\theta_{max} = \pm 30^\circ$. (b) Segregation time \hat{t}_{seg} as a function of Φ ; solid line is a fit for the symmetric model with $S_r = 0.016$, whilst the dashed line is a fit for asymmetric model with $S_r = 0.030$ and $\kappa = 0.89$.

point I set $\theta = \pm 10^\circ$ in order to slow down the segregation and increase the time resolution.

The first observation is that the trajectories of these two single intruders, shown in Figure 4.7(a), are quite different: (i) the SLP segregates roughly three times slower than the SSP; and (ii) the SLP rises smoothly at an almost constant speed, whereas the SSP shows a stepwise motion with steps of the order of d_l . This suggests that the small particle falls through gaps in the large particle matrix under gravity, typically traversing a single layer, but sometimes even two layers at once.

In order to more precisely understand the nature of these trajectories, we study the root mean square of the vertical displacement (RMSD) after $\hat{\tau}$ cycles: $\sigma(\hat{\tau}) = \sqrt{\langle \Delta z^2(\hat{\tau}) \rangle}$, where $\Delta z(\hat{\tau}) = z(\hat{\tau} + \hat{\tau}) - z(\hat{\tau})$ and the $\langle \dots \rangle$ indicates a time average. The RMSD plotted in Figure 4.7(b) shows that the dynamics of the SLP and SSP are diffusive (logarithmic slope 0.5) at short timescales and super-diffusive or linear with time (logarithmic slope 1)¹ at longer timescales. The super-diffusive dynamics naturally correspond to the segregation, i.e., a linear increase with time. The crossover length scale between the diffusive and segregation regimes for the SSP is approximately d_l , which judging from the trajectory data, corresponds to the typical segregation step-size of the SSP. The crossover length scale for the SLP is lower, roughly $0.2d_l$ ($= 0.4d_s$), which is likely related to the scale of the rearrangements of the surrounding small-particle matrix. The final observation is that the timescale at which segregation kicks in is longer for the SSP ($\hat{\tau} \approx 50$) compared to the SLP ($\hat{\tau} \approx 20$).

To investigate the relation between the dynamics of the single intruders and their surroundings, we measure the vertical RMSD per cycle $\varsigma = \sqrt{\langle \Delta z^2(\hat{\tau} = 1) \rangle}$ as a function of \hat{t} for the two single

¹For a mean square displacement a linear and quadratic scaling with time indicate diffusive and super-diffusive behavior, respectively.

intruders and the surrounding particle matrix. For the ζ of the surrounding matrix I average the RMSD at each time step over a number of particles at random that are in a region close to the single intruder, at a maximum distance of $3d_l$. As such, the $\langle \dots \rangle$ indicate a time and ensemble average. I define ζ_{SLP} and ζ_{SSP} to distinguish between of the SLP and SSP, respectively. For the large and small background particles I use ζ_l and ζ_s respectively. A lot of information can be deduced from the plots of ζ in Figures 4.8(a) and 4.8(c) and I start with pointing out the differences between ζ_{SLP} and ζ_{SSP} , next we will look at how these parameters differ from their respective background matrix ζ_l and ζ_s .

First of all, ζ_{SSP} is much bigger compared to ζ_{SLP} , which was already evident from the plots of the trajectory in Figure 4.7(a). The SLP also exhibits very tiny displacements, which, judging again from the trajectory data can be attributed to the fact that the SLP spends periods of time trapped between large-particle layers. When comparing ζ_{SLP} with ζ_s , we see that the former is nearly always smaller or equal to the latter. This important feature suggests that the displacements of the SLP are ‘regulated’ by the surrounding matrix. The displacements of the SLP are unlikely to be bigger than the overage scale of rearrangements of the surrounding matrix. Note that ζ_s itself is quite uniform in time, with less variations, compared to ζ_{SLP} , which is

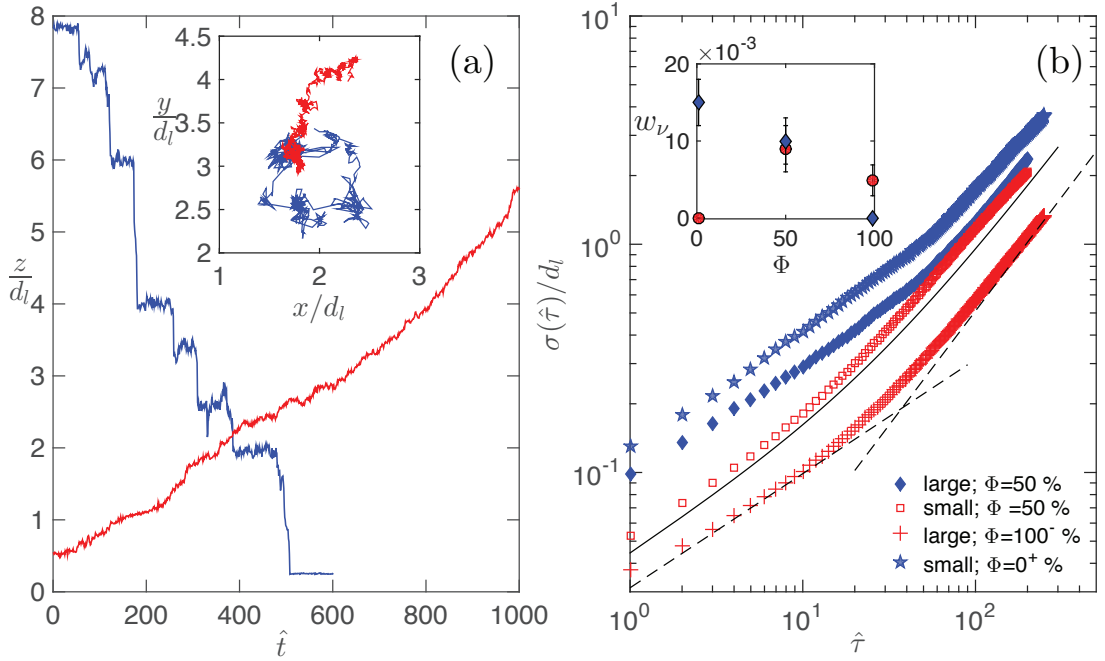


Figure 4.7: Individual particle dynamics for small particles (blue) and large particles (red) with $\theta_{max} = \pm 10^\circ$. (a) Vertical trajectories of a small particle segregating in a $\Phi = 0^+$ % mix; and a large particle segregating in a $\Phi = 100^-$ % mix. Inset: Particle movement in the horizontal plane. (b) RMSD $\sigma(\tau)$ for different mixtures (see legend), with the solid line a fit of $\sigma_s = \sqrt{D_0 \tau + w_s^2 \tau^2}$ at $\Phi = 50\%$ (shifted for clarity). The dotted lines show the slopes 0.5 and 1. Inset: $w_v(\Phi)$ for large (red) ($v = l$) and small particles (blue) ($v = s$).

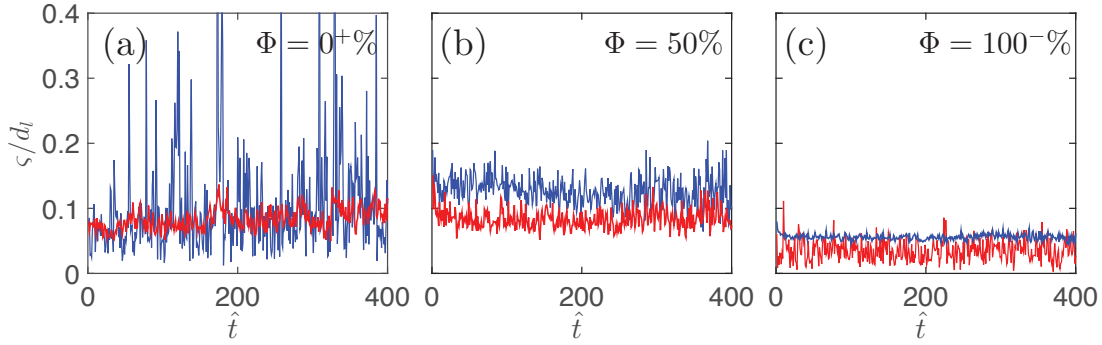


Figure 4.8: Root mean square displacement for single cycles $\zeta = \sqrt{\langle \Delta z^2(\hat{\tau} = 1) \rangle}$ for small particle(s) (blue) and large particle(s) (red), with $\theta_{max} = \pm 10^\circ$, for mixtures of (a) $\Phi = 0^+%$, (b) 50% and (c) 100 $^-%$. The ζ for small particles in (b) and (c) is averaged over multiple particles. The ζ for large particles in (a) and (b) is averaged over multiple particles.

the result of averaging over multiple particles. When comparing ζ_{SSP} with ζ_l (Figure 4.8a) we observe that although ζ_{SSP} has huge variations, as a result of the SSP falling through layers and being trapped in between them, the mean value is of the same order as that of ζ_l .

Comparing With a 50% Mixture

We now investigate how the single particle dynamics change when transitioning to a mixture of $\Phi = 50\%$. Going back to Figure 4.7(b), the RMSD $\sigma(\hat{\tau})$ for the small and large particles in such a mixture can be seen to lie between the $\sigma(\hat{\tau})$ for the SLP and SSP. To be precise: σ for small particles is shifted downward, with respect to the data for the SSP, whilst σ for large particles is shifted upwards, with respect to the data for the SLP. These shifts indicate a faster segregation of large particles and slower segregation of small particles, with respect to the single particle case. We observe that σ in the super-diffusive regime for the large and small particles in the 50% mixture is comparable in magnitude, indicating equal segregation velocities. Note that the magnitude of diffusion of the small particles in the 50% mixture is still greater than that of the large particles. An important feature that we can confidently attribute to the smaller size of the particles.

To better quantify the scaling of the segregation regime of the RMSD curves I fit all the curves with $\sigma_v(\hat{\tau}) = \sqrt{D_0 \hat{\tau} + w_v^2 \hat{\tau}^2}$ with a diffusion coefficient D_0 . In this way we can examine the average segregation velocities w_v for large ($v = l$) and small ($v = s$) particles at different Φ . The inset of Figure 4.7(b) shows that $w_s(\Phi)$ decreases linearly with increasing Φ , whereas $w_l(\Phi)$ increases to a maximum at $\Phi = 50\%$ and then decreases, although not to zero, at $\Phi = 100^-%$.

Before I discuss how this trend relates to the linear scaling of the segregation time with Φ , discussed in the previous section, we try to understand the peak in $w_l(\Phi)$. In order to do so I plot ζ for large and small particles in the $\Phi = 50\%$ mixture in Figure 4.8(b). Comparing this

data to those of $\Phi = 0^+$ and $\Phi = 100^-$ in Figures 4.8(a) and 4.8(c), we see that in the 50% mixture the displacements of large particles are bigger compared to the $\Phi = 0^+$ mixture, whereas for the small particles the big segregation jumps have disappeared. The overall mean scale of rearrangements for both species has increased compared to the $\Phi = 100^-$ mixture.

At this point I am confident to propose an explanation for the linear scaling of segregation time with Φ in Figure 4.6(b): The individual dynamics of small and large particles have a different significance on the overall segregation dynamics at different Φ . At high Φ , the significant dynamics are of the ‘slow’ SLP, which are governed by the scale of rearrangements of the surrounding small particles. At low Φ , it is the ‘fast’ SSP which is significant, making big segregation steps between large particle layers. At an intermediate Φ both processes combine, but are also modified; small particles slow down, i.e., their segregation ‘jumps’ are not as big anymore. This follows from a disappearance of layering because the matrix is made up of both large and small particles. At the same time large particles speed up, because the scale of rearrangements in the flow has increased.

The next step is to actually determine the relation between local volume fraction ϕ and particle dynamics. This is the topic of the next section.

4.4.3 Displacement Dependence on Local Volume Fraction

In order to study the relation between the local environment and the particle dynamics for each species ($v = l, s$) I determine the conditional probabilities $P(\Delta z_v | \phi)$ of the vertical displacement Δz_v per cycle, given that the local small particle volume fraction is ϕ . It is important to point out that because the shear-box applies a linear shear profile the shear-gradient is constant. This in combination with a low shear-rate, allows us to rule out that the segregation is influenced by changes in the temperature or shear-gradient and attribute the probability and magnitude of vertical displacements purely to the local volume fraction. The difference in kinetic stress experienced by the two species as a function ϕ [Fan and Hill, 2011; Hill and Tan, 2014; Staron and Phillips, 2015a; Tunuguntla et al., 2016], which is assumed to give rise to the dependence of the segregation rate on ϕ , is not something I am trying to investigate here. It is purely the effect of the local volume fraction on the segregation rates.

The local ϕ around a particle is determined by averaging ϕ in a spherical shell of width $W_{shell} = d_s$. The effect of this shell width is investigated in Section 4.5. The plots of $P(\Delta z_v | \phi)$ in Figure 4.9(a) and 4.9(b) shows that the most probable vertical displacement of large particles at $\phi = 1.0$ is non-zero and smaller than the most probable displacement of small particles at $\phi = 0$. A clear demonstration of asymmetric behaviour. When overlaying the probability density plots with the mean of $P(\Delta z_v | \phi)$ a clearer trend becomes visible. For small particles there is an almost linear dependence of the mean vertical displacement on ϕ and for large particles the highest mean vertical displacement is at an intermediate ϕ . These trends are similar to those for $w_v(\Phi)$ in the inset of Figure 4.7(b).

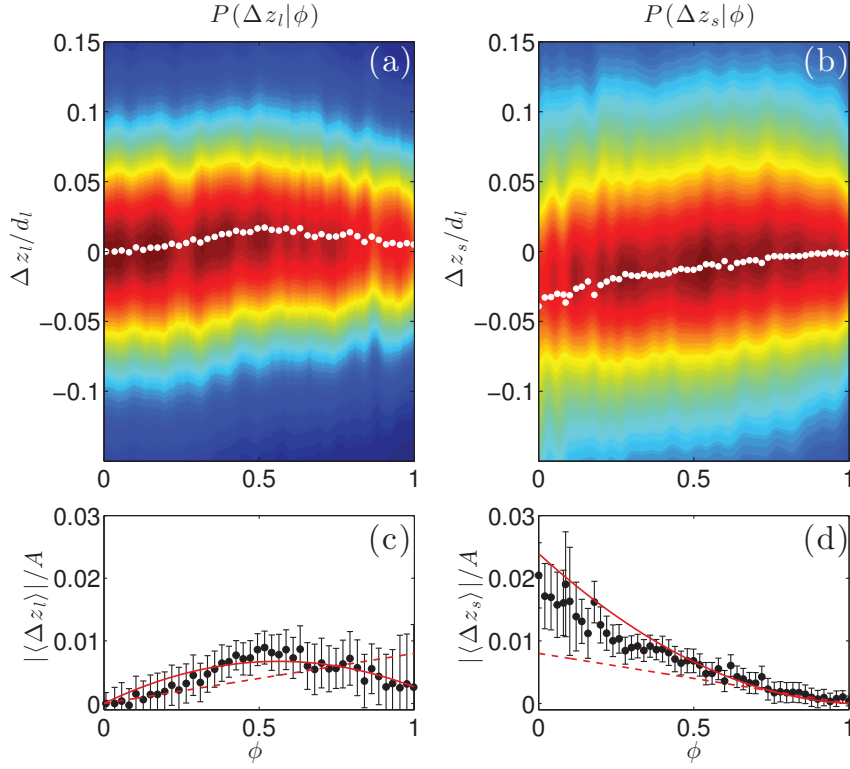


Figure 4.9: (a–b) Conditional probabilities $P(\Delta z_l|\phi)$ and $P(\Delta z_s|\phi)$. White curves are $\langle \Delta z_l \rangle$ and $\langle \Delta z_s \rangle$. (c–d) $|\langle \Delta z_l \rangle|/A$ and $|\langle \Delta z_s \rangle|/A$ as a function of ϕ , with error-bars indicating the standard error of the mean. Dashed and solid lines are plots of equation (4.7) for quadratic and cubic flux functions $F(\phi)$ with $S_r = 0.008$ and $S_r = 0.015$ respectively. The values of S_r were scaled to account for the lower shear rate $\gamma_0\omega$ at $\theta_{max} = \pm 10^\circ$.

4.4.4 Temporal Volume Fraction

At a mesoscale we can observe the effect of the asymmetric segregation velocities in the temporal development of the local small-particle volume fraction $\phi(z, \hat{t})$ for a $\Phi = 50\%$ mixture in Figure 4.10(a). Two important features can be observed in this data. Firstly, the saturation of the bottom of the flow by small particles occurs earlier ($\hat{t} \approx 17$) than the saturation of the top of the flow with large particles ($\hat{t} \approx 20$). This is a very robust feature, easily observed by eye. Secondly, large particles appear to rise predominantly together as indicated by the band of low ϕ (light green). The first feature is easily explained by the asymmetric segregation velocities: small particles beginning the experiment near the interface between the two species, at $z/h = 0.5$, quickly travel to the bottom through the large particle matrix, in accordance with $P(\Delta z_s|\phi)$. The second feature is probably related to the fact that the large particles have a maximum segregation speed at an intermediate concentration. Apparently large particles ‘prefer’ to stick together at this concentration in order to travel faster to the top, reminiscent of some sort of collective behaviour.

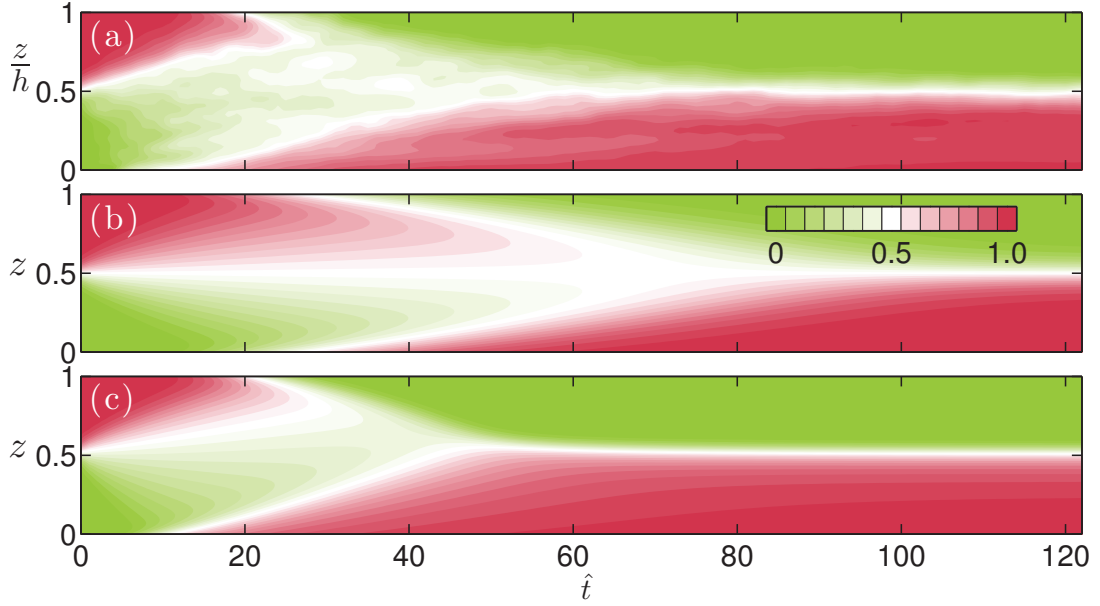


Figure 4.10: (a) Temporal development of $\phi(z, \hat{t})$ versus normalized flow height z/h for a $\Phi = 50\%$ mixture with $\theta_{max} = \pm 30^\circ$. (b)-(c) Theoretical predictions from equation (4.6). (b) Prediction using the symmetric flux function (4.2), with $S_r = 0.016$ and $S_r/D_r = 20.9$. The ratio S_r/D_r is found by least squares matching the steady end state. (c) Prediction using the asymmetric flux function (4.5), with $S_r = 0.030$, $S_r/D_r = 29.6$ and $\kappa = 0.89$.

Theoretical Comparison

The above described effects are a somewhat hypothetical translation of a particle-scale measure, namely the segregation asymmetry, to the meso-scale structure of $\phi(z, \hat{t})$. In order to give a more profound support for the explanation above we will compare a theoretical solution, using the asymmetric cubic flux function, described in section 4.4.4, with the experimental $\phi(z, \hat{t})$ data.

The oscillating shear applied by the shear-box gives an average velocity profile $\bar{\mathbf{u}} = 0$. Additionally, we can assume that ϕ is spatially uniform in the xy -plane. This means that the transport term in Equation (4.1) is zero and Equation (4.1) reduces to:

$$\frac{\partial \phi}{\partial t} - \frac{\partial}{\partial \hat{z}} (S_r F(\phi)) = \frac{\partial}{\partial \hat{z}} (D_r \frac{\partial \phi}{\partial \hat{z}}), \quad (4.6)$$

where $\hat{z} = z/A$, and $S_r = qT/A$, $D_r = DT/A^2$ are non-dimensionalised segregation and diffusive-remixing coefficients respectively. Remember that $A = \gamma_0 h$ is the maximum particle displacement and T the oscillation period. I plot solutions to the theory using both the asymmetric (cubic) flux function (Equation 4.2) and the symmetric (quadratic flux) function (Equation 4.5). The symmetric and asymmetric models were least squares fitted to the data of \hat{t}_{seg} in Figure 4.6(b) to obtain $S_r = 0.016$ for the symmetric model and $\kappa = 0.89$, $S_r = 0.030$

for the asymmetric model. An explanation of this fitting can be found in [Gajjar, 2016]. The two fits of \hat{t}_{seg} plotted in Figure 4.6(b) are remarkably different. The asymmetric flux function results in a linear increase of the segregation time \hat{t}_{seg} with Φ and fits the experimental data well, whereas the symmetric flux results in equal \hat{t}_{seg} at $\Phi = 0\%$ and $\Phi = 100\%$, with a peak at $\Phi = 50\%$.

Because on average the bulk vertical velocity is zero the theoretical segregation velocities in Equation (4.3) can be rewritten as absolute vertical displacements per cycle

$$|\Delta \hat{z}_l| = S_r \frac{F(\phi)}{1-\phi}, \quad |\Delta \hat{z}_s| = S_r \frac{F(\phi)}{\phi}, \quad (4.7)$$

These are shown alongside the experimental data in Figure 4.9(c) and 4.9(d) using the cubic and quadratic flux functions. The experimental trend is clearly better predicted by the asymmetric flux, which is able to reproduce both the peak in $|\langle \Delta z_l \rangle|$ around $\phi = 0.5$ and the nonlinear decrease of $|\langle \Delta z_s \rangle|$. The theoretical prediction is not perfect. The discrepancy of $|\langle \Delta z_s \rangle|$ at low ϕ is possibly the result of particle tracking errors: when small particles move more than their radius they can be lost, hence their displacement is not recorded. This lowers the measured value of $|\langle \Delta z_s \rangle|$. Such a problem does not arise with large particles because their displacements are much smaller.

Integrating Equation (4.6) gives the theoretical $\phi(z, \hat{t})$ in Figures 4.10(b) and 4.10(c). Qualitatively, the asymmetric model reproduces the experimental data on some critical points: (i) the difference in time between the arrival of small particles at the bottom and large particles at the top of the flow; (ii) the collective rising of large particles; and (iii) a lower ϕ in the bottom half of the flow near the end of the experiment, indicating that some large particles are still inside the small particle matrix, segregating very slowly. These features are not found in the symmetric result in Figure 4.10(b). There are however a number of discrepancies between the experimental data and the solution of the asymmetric model. In particular the slope of the two boundaries where $\phi = 0.5$ is not consistent with the experiment. In the theory these boundaries are either too steep or too shallow, indicating the flux function over- or underestimates particle velocities. Possibly a more complex asymmetric flux function could improve this. The cubic flux function used here is but one of many possible flux functions to model asymmetric segregation speeds [Gajjar and Gray, 2014]. By imposing a linear shear I have ruled out any shear rate dependency in the flux function, however it could be possible that a depth or pressure dependency might give rise to the observed bulk scale behavior in the experiment.

4.5 Simulation Results: Chute Flow

A major challenge with the experimental study described in the previous section is the accurate and correct tracking of particles. In addition, experimental constraints limit the system size which raises doubts as to the validity of the statistical analysis. Hence, in this section the

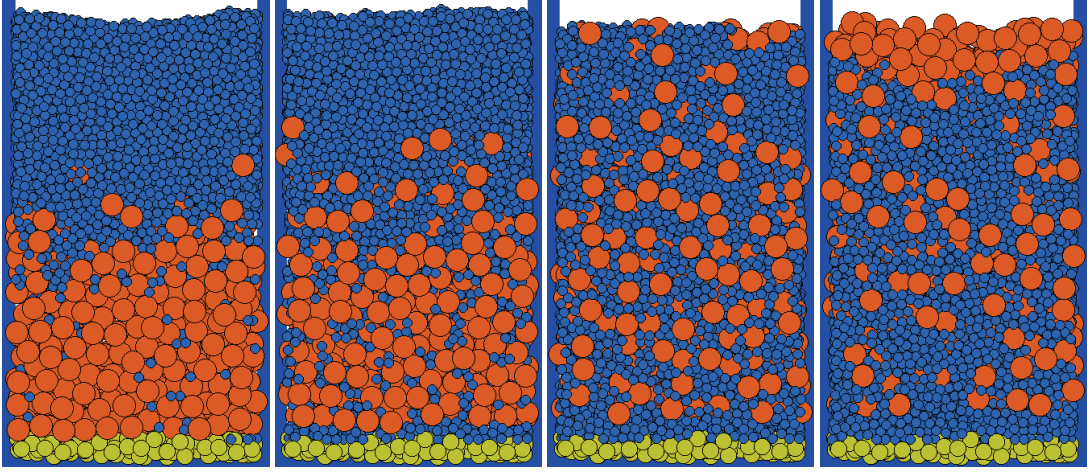


Figure 4.11: Snapshots at different times of a simulation of a bi-disperse segregating mixture in a chute flow configuration. The yellow particles are the fixed rough bed. The global small particle volume fraction $\Phi = 50\%$. The size ratio is 2.4. The time increases from left to right. The slope inclination is $\theta = 23^\circ$.

results of discrete particle simulations are discussed, which inherently allow for perfect particle tracking and much larger system sizes.

4.5.1 Phenomenology

Segregation in the chute flow simulation proceeds in similar manner as in the shear-box experiments: The mixture transitions from a normally graded state, with small particles on top, to a mixed state, and finally to a segregated state with large particles on top, as shown in Figure 4.11. This behavior is widely reported in bi-disperse chute flow simulations [e.g. Rognon et al., 2007; Thornton et al., 2012; Marks et al., 2012; Weinhart et al., 2013; Staron and Phillips, 2014; Tunuguntla et al., 2015].

The effect of size-segregation asymmetry is immediately evident from the thin layer of small particles that quickly appears at the bottom of the flow. It takes a much longer time for top of the flow to be saturated with large particles. Other noteworthy features are a slight decrease in flow depth in the third snapshot in Figure 4.11 as a consequence of the denser packing when the large and small particles are mixed homogeneously [Golick and Daniels, 2009].

Looking at the averaged downstream velocity $\langle u \rangle_p$ as a function of time in Figure 4.12 we see an initial peak in the velocity where the flow accelerates quite fast, followed by a slightly less sharp decrease and a slow increase over time. Possibly the peak is linked to our startup protocol, however I think this is unlikely because the application of the 26° angle is only for a couple of seconds and the peak lasts for several hundred seconds. The height of the initial peak in $\langle u \rangle_p$ seems not to scale with Φ , however the velocity after the peak does scale with Φ : mixtures

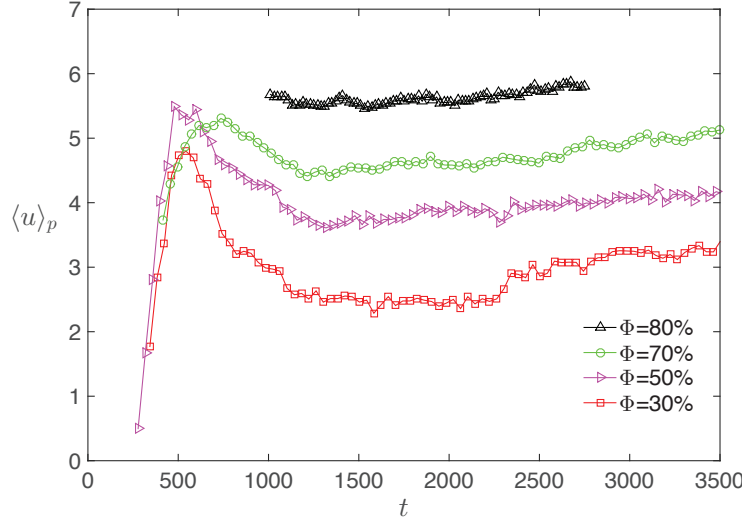


Figure 4.12: Downstream velocity averaged over all particles $\langle u \rangle_p$ as a function of time for different global volume fractions Φ . Note that the sudden jump in $\langle u \rangle_p$ for $\Phi = 30\%$ at $t = 2300$ is the result of layer forming in the large particle mass.

containing more small particles flow faster, except for $\Phi = 0\%$, which has a similar velocity as the flow at $\Phi = 50\%$. Staron and Phillips [2015b] reported for 2D chute flow simulations that large particles increase the bulk friction of bi-disperse flows, which suggests an explanation for our data. The slow increase over time is likely correlated with the segregation, where the mixture would reach its steady state velocity once the flow composition has reached a steady state.

The scaling of the mean velocity with Φ is not a focus of this work and is not further investigated. I did not let the flows fully segregate because I aimed to gather large amounts of data in the segregating regime. Nonetheless, the fact that the flows studied here have a different downstream velocity depending on the mixture ratio is important to keep in mind during the remainder of this chapter. Note that in the shear-box experiment the velocity field is imposed, thereby suppressing any scaling with Φ .

Most of the displacement statistics studied below are obtained in the window after the peak where the flow is slowly accelerating. However, for statistics at low ϕ it is necessary to investigate the regime close to the peak, where at the start of the simulation small particles percolate through the large particle mixture, such as seen in the first snapshot in Figure 4.11.

4.5.2 Trajectories and Mean Square Displacement

We start by looking at the dynamics of single intruders: a single small particle (SSP) segregating in a mixture of large particles ($\Phi = 0^+\%$) and a single large particle (SLP) segregating in a mixture of small particles ($\Phi = 100^-\%$). Typical trajectories of two of such particles, shown in

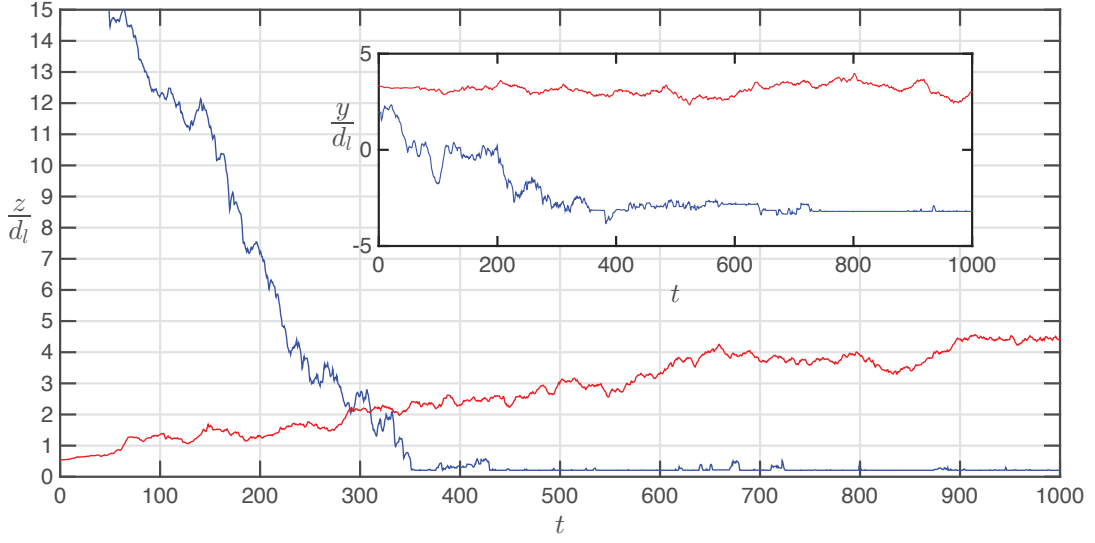


Figure 4.13: Example vertical trajectories of a single small intruder in a $\Phi = 0^+$ % mixture (blue), and a single large intruder in a $\Phi = 100^-$ % mixture (blue). Inset: y -trajectories. The x -trajectory is not shown because it is the downslope direction.

Figure 4.13, are similar to those reported in the previous section for the shear-box experiment: the SLP segregates much slower than the SSP, and the SSP makes segregation steps of the order of d_l .

Looking more closely we do observe some differences: The trajectory of this SLP is less smooth in time compared to the trajectory of the SLP in the shear-box. This is most probably related to the more kinetic flow in the chute, resulting in more diffusion in the vertical direction. The average shear rate in the chute flow is twice as big as in the shear-box (0.15 s^{-1} versus 0.085 s^{-1}).

The SSP on the other hand has a trajectory that is characterized by jumps of size d_l , but the delay time between jumps is shorter and the vertical motion seems more diffusive. This observation could be the result of the fact that the trajectory of the small particle in the chute flow is plotted at a different vertical scale. The chute flow is $19d_l$ deep whereas it is only $10d_l$ in the shear-box experiment. Nonetheless it appears that the time the SSP remains stuck between layers is not as long as in the shear-box. This is a reasonable assumption considering that the chute flow is much more kinetic, as mentioned above.

We will further investigate this behavior when looking at the mean square displacement below, but before doing so, there is another noteworthy feature in the trajectory of the SSP: The small peaks of size $0.5d_l$ occurring just before a big decrease in height, suggesting that the SSP is first sheared over a large particle, thereby slightly moving upwards, and subsequently falls down through one or more layers. When looking back at the trajectory of the SSP in the shear-box in Figure 4.8 it turns out this behavior exists there as well.

Mean Square Displacement. The vertical mean square displacement (MSD) $\langle \Delta z^2(\tau) \rangle$, where $\Delta z = z(t + \tau) - z(t)$, as a function of delay time τ is plotted in Figure 4.14. For the SLP ($\Phi = 100^+ \%$) the MSD has not been ensemble averaged and a number of different MSD curves are shown. I choose to not ensemble average here, and in few other situations below, because ensemble averaging hides some of the underlying differences in the behavior of particles. As I will demonstrate a wide range of segregation and diffusion magnitudes occur in the same system and even between different single large intruders.

We observe a diffusional regime, indicated by a slope of 1, i.e, a linear scaling of the MSD with time, for all SLPs, followed by a super-diffusive regime, signifying segregation, with a maximum slope of 2. Not all SLPs show the same amount of segregation, as indicated by the difference in τ where the slope of 2 sets in. Some SLPs do not appear to exhibit segregation at all on the time-scale shown, i.e., they never scale quadratically with time. This however is misleading, because, when looking at the un-squared mean displacement $\langle \Delta z(\tau) \rangle$ plotted in Figure 4.15(a) we definitely see that all the SLPs rise. The explanation for this contradiction

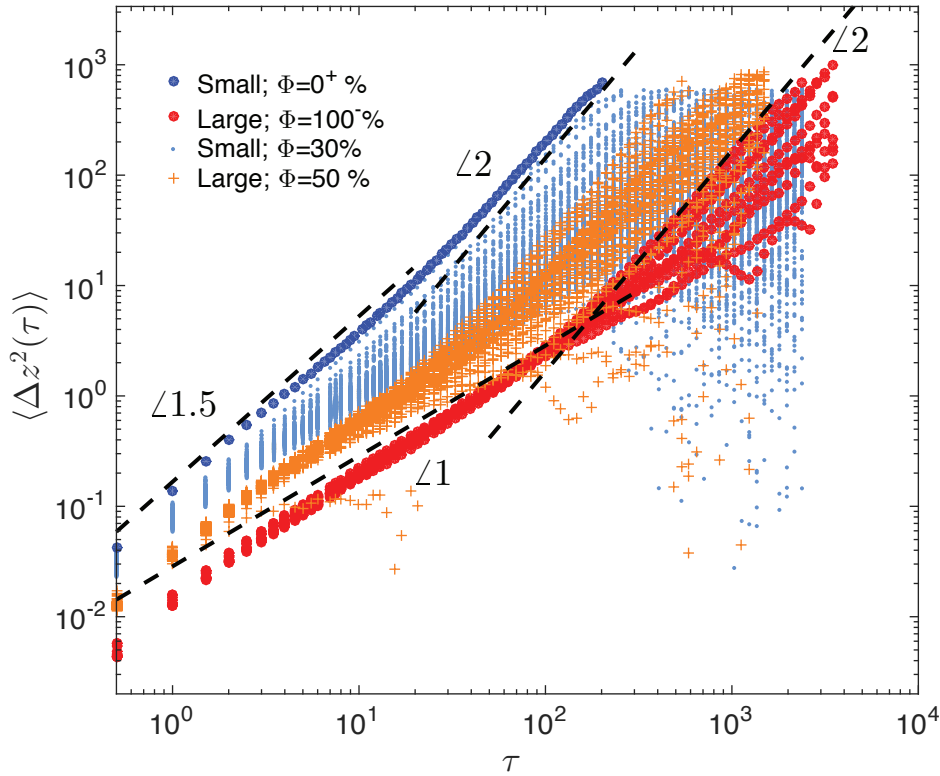


Figure 4.14: Vertical mean square displacement $\langle \Delta z^2(\tau) \rangle$ plotted as a function of delay time τ for single small particles in a $\Phi = 0^+ \%$ mixture (blue circles), single large particles in a $\Phi = 100^- \%$ mixture (red circles), small particles in a $\Phi = 30\%$ mixture (light blue dots), and large particles in a $\Phi = 50\%$ mixture (orange +). For all data $\langle \dots \rangle$ indicates a time-average, except for the single small particles (blue circles), where it indicates both time- and ensemble averaging. The dashed lines indicate different slopes.

is that some large particles segregate so slowly that their behavior is characterized as diffusional, i.e., the increase of the MSD is linear in time, even though the particle moves predominantly in the positive z direction. Of course, it should be considered diffusional if the large particle eventually moves down again. This however, we know not to be true. Thus I conclude that a very wide range of segregation rates is possible for SLPs.

We continue and look at the MSD for SSPs, which I ensemble averaged because the individual MSDs showed nearly identical behavior. SSPs exhibit a slope of 1.5 at short time-scales indicating that they never exhibit pure diffusion; a very interesting feature that was not present in the shear-box experiments. In the shear-box, SSPs exhibited diffusional behavior when in-between large particle layers. Apparently in the chute flow, small particles are always segregating, although sub-linearly with time.

We now investigate the MSD in mixtures of intermediate Φ . First we consider large particles in a mixture of $\Phi = 50\%$. A number of MSDs for large particles picked at random are plotted in Figure 4.14. In general, the MSDs of large particles in the $\Phi = 50\%$ mixture lie above those of SLPs. This indicates a stronger diffusion and stronger segregation. Again slopes of 2 are reached at long time-scales, but a number of large particles appear to exhibit non-segregating behavior at long time scales, as indicated by the very low values of their MSD. The range of different onset times for the segregation regime is also very wide. Some large particles exhibit a segregation of similar magnitude as SLPs. Nonetheless, if we look at $\langle \Delta z(\tau) \rangle$ in Figure 4.15(c) we see that on average most of the large particles in a $\Phi = 50\%$ mixture rise in the studied time window.

Next we consider the MSD for a number of small particles in a mixture of $\Phi = 30\%$, also plotted in Figure 4.14. We observe that the MSDs are shifted downward with respect to the MSDs of

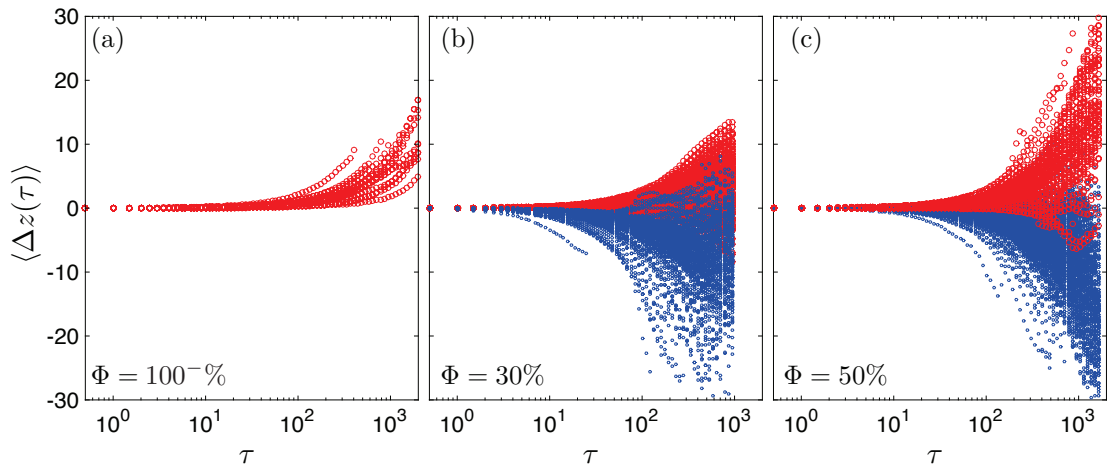


Figure 4.15: Mean vertical displacement $\langle \Delta z(\tau) \rangle$ as a function of delay time τ for large (red) and small (blue) particles chosen at random, for (a) $\Phi = 100^{-}\%$, (b) $\Phi = 30\%$ and (c) $\Phi = 50\%$. The $\langle \dots \rangle$ indicates a time average.

the SSP, signifying a lower magnitude of diffusion and segregation. At short time-scales the slope ranges from 1 to 1.5 and at long time-scales the maximum slope is again 2. We also observe that many small particles do not segregate at all on the plotted time-scale, and come back to their original depth, as indicated by the low values of the MSD at high τ . The range of different behaviors is clearly very wide. The mean displacement in Figure 4.15(b) shows that on average most of the small particles do move downwards, but a number of small particles also move up. Once again I conclude that a very wide range of segregation rates is possible in one flow.

The range of segregation rates in one flow is likely the result of the varying local concentration, pressure, shear gradient, and velocity throughout the flow. On top of that we should not forget the scaling of the mean flow velocity with Φ , observed in Figure 4.12. The MSD data for the SSP and the small particles for $\Phi = 30\%$ has been recorded in slower flows compared to the data for the SLP and the large particles for $\Phi = 50\%$. One of the major difficulties of studying size-segregation is decoupling one parameter, such as the dependence on ϕ , from others, such as the local velocity, pressure and shear gradient. Especially because the flow is evolving. At first small particles are in the higher velocity region at the top of the flow, whilst large particles are at the bottom in the lower velocity region. In order to partially mitigate this problem I record all data for $\langle \Delta z(\phi) \rangle$ in a thin region in the center of the flow from $z = 17$ to $z = 27$. A thinner region would be preferable, but this reduces the amount of data acquired.

4.5.3 Displacement Dependence on Local Volume Fraction

Instead of calculating the conditional probability $P(\Delta z_v | \phi)$, as was done for the shear-box data, here I directly calculate a time and ensemble averaged vertical displacement $\langle \Delta z_v(\phi) \rangle$ ($v = l, s$) as a function of local small-particle volume fraction ϕ . The value of ϕ around each particle is calculated by averaging ϕ in a spherical shell of width W_{shell} . In the analysis of the experimental results $W_{shell} = d_s$, however as we will see below the choice of W_{shell} is not arbitrary. The large amount of statistics obtained in the simulations allow us to investigate the dependency of $\langle \Delta z_v(\phi) \rangle$ on the shell width. Similarly, we have a choice of delay time τ for the calculation of $\Delta z = z(t + \tau) - z(t)$. A higher τ gives a better resolution in terms of displacement magnitude, because particles have moved more, but as they move the ϕ surrounding them changes, and so will their dynamics. Note that I determine ϕ at time t , not at $t + \tau$. I verified there is no observable difference between these two options.

Dependence on W_{shell} . Figure 4.16(a) shows the dependence on ϕ of $\langle \Delta z_s(\phi) \rangle$ for varying W_{shell} . The data is quite scattered but the general trend is a large negative displacement at low ϕ and an almost zero displacement at high ϕ similar to the experimental results. We observe that the data for different W_{shell} overlaps most near $\phi = 0.3$. This is reasonable since the mixture $\Phi = 30\%$. Each data point consists of an average of between 1.000 to 30.000 displacements. The effect of increasing W_{shell} is ‘moving’ such displacement data from high and low ϕ to an intermediate value of ϕ close to the mixture concentration. In the extreme

that W_{shell} spans the entire system we expect all data to collapse on a single ϕ corresponding to the mixture concentration. For low W_{shell} we expect that displacement data is ‘moved’ away from this point.

The data of $\langle \Delta z_s(\phi = 0) \rangle$, plotted in the inset of Figure 4.16(a), shows that $\langle \Delta z_s(0) \rangle$ is reduced with increasing W_{shell} , reaches a minimum around $W_{shell} \approx 2$, and subsequently increasing again. This behavior can be explained as follows: for a small W_{shell} more particles are considered to be in a region of $\phi = 0$ than at large W_{shell} . Thus increasing W_{shell} gives a more realistic value for the displacement, since we are more strict as to what particles we consider to be at $\phi = 0$. Doing so lowers the displacement because particles that truthfully are at $\phi \approx 0$ segregate faster. However, if W_{shell} is increased too much, the requirement for a small particle to be at $\phi = 0$ is too strict, and the error in our data increases because of less data is used for the average. Hence a balance has to be made, taking into account Φ . However, even though we know the mixture Φ , we don’t know precisely how likely it is to observe particles at a certain ϕ . Based on the data I choose $W_{shell} = 2.0$ for the small particles because it gives the lowest value of $\langle \Delta z_s(0) \rangle$ while also having the lowest error.

For large particles we perform the same investigation, but for displacement data at $\phi = 1$ in a mixture of $\Phi = 90\%$. In Figure 4.17 we see that $\langle \Delta z_l(1) \rangle$ remains roughly constant for W_{shell}

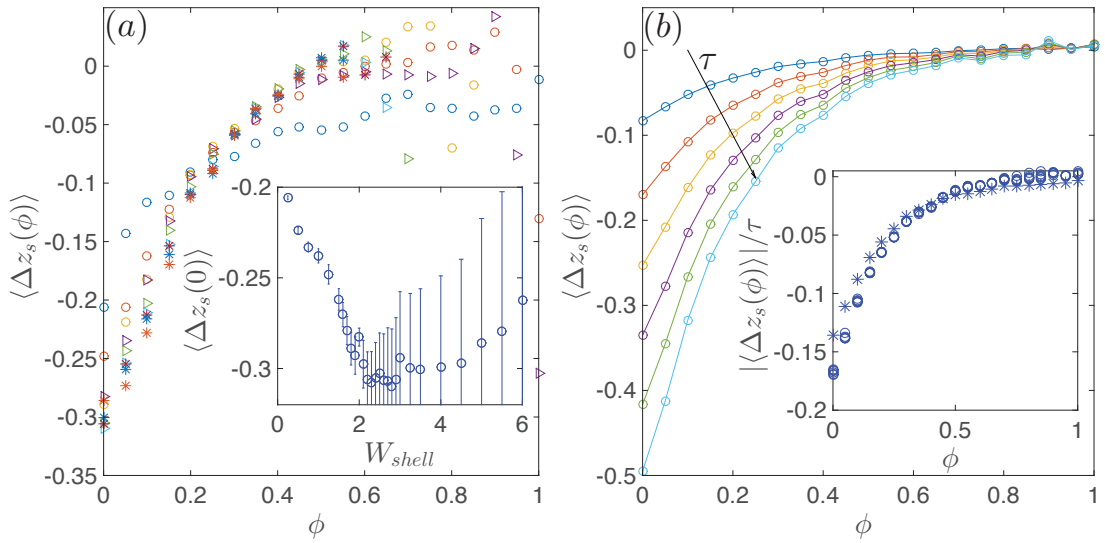


Figure 4.16: In a mixture of $\Phi = 30\%$: (a) Different plots of the average vertical displacement as a function of ϕ for $\tau = 1.5$ and varying W_{shell} . Inset: $\langle \Delta z_s(\phi = 0) \rangle$ plotted as a function of W_{shell} . The magnitude of the errorbars $E(W_{shell})$ is calculated by $E(W_{shell}) = 10^{-3} N_d(0.25) / N_d(W_{shell})$, where N_d is the amount of displacement data. The error is an indication of reduction in the amount of data with respect to the amount for the point at $W_{shell} = 0.25$. The standard deviation is not a good measure of the error because it remains fairly constant. (b) $\langle \Delta z_s(\phi) \rangle$ for different delay times τ . Inset: A plot of $\langle \Delta z_s(\phi) \rangle / \tau$ shows that all data in (b) collapses. The data for $\tau = 50$ with the * marker does not collapse on the other data.

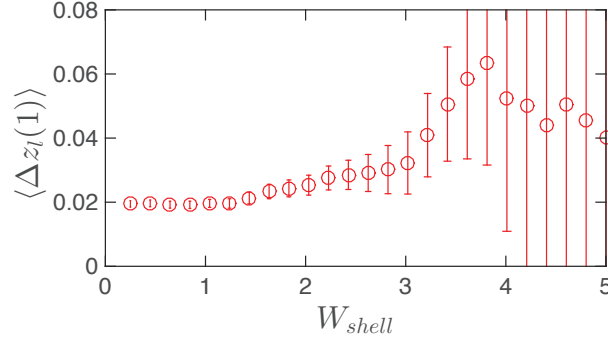


Figure 4.17: The mean vertical displacement of large particles at $\phi = 1$ for different shell widths W_{shell} . Mixture $\Phi = 90\%$ and $\tau = 2.5$. The magnitude of the errorbars $E(W_{shell})$ is calculated by $E(W_{shell}) = 10^{-3} N_d(0.25) / N_d(W_{shell})$, where N_d is the amount of displacement data. The error is an indication of reduction in the amount of data with respect to the amount for the point at $W_{shell} = 0.25$.

between 0 and 2 and the error remains small as well. Above $W_{shell} \approx 2$ the value and error of $\langle \Delta z_l(1) \rangle$ increases. I argue that $W_{shell} = 1$ is too low because it overestimates ϕ because $\phi = 1$ would then correspond to a single layer of small particles around a large particle. Our observations of the slow rising of large particles when surrounded by many particles, suggest that a single layer of small particles around a large particles does not slow it down considerably. Hence I choose $W_{shell} = 2.5$ in order to be strict in assigning high values of ϕ to large particles, whilst having a low error. Additionally, for a large particle to be considered in a $\phi = 0$ region I argue that it should be surrounded by at least one full layer of large particles, hence a W_{shell} equal to a large particle diameter is appropriate.

The arguments above for choosing W_{shell} are to a certain degree qualitative. Fundamentally the shell width is related to the distance on which a particle's displacement is influenced by its local surroundings. In the case of size-segregation, it is the length scale on which a particle effectively 'feels' the presence of particles of other sizes. We could reason that a small particle surrounded by only large particles is not aware of other small particles as long as it does not come into contact with them, however, we do not know how the behavior of the surrounding large particles is affected by the presence of all small particles in the system. For now we have no other choice then to make an educated guess at this interaction distance. For future work I believe more fundamental analysis and arguments are required.

Dependence on τ . Figure 4.16(b) shows $\langle \Delta z_s(\phi) \rangle$ for varying τ . In the calculation of $\langle \Delta z_s \rangle$, ϕ is calculated at a time t while the displacement $\Delta z = z(t + \tau) - z(t)$. Naturally, as τ increases the curves shift towards more negative displacements. The inset shows how dividing the curves by τ —effectively calculating the velocity—collapses them for low values of τ but not for the value of $\tau = 50$. This demonstrates that the segregation dynamics do not change significantly on short time scales, but as the particle moves further away from its position where ϕ is calculated at time t , it will behave differently. This gives a time-scale on which the local environment of

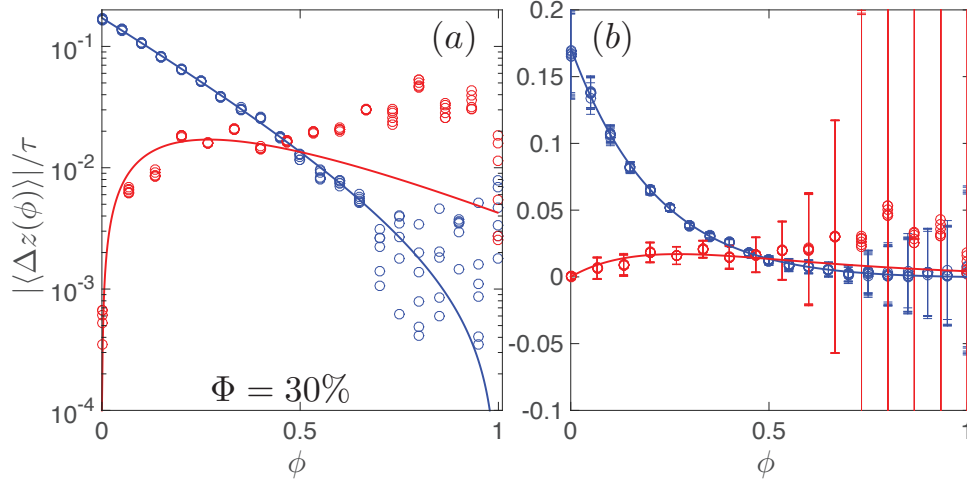


Figure 4.18: (a) Semi-log plot and (b) normal plot of the absolute values of the mean vertical displacement as a function of ϕ for large particles (red) and small particles (blue), normalized by τ . The mixture $\Phi = 30\%$, $W_{shell} = 2$ for small and $W_{shell} = 2.5$ for large particles. Data sets for different τ are shown for both species in order to demonstrate a collapse by dividing by τ . The blue line and red line are the theoretical small particle velocity and large particle velocity, respectively, using an exponential flux function with $S_r = 1.7$ and $G = 3.7$.

the particle changes. This time-scale will of course depend on $\langle \Delta z(\phi) \rangle$. For a large particle at $\phi = 0$ I expect this time-scale to be long, whereas for a small particle at $\phi = 1$ it will be shorter. Based on the data I am confident that delay times shorter than $\tau = 3$ are safe for both species.

Exponential Asymmetry. For the shear-box experiment the segregation velocities as a function of ϕ were captured quite well by a cubic flux function. For the chute flow simulation at $\Phi = 30\%$ an exponential flux function gives a better match as demonstrated in Figure 4.18, where I have plotted $|\langle \Delta z(\phi) \rangle|/\tau$ for large and small particles for varying τ . The exponential flux function is able to produce a bigger asymmetry and is given by

$$F(\phi) = A_G \phi(1 - \phi)e^{-G\phi}, \quad (4.8)$$

where $0 \leq G$ is an asymmetry parameter and A_G is a normalisation constant that gives back the same area as under the quadratic flux function in Equation (4.2). Here I least-squares fit the theoretical segregation velocities (Equation (4.3)) directly in order to obtain $G = 3.7$ and $S_r = 1.7$. The fit is especially good at low ϕ , which is to be expected with a mixture of $\Phi = 30\%$. At high ϕ the uncertainty in the data for the large particles is considerable and the exponential flux function does not capture it well. It is not unreasonable to presume that the trend for large particles at high ϕ is unrealistic. The trend at high ϕ for small particles is captured well considering the fact the displacements should be very low. Certainly we would never expect to obtain an average displacement of zero with this statistical analysis.

For the analysis of segregation velocities in the shear-box I combine the statistics from mixtures

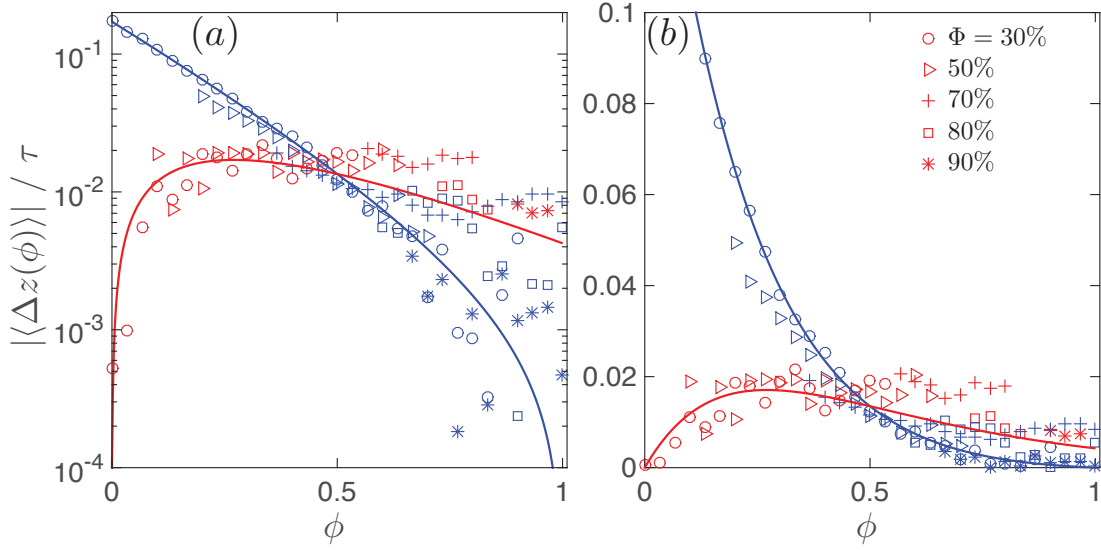


Figure 4.19: (a) Semi-log plot and (b) normal plot of the absolute values of the mean vertical displacement as a function of ϕ for large particles (red) and small particles (blue), normalized by τ . $W_{shell} = 2$ for small and $W_{shell} = 2.5$ for large particles, whilst $\tau = 1.5$. Data sets for different Φ are shown with different symbols, and only those data points are plotted that are averaged over at least 10,000 displacements. The blue line and red line are the theoretical small particle velocity and large particle velocity, respectively, using an exponential flux function with $S_r = 1.7$ and $G = 3.7$.

with different Φ . Because, in the chute flow we observe that the mean velocity varies with Φ we expect that the segregation velocities scale with Φ as well. Hence it is not reasonable to simply combine all the statistics. Therefore I plot the segregation velocities $|\langle \Delta z_v(\phi) \rangle| / \tau$ obtained from flows with different Φ with different symbols in Figure 4.19. In addition, to make the data easier to read I do not plot data points that are an average over less than 10,000 displacements. We find that the exponential flux function using $S_r = 1.7$ and $G = 3.7$ that we obtained by fitting to the data of $\Phi = 30\%$, captures the trend quite well. However, clearly there is significant variation among the different data sets as a result of the varying mean velocity. I have attempted to scale the data sets with the mean velocity of the flow but this did not collapse the data. Moreover, the scaling of the segregation velocities with the mean flow velocity does not follow a clear trend. The dataset that stands out in this regard is for $\Phi = 70\%$ (+ symbols), which has relatively high segregation velocities at high ϕ , compared to the other data sets. I currently do not have an explanation for this.

4.6 Conclusions

I conclude that the demonstration of an asymmetry in the dependency of the segregation velocities of large and small particles on the local volume fraction is quite convincing. Large particles are observed to segregate slowly in regions of many small particles, whilst small

particles segregate fast in regions of many large particles. The maximum segregation velocity of large particles is observed to lie at an intermediate concentration. I also demonstrate that size-segregation asymmetry affects the meso- and bulk-scale of the flow. In the development of $\phi(z, \hat{t})$, small particles reach the bottom of the flow faster than large particles reach the top. Furthermore, the segregation time increases linearly when a mixture contains a bigger fraction of small particles. I link the asymmetry to the different mechanisms that drive segregation of large and small particles. Small particles can make big segregation jumps through layers of large particles, whereas the segregation motion of large particles is of the order of the local reorganization in the surrounding small-particle matrix. The latter observation offers some new insights into the rising mechanism of single large intruders.

We observe the asymmetry in both a shear-box and in a chute, which proves that it is not an isolated effect, but occurs in the most common type of granular flows. Critically, we observe a greater asymmetry in the chute flow compared to the shear-box experiments. In the shear-box the segregation velocities are qualitatively captured by a cubic flux function, whereas in the chute flow an exponential flux function is required. The difference in maximum segregation velocities between large and small particles is tenfold in the chute flow, whereas it is only sixfold in the shear-box. At this point I can not give an explanation for this difference, but I suspect that it is related to the bigger size ratio used in the chute flows, and/or the higher shear rate. Although in theory the shear rate is thought to only effect the magnitude of the segregation velocities and not the degree of asymmetry, it is not known whether this is actually true. I also suspect that tracking errors in the shear-box analysis play a role in reducing the perceived asymmetry. Further investigation is required in this direction. I am currently investigating particle simulations in a shear-box geometry.

The advantage of the shear-box is that the shear rate is imposed and constant over the depth, whereas in the chute flow the shear rate is not constant. Which brings us to the point of discussing the uncertainties of the presented work. In the shear-box we isolate the dependency of the segregation velocity on the local concentration from that of shear-gradients, which are believed to also effect the velocities [Fan and Hill, 2011; Hill and Tan, 2014]. Temperature gradients, however, could theoretically still arise from the lithostatic pressure, but by using a very low shear-rate, it is safe to argue that this gradient is very small. Unfortunately in the chute flow this is not the case, and we cannot rule out the possibility that the the measured mean displacements are effected by the local shear-gradient. Particularly, because we also observe differences in mean flow velocity between different mixtures with varying global small particle content. There is a good chance that this gives rise to the large spread in the segregation velocity data. It is also not established yet whether pressure gradients affect segregation velocities.

The choice of shell width in the calculation of the local concentration around a particle is also critically important in the interpretation of the presented results. I have attempted to quantify my choice of the shell width, but I do not know if this interaction length depends on other parameters such as local downstream velocity, or pressure. Based on the data I argued that a

Chapter 4. Size-Segregation Asymmetry

different shell width for large and small particles is appropriate. I believe this is an important question that requires a more thorough investigation. Results of such an investigation could potentially also be very valuable for our understanding of granular flows in general.

5 Breaking Size-Segregation Waves

“Talent is luck. The important thing in life is courage.”

– Woody Allen

WHEN a mixture of large and small particles flows down an incline and segregates the large particles that rise to the free-surface will be carried towards the front of the flow because the higher layers of the flow move faster. When reaching the front these large particles accumulate or are deposited on the bed and overrun by the advancing flow. Large particles that are overrun can subsequently segregate again to the free-surface, repeating the cycle. This recirculation, sketched in Figure 5.1, gives rise to a complex structure that is called a *breaking size-segregation wave*.

The work discussed in this chapter is partly contained in the article titled “Asymmetric breaking size-segregation waves in dense granular free-surface flows” by P. Gajjar, K. van der Vaart, A. R. Thornton, C. G. Johnson, C. Ancey and J. M. N. T. Gray. The article was published in volume

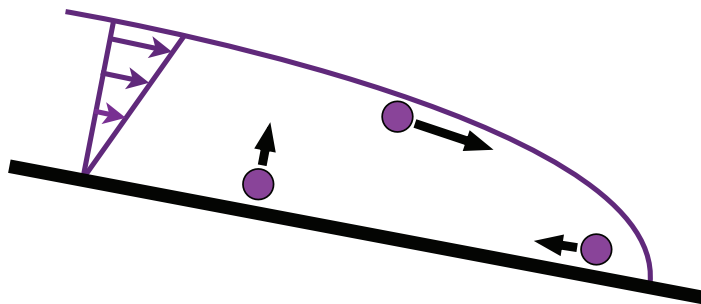


Figure 5.1: Movement of large particles near the front of an avalanche. A large particle segregates to the free-surface and travels to the front because higher layers move faster. When a large particle is deposited on the bed it effectively travels backwards because the avalanche is flowing over it. If this particle gets picked up by the flow it will segregate again.

794 of the *Journal of Fluid Mechanics* (2016), on pages 460–505. It contains mainly theoretical work with a comparison of the theory to experiments and simulations. My contributions are the experimental and simulation results which are discussed in this chapter in addition to analysis and discussion of not previously published results. The theoretical comparison, from the above mentioned article, is also shown in this chapter, but the details of the theory can be found in the article itself.

5.1 Introduction

Deposits of snow avalanches, debris and pyroclastic flows usually show evidence of bouldery or coarse grained fronts [e.g. Sharp and Nobles, 1953; Bagnold, 1968; Johnson, 1970; Takahashi, 1980, 1981; Johnson, 1984; Costa and Williams, 1984; Pierson, 1986; Iverson, 2014; Turnbull et al., 2015]. Figure 5.2 shows an example of this phenomenon: coarse material is deposited at the front of a snow avalanche, consisting of uprooted trees and coarse gravel. This coarse material typically experiences more friction with the mountain slope compared to the fine snow, and consequentially has a significant influence on the overall flow dynamics by acting as a ‘dam’ that resists the flow behind [Pierson, 1986]. Figure 5.2 also shows coarse material at the sides of the deposit, called lateral levees, or simply *levees*. They originate from the advancing more mobile fine grains within the interior of the flow that shoulder the coarse material at the



Figure 5.2: Field example of a snow avalanche that uprooted trees and entrained debris in the Puschlav valley (Grisons, Switzerland). The deposit exhibits a coarse front and lateral levees. Image courtesy of P. Bartelt, WSL-Institut, Davos.

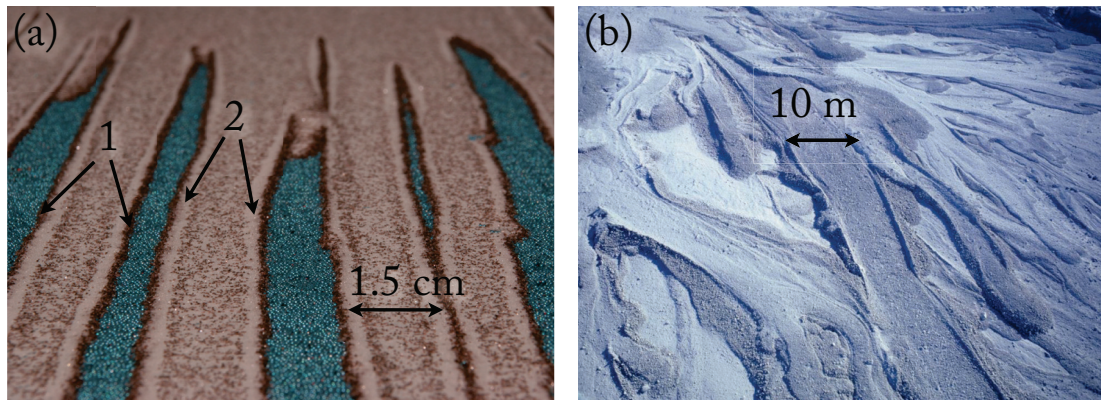


Figure 5.3: (a) Fingering in experiments, performed in the lab of Nico Gray at the University of Manchester, and in (b) pumiceous pyroclastic flow deposits from Mount St. Helens, 1980. Photograph courtesy of Dan Miller and USGS. Coarse lateral levees (1) made up of larger brown grains channelize the flow. These levees are lined with finer light colored grains (2). Similar features are observed in the pyroclastic flow deposit although at a completely different scale. The channels in the experimental deposit are approximately 1.5 cm, whereas in the pyroclastic deposit they are of the order of 10 m.

front to the sides [Major and Iverson, 1999; Johnson et al., 2012]. The levees are an important aspect of these type of flows because they are known to channelize the flow. The inside of the levees is often lined by a layer of deposited fine grains, which reduce the friction of the flow and increase the run-out distance [Kokelaar et al., 2014]. All of these phenomena are also observed in both large- and small- scale experiments [Iverson and Vallance, 2001; Iverson et al., 2010; Johnson et al., 2012].

The coarse resistive front has a complex interaction with the more mobile flow behind it. Pouliquen et al. [1997] were the first to observe an instability of the flow front in their experiments using inclined wide chutes. They found that the flow-front can break up into a number of distinct channels—a process referred to as fingering [Sharp and Nobles, 1953; Pouliquen et al., 1997; Woodhouse et al., 2012]. Figure 5.3 shows an example of this behaviour in experiments and in a naturally occurring pyroclastic flow deposits from Mount St. Helens.

Size-segregation is a key process within the formation of coarse grained fronts and lateral levees. The surface layers have the highest velocities, and so the segregated larger particles are transported to the front of the flow. After a coarse particle front has formed it is unlikely for smaller particles to reach the front because they segregate quickly to the bed upon entering the coarse front. If large particles in the front are overrun by the advancing flow and subsequently re-entrained, segregation will bring them back to the front once again. The combination of these processes creates a complex recirculating structure, that separates the coarse front from the small-particle tail of the flow. Figure 5.4 shows a schematic of the formation of this recirculation structure: When small particles are sheared over the large particles at the front the resulting configuration is unstable as a consequence of size-segregation. Size segregation will cause the small particles to sink and the large particles to rise. This causes the ‘wave’ of small particles to break and form a breaking size-segregation (BSS) wave.

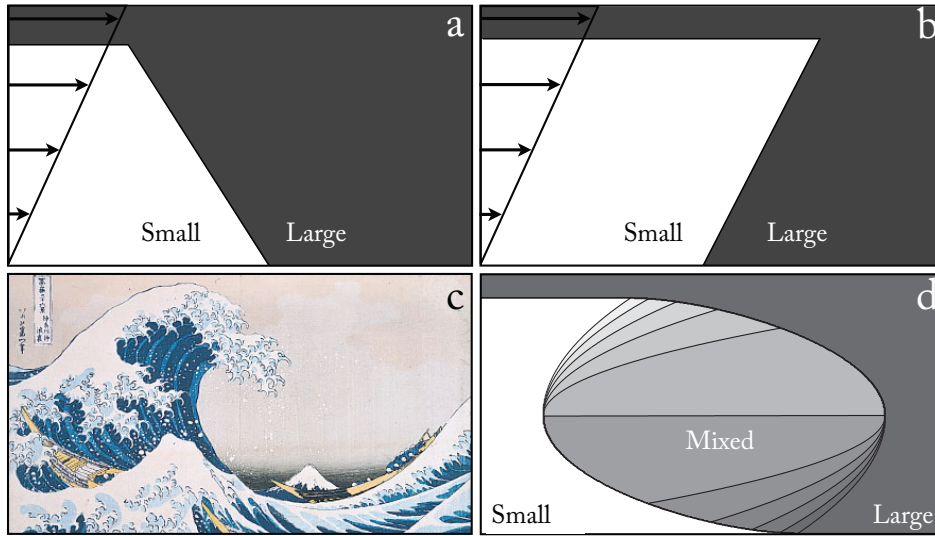


Figure 5.4: A schematic diagram showing the formation of a breaking size-segregation wave. First large particles accumulate at the front (a). Next, small particles are sheared over the large particles (b). Because of size-segregation this configuration is unstable and the “wave” of small particles breaks, similarly to the breaking of a water wave as illustrated by the woodcut print *The Great Wave* from the Japanese artist Katsushika Hokusai (c). The result is a complex recirculation structure of small and large particles (d).

The complex internal structure of a BSS wave has been theoretically predicted by Thornton and Gray [2008], but the first hints as to its existence were provided by Pouliquen et al. [1997] and Pouliquen and Vallance [1999], who used a moving camera to measure the recirculating motion of large particles placed on the surface of a flow of translucent smaller beads. Their observations of the wave, however, were only indirect, and more detailed experimental studies have been challenging due to sidewall effects and the complex time-dependence of BSS waves. The sidewalls are predominantly occupied by smaller particles which obscure the structure of the BSS wave. Furthermore, a BSS wave does not form instantaneously and when it has formed it travels close to the front of the flow, but not at the same velocity. As more large particles are carried to the front than are deposited, the coarse-grained front grows thereby pushing the BSS wave back [Gray and Kokelaar, 2010a,b]. In order to study this behaviour a very long chute is required to allow a steady BSS wave to emerge. Additionally there is the challenge of capturing the motion of the BSS wave close to the front using a moving camera.

A solution to this challenge is the *moving-bed channel* [Davies, 1990]. In this setup the channel bed moves upstream at a specific velocity, hence the lower layers of the flow are dragged upstream by the bed, whilst the upper layers move downstream under gravity. This significantly decreases the required length of the channel and circumvents the problem of the time-dependence, since the flow can continue indefinitely. Refractive index matched scanning (RIMS) addresses the problem of imaging through sidewalls since it permits visualization of the interior of the flow. Here I combine both these techniques to study breaking size-segregation waves in granular avalanches of a bi-disperse mixture.

5.2 Setup and Protocol

Experiments and discrete particle method (DPM) simulations have been performed in a moving-bed channel geometry. The full details of the setup, Channel A, can be found in Section 3.2.3.

I fine-tune the inclination angle of the channel and bed velocity in order to establish a uniform depth along the length of the channel, mimicking a normal free-surface flow as closely as possible. In practice, it is impossible to obtain this goal with high accuracy because of the size difference between the two particle species and the fact that the front of the flow is only a few large-particle diameters deep.

Figure 5.5 shows schematically how the flow configuration in the moving-bed channel is a section of a normal bi-disperse avalanche. In a bi-disperse avalanche the large particles will be segregated to the top, and, since the top layers have the highest velocity, there is an inflow of large particles towards the front. The front moves with velocity u_{front} , whilst the BSS wave, which is located behind the front has a velocity u_{wave} . The depth dependent velocity profile is given by $u(z)$. The flow in the moving-bed channel corresponds to the section centred on the BSS wave. The velocity profile in this section $\hat{u}(z) = u(z) - u_{wave}$. As a consequence the lower layers of the flow move upstream, whilst the upper layers move downstream. We can ignore the regions of the flow close to the upstream and downstream walls in the channel, where small particles are forced upwards and downwards, respectively, as long as I image and analyze the flow far from these walls. For convenience I will refer from here onward to $\hat{u}(z)$ simply as $u(z)$.

Below are outlined the specific parameters and protocol used in the experiments and simulations.

5.2.1 Experiments

Full details of the experimental geometry can be found in Section 3.2.3. The belt velocity $u_{belt} = 72 \text{ mm s}^{-1}$ and the bed inclination angle $\theta = 19.8^\circ$. The bi-disperse granular mixture consists of particles with diameters $d_l = 14 \text{ mm}$ and $d_s = 5 \text{ mm}$, with the total mixture volume ratio of small particles $\Phi = V_s^p / (V_s^p + V_l^p) = 70\%$. V_s^p and V_l^p are the large and small particle volumes. The experiment is prepared by pouring in the mixture of grains, after which the inclination angle and belt speed are set. The BSS wave forms quickly and becomes steady in less than a minute. At that point I can begin data collection.

The individual motion of the particles on the stream-wise centre line of the channel is revealed using refractive index matched scanning (RIMS) [Wiederseiner et al., 2011a; Dijksman et al., 2012]. The RIMS method and implementation is explained in detail in Sections 3.1.2 and 3.2.4. Only the particle motion on the stream-wise centre line is captured because scanning the entire width would require stopping the flow. Doing so would be possible by slowly lowering

the belt speed, however, I found that often after the belt came to a complete stop, the top of the flow would avalanche for a few seconds, thereby changing the flow structure. Thus I made the choice to not stop the flow and visualize only on the centre line. The upside of this approach is that we capture the structure of the flowing BSS wave.

The particle cross-sections on this centre line, obtained via RIMS, are tracked over time, with the minimum and maximum diameters used to determine whether that cross-section corresponds to a small or large particle. If a cross-section disappears and the diameter has not been conclusively determined it is ignored. The large size ratio between the grains minimizes

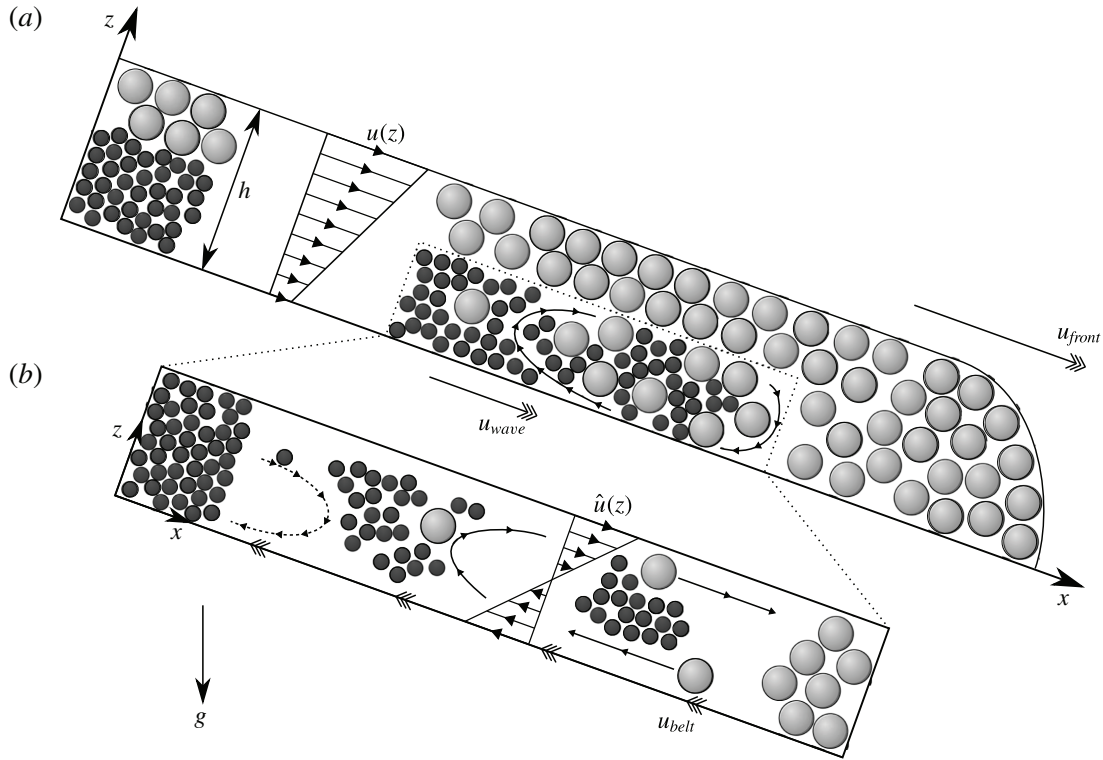


Figure 5.5: (a) A vertical section through a steadily propagating avalanche travelling down an inclined plane. In the body of the flow, the large grains segregate to the upper layers, where the velocity $u(z)$ is greatest, and hence are transported towards the front of the avalanche, where they are over-run, re-segregated upwards and recirculated to form a coarse-rich particle front. A breaking size-segregation wave forms between the vertically segregated flow in the rear of the avalanche and the coarse grained front. Although the front can increase in size when more large particles are supplied from the inversely graded flow upstream, the recirculation region shown with dotted lines reaches a steady structure that travels at the average speed u_{wave} . (b) In the moving-bed channel the belt moves upstream at a speed $u_{belt} = -u_{wave}$, driving an upstream flow in the lowest layers, whilst the upper layers move downstream under gravity. This generates a net velocity profile $\hat{u}(z) = u(z) - u_{wave}$ and is the same as examining the recirculation zone within the full avalanche (a) in a reference frame moving with u_{wave} . In the configuration in (b) there is no upstream supply of large particles, and so, provided that the segregation and diffusion rates are constant [Thornton and Gray, 2008], it is mathematically equivalent to the region in (a) marked by the dotted lines. Image reprinted from [Gajjar et al., 2016].

identification errors. There is a possibility that a large particle is mistaken for a small particle only if the particle is sliced very close to its edge and never moves closer to the plane of the laser. This however, is an unlikely event, because of the size difference; most of the time if a large particle is sliced this close to its edge the resulting disk on the image is too blurry to be resolved. Since the flow is in steady-state we can coarse-grain the disks in 2D (see Section 3.3) and time-average.

5.2.2 Numerical Simulations

The simulation details can be found in Section 3.3. A dry bi-disperse mixture of spherical particles is used, with all of the particles of the same (non-dimensional) density $\rho^* = \pi/6$, but of two different (non-dimensional) diameters, $d_s = 1$ and $d_l = 2.4$, for small and large particles respectively. All of the simulation parameters are non-dimensionalised so that $g = 1$. The global small particle volume ratio $\Phi(\%) = V_s^P / (V_s^P + V_l^P)$, where V_s^P and V_l^P are the total small and large particle volume respectively, is varied between different runs.

The simulations are conducted in a box of length $300d_s$ with fixed end walls, and width $8.9d_s$. The side-walls are periodic in order to remove side-wall effects. A rough moving base is used with particles of diameter $d_{base} = 1.7$ (see Section 3.3 for details on the creation of the base). Before each time step $\Delta t = 10^{-4} \sqrt{d_s/g}$, the base was moved upstream by a distance $u_{belt}\Delta t$. The system was allowed to evolve until a steady recirculation zone was formed. Two channel inclination angles have been used $\theta = 23^\circ$ or $\theta = 24^\circ$. A small inclined wall is placed between the base and the vertical upstream wall in order to prevent small particles being crushed between the wall and particles of the bed. The short inclined wall moves particles up before they impact the solid upstream wall. The placement of this wall only affects the dynamics very close to the wall, and did not affect the BSS wave. Time- and width-averaged concentration and velocity fields are produced by employing coarse-graining [Tunuguntla et al., 2015] (see Section 3.3).

5.3 Results

5.3.1 Phenomenology

A typical snapshot of the flow through the side-wall after the coarse front and small-particle tail have formed is shown in Figure 5.6(a). Large particles accumulate at the downstream end of the flow whilst small particles form the tail. Small particles sink to the bed before reaching the downstream wall and large particles rise to the free-surface before reaching the upstream wall. The tail is roughly six times longer than the coarse particle front. A long exposure shot in Figure 5.6(b) illustrates the time-averaged concentration field. The region between the front and tail where the recirculation takes place becomes more clearly visible, but the true structure is still mostly obscured by the small particles that are preferentially positioned near the side-walls. For this reason I apply RIMS in order to study the interior of the flow.

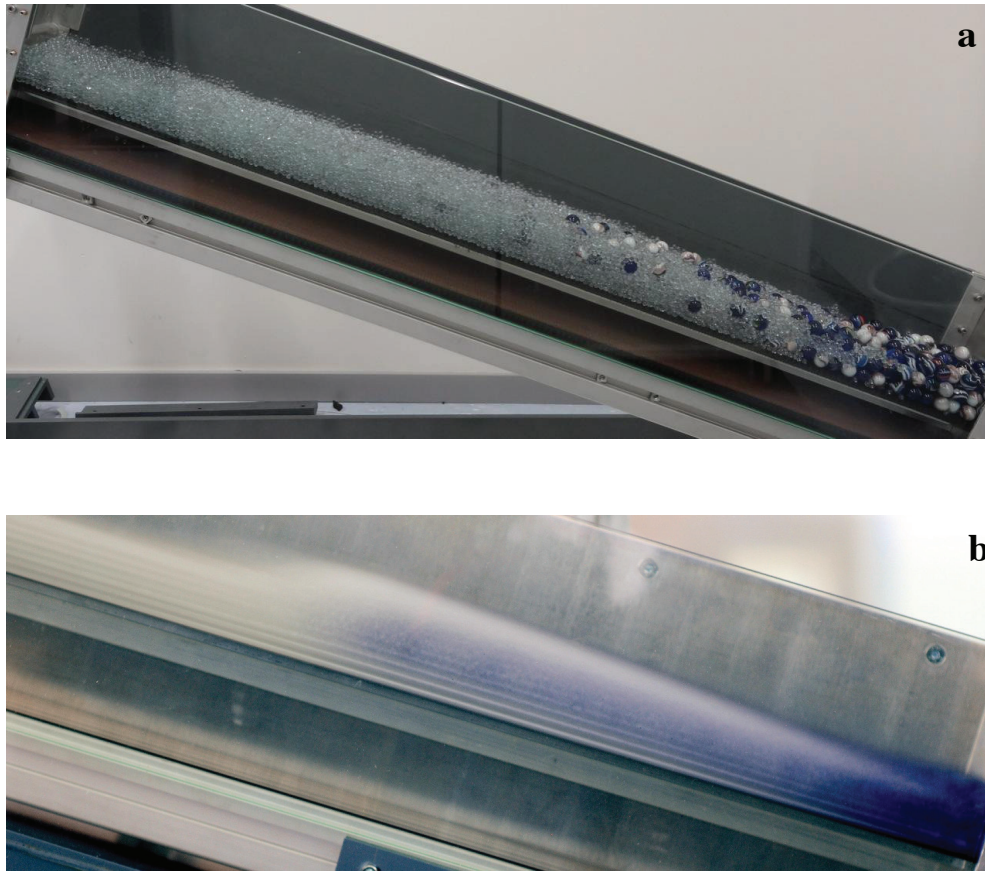


Figure 5.6: Photographs showing the steady recirculation regime established within the channel. These are dry preliminary tests using 5 mm and 14 mm glass marbles. The normal exposure photograph (a) shows that the large blue and white marbles collect towards the right, forming a coarse grained flow front at the downstream end of the channel, whilst the long exposure photograph (b) shows a time-averaged concentration field and the structure of the breaking size-segregation wave. An exposure time of 133 s was used to capture (b). Images reprinted from [Gajjar et al., 2016]

The ideal situation for the study of the BSS wave is when the large particles never reach the upstream wall and small particles never reach the downstream wall. In this case the BSS wave is isolated from the upper and lower boundary and fits in the channel. I found that this is hard to achieve even though the channel is 104 cm long. Careful fine-tuning of the flow depth, particle sizes, the value of Φ , and channel inclination was necessary to obtain satisfactory results.

Most often it is easy to obtain a coarse front, however, obtaining a BSS wave where the large particles do not reach the upstream wall is more challenging. I found that the large particles travel quite far upstream through the small particle tail. This behaviour is clearly the result of the size-segregation asymmetry discussed in Chapter 4. The upstream travel distance of the large particles can be reduced by decreasing the flow depth and increasing their segregation speed. The latter can be done by optimizing the size-ratio. A larger size-ratio facilitates an

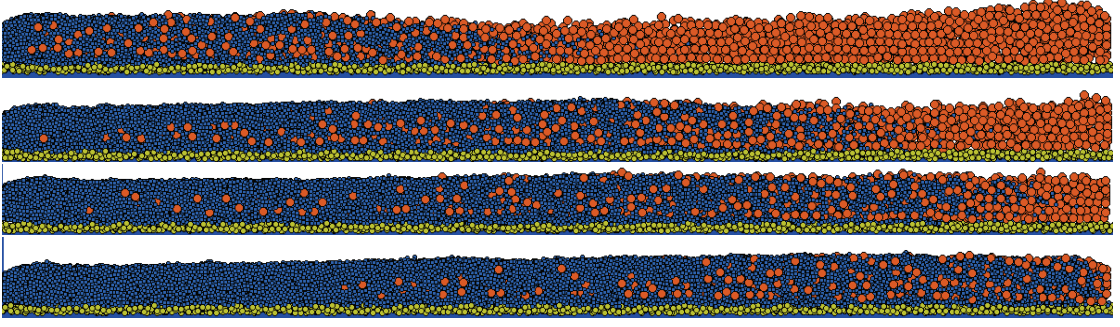


Figure 5.7: Snapshots of simulations with varying Φ . From top to bottom: $\Phi = 25\%$, 50% , 60% and 75% , for $u_{belt} = 3.55$, 3.2 , 3.2 and 3.4 , respectively.

easier coarse front formation, but rising of large in the tail is slower. A too small size ratio reduces segregation at both ends of the flow. By changing Φ we can also manipulate the space between the centre of the BSS wave and the upstream wall. If there are fewer large particles in the flow the centre of the BSS wave will move downstream. However, if the amount of large particles is too low, no coarse front will form. Adjusting the inclination, and thereby the flow velocity (since these are linked), has a complex effect on the upstream travel distance of large particles. A higher velocity results in a more kinetic flow, increasing the segregation speed, however large particles are also carried further upstream by the faster flow. Entrainment near the front is also increased, which reduces the size of the coarse front. If more particles are entrained the size of the BSS wave also increases.

Fortunately, our understanding of size-segregation is such that we can explain all of these behaviours, however it is clear that in order to study the BSS wave for different size ratios, flow velocities and flow depths, a much smaller mean particle size is required or a much longer channel.

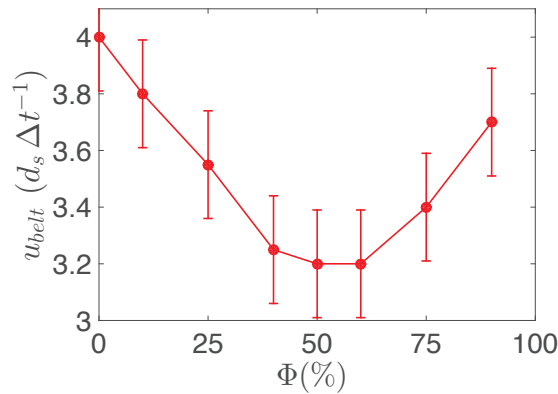


Figure 5.8: Belt velocity u_{belt} required to maintain a uniform flow depth along the channel for different global small-particle volume fractions Φ in the simulations.

The experimental data is obtained from a perfect BSS wave, i.e., one that fits in the channel. For the simulations I have recorded data from a number of different flows with varying global small-particle volume fractions and flow velocities. Naturally, only for some of these the BSS wave fits in the channel. For others no pure front or tail form at all, but segregation occurs nonetheless, as can be seen in some snapshots of these simulations with varying Φ and u_{belt} , shown in Figure 5.7. When varying Φ the depth along the channel changes. Adding more large particles or more small particles requires a higher belt velocity in order to maintain a uniform depth along the length of the channel. The lowest belt velocity is required around $\Phi = 50\%$. This trend is shown in Figure 5.8. In Section 5.3.6 an explanation for this behaviour is proposed.

5.3.2 Velocity Profile

Before showing the internal structure and particle recirculation in more detail, it is valuable to investigate the velocity profile. Figure 5.9 shows the height dependence of the horizontal velocity $u(z)$ in the experiment and simulations. In the experiment the scaling of the velocity is Bagnold like [Bagnold, 1954] in the particle tail, but closer to the coarse front, the velocity profile becomes more linear. This is reasonable since for very shallow flows the velocity profile tends to linear [Silbert et al., 2003; Rajchenbach, 2003], and the flow depth near the front is only a few large particles. We also observe significant reduction in horizontal velocity in the front of the flow, which indicates slip between the flow and the bed and less friction between the coarse particles in the front. The profile of the bed in the experiment is relatively small compared to the size of the large particles. Hence it is to be expected that the small-particle tail experiences a different amount of friction compared to the large-particle front. I do not view this behaviour as an unwanted artifact, since large boulders are known to be pushed en masse in front of debris flows. The overall effect of the decreased velocity of the coarse front is

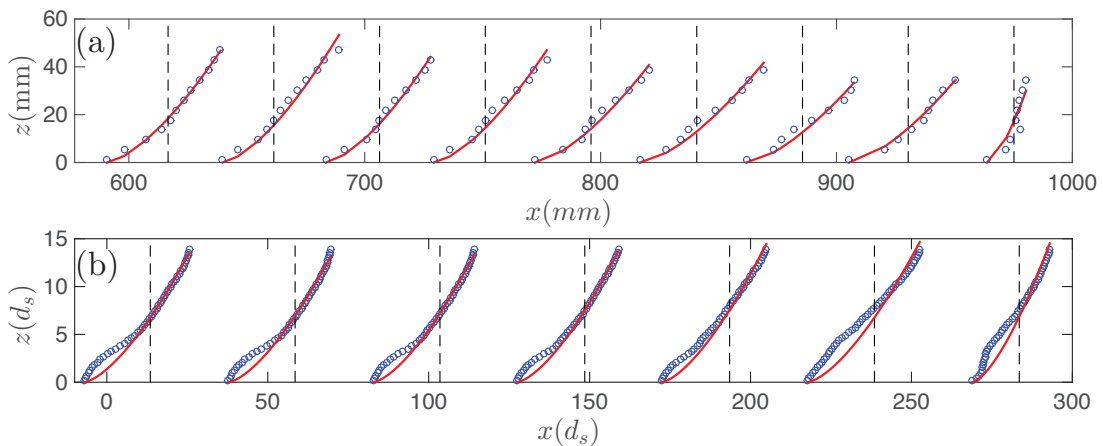


Figure 5.9: Horizontal velocity profiles at different x positions for (a) the experiment with $\Phi = 70\%$ and (b) the simulation with $\phi = 60\%$. Each black dashed line indicates the zero velocity line for the data taken at that position. Red dashed lines are fits with $f(z) = bz^{3/2}$, where b is some constant.

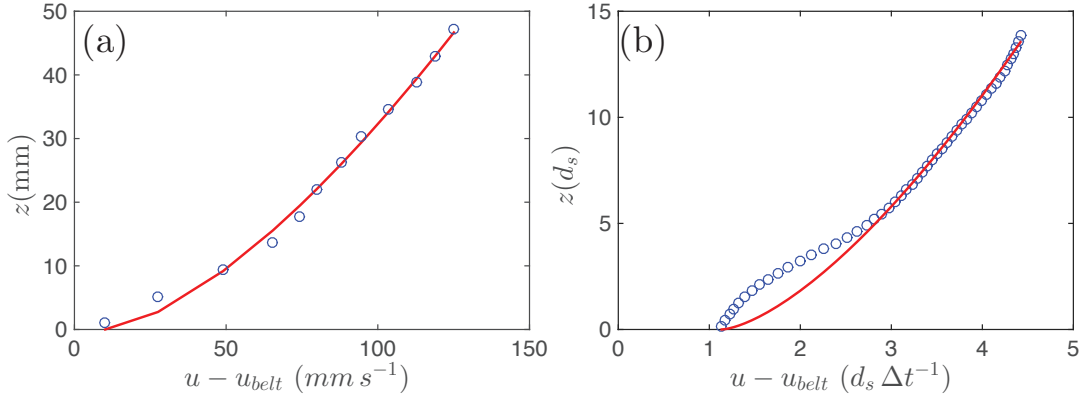


Figure 5.10: Horizontal velocity u minus u_{belt} versus depth z , in the small particle tail, for (a) the experiment with $\Phi = 70\%$ and (b) the simulation with $\Phi = 60\%$. Red dashed lines are fits with $f(z) = bz^{3/2}$, where b is some constant.

to promote its formation: a slower moving front makes it more likely for a small particle to have segregated to the bed before reaching the downstream wall.

For the simulations, looking at the tail region first, we only find a Bagnold scaling in the centre of the flow. Near the free-surface the velocity is slightly reduced, whilst at the bottom the velocity exhibits a quite unusual behaviour, which is likely also the result of slip with the bed. A possible explanation for this trend near the bed is suggested by the work of Thornton et al. [2012] who found that in similar chute flow simulations the gaps in the rough bed get filled by small particles. Possibly this results in a stronger decrease in velocity near the bed, compared to the Bagnold scaling. The seemingly linear scaling close to the free-surface is inline with the observations of Weinhart et al. [2012b], who found three different regimes for thick flows; a linear part near the free-surface and near the bed, and a Bagnold scaling in between. The linear part near the bed is, however, not present in the data presented here, possibly, because of the slip behaviour. Towards the front of the flow the velocity profile starts to deviate from a Bagnold like scaling as a whole, becoming more linear. The velocity at the front is also greatly reduced, again indicating slip.

Because the actual magnitudes of the velocities in Figure 5.9 are not indicated we take the velocity profile at the lowest x position and plot it in Figure 5.10. The velocity is shifted with u_{belt} in order to more clearly demonstrate the slip. We observe for both the experiment and the simulation that slip occurs. It is interesting that, although slip occurs in both the experiment and the simulation, the experimental velocity profile does not exhibit the strange scaling near the bed, which can be seen in the profile from the simulation. An explanation for this behaviour I can not give at this moment. Weinhart et al. [2012b] observed slip in their chute flow simulations with large size-ratios between the size of the bed particles and the (monodispersed) flow particles. In our simulations $d_{base} = 1.7$ whilst $d_l = 2.4$. They also observed that the slip scales with the mean flow velocity.

We will investigate the scaling of the slip in a later section. For now it is enough to be aware of the slip and continue our discussion with an analysis of the flow structure and particle recirculation.

5.3.3 Time-averaged Structure

Figure 5.11(a) and 5.11(b) show a typical snapshot of the interior of the flow in the experiment and in the simulation. It can be seen that large particles occupy the flow front and small particles the tail, whilst between the tail and the front a mixed region exists. We also observe how some large particles travel far inside the small-particle tail, whereas the small particles entering the large particle front do not seem to travel very far. This is more clearly demonstrated when looking at the time- and width-averaged small-particle volume fraction fields $\phi(x, z)$ in Figure 5.11(c) and 5.11(d). The volume fraction reveals the complex structure of the BSS wave, which is not evident from the snapshots. We still observe the purely large particle front ($\phi = 0$) and small-particle tail ($\phi = 1$), but in the mixed region a complex pattern can be observed that

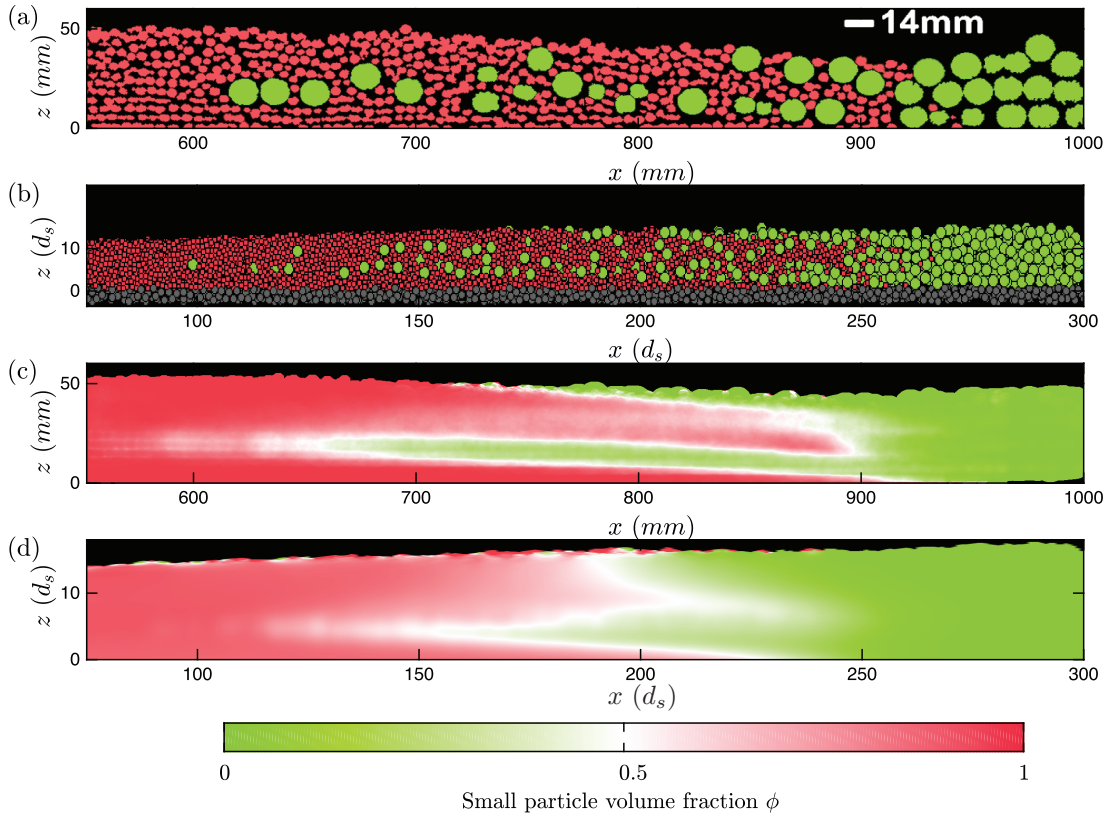


Figure 5.11: (a) Snapshot of the experiment. The white label indicates the length scale of 14 mm. (b) Snapshot of a simulation for $\Phi = 62\%$. The fixed base particles are shown in grey. (c) The experimental time-averaged small-particle volume fraction field $\phi(x, z)$. (d) The time-averaged small-particle volume fraction field for the simulations. Images adapted from [Gajjar et al., 2016].

is not simply equal to $\phi = 0.5$. For both the experiment and the simulation we see that the large particles travel quite far into the tail, as indicated by the low ϕ green and white region extending far into the red tail. Such a pattern is not observed in the front. I attribute these features to size-segregation asymmetry: After a large particle is deposited on the bed near the front it will be carried upstream and begin to segregate. Its segregation velocity diminishes the further it is carried back into the tail. It is likely that large particles segregate quickly closely behind the front, but it is not impossible for large particles to be carried further back before being entrained by the flow. On the other hand, small particles entering the large-particle front segregate quite fast.

The experiment and the simulation show a very similar pattern. This qualitative similarity between the simulations, which are laterally periodic, and the experiments, indicates that there are only minimal effects arising from the side-walls. It is impressive that with no calibration between the simulations and experiments and using different sized particles in different sized channels, both show a very similar pattern.

We will now further investigate the recirculation in the flow by means of particle trajectories and streamlines.

5.3.4 Recirculation

The $\phi(x, z)$ data discussed in the previous section provide a very detailed look at the structure of the BSS wave. However, it is not clear from this data how particles move precisely and if how recirculation takes place between the front and tail. Therefore we look at some typical particle trajectories as well as streamlines in this section. A typical trajectory of a single large particle, chosen at random, is shown in Figure 5.12(a). This data demonstrates how a large particle recirculates. The particle moves downstream above $z = 7.5$ and upstream below this height. The particle moves down towards the bed upon hitting the downstream wall and rises

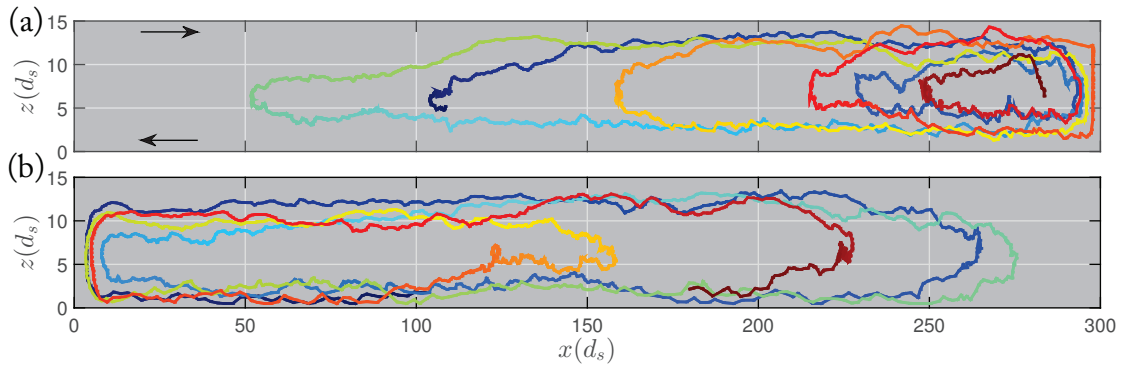


Figure 5.12: Simulation trajectories for a large particle (a) and a small particle (b) in a mixture of $\Phi = 50\%$, chosen at random. The color change in the trajectory is added to make it easier to follow. The arrows are a reminder that the top of the flow moves downstream, towards the right, and the bottom of the flow moves upstream, towards the left.

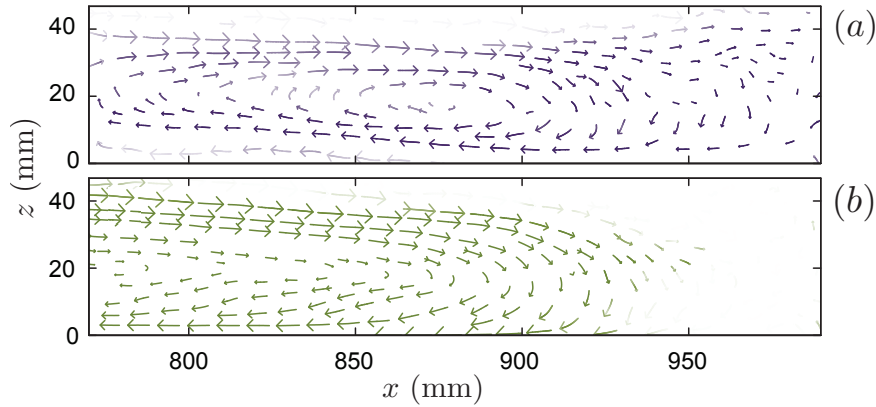


Figure 5.13: Experimental streamlines for large (a) and small (c) particles, constructed from velocity fields. Faded arrows indicate a lower concentration of that species.

everywhere else. Most of the time the large particle segregates to the free-surface close to the front, but sometimes it travels much further upstream before segregating.

Figure 5.12(b) shows a typical trajectory of a small particle. The small particle is pushed up against the upstream wall, and subsequently travels downstream. We observe that it actually travels quite far downstream before segregating to the bed. Naturally, diffusion within the small-particle tail can also cause a small particle to cross the vertical centre line of the flow, thereby changing its flow direction. The main difference with the trajectory of the large particle is that vertical movement of the small particle is quite steep, whereas the rising of the large particle, once it gets past $x = 150$, is very slow.

Figure 5.13 show streamlines obtained from velocity fields in the experiment indicating the

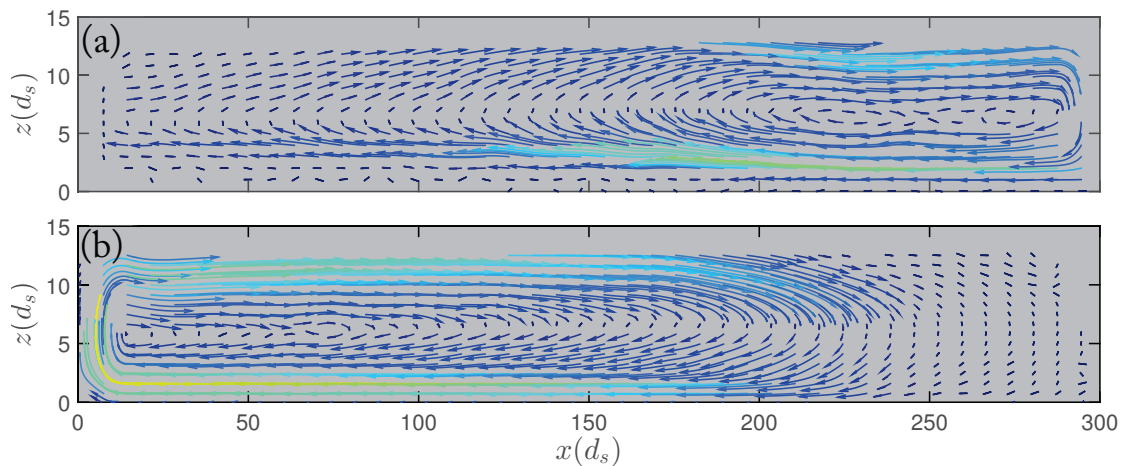


Figure 5.14: Simulation streamlines for large particles (a) and small particles (b). Lighter color and larger arrows indicates a higher velocity. For a $\Phi = 50\%$ mixture.

general flow of the two species. Segregation of small particles occurs predominantly in the region between $x = 850$ and $x = 950$. Large particles segregate below $x = 875$. Notice the beautiful eye-like pattern in the streamlines of the large particles. Streamlines obtained from the simulation data show qualitatively similar behaviour in Figure 5.14. The region where small particle sinking is strongest is positioned just to the right of the region where large particle rising is strongest. One difference between the simulation and experimental streamlines should be noted: In the experimental streamlines there occurs some downward movement of large particles in the same region as where the small particles move down, around $x = 925$. This is not the case in the simulation. I attribute this difference to the fact that more slip occurs in the experiment and the flow depth is lower. The large particle front in the experiment is much more a solid mass, as also indicated by the velocity profiles. As a consequence some large particle circulation towards the bed occurs at the start of the large particle front. This difference is likely the result of the different base roughnesses in the experiment and simulation.

5.3.5 Slip Velocity

In order to further investigate the slip with the bed we calculate the slip velocity $u_{slip} = u(z = 0) - u_{belt}$ along the entire length of channel, where $u_{belt} \leq 0$. We will compare data for different simulations with varying global small-particle concentration Φ and u_{belt} with uniform depth along the channel.

The slip velocity u_{slip} is plotted in Figure 5.15(a) for three different Φ . u_{slip} has a finite value along the entire channel for all three flows. Remarkably we observe how the slip exhibits two

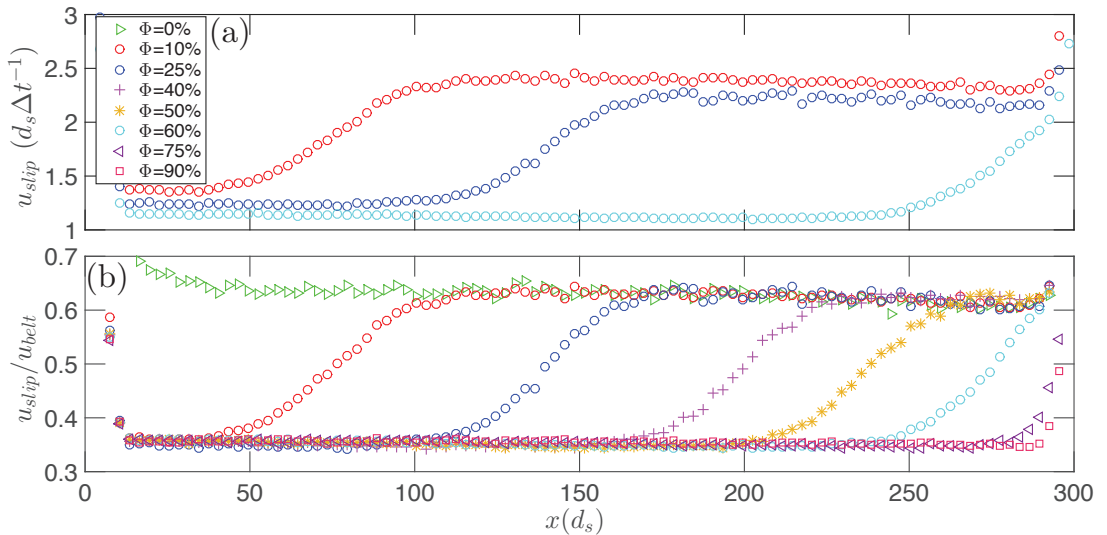


Figure 5.15: (a) Slip velocity $u_{slip} = u(z = 0) - u_{belt}$ in the simulations for three different global small-particle concentrations Φ . (b) Slip velocity in the simulations normalised by u_{belt} for mixtures of varying Φ and u_{belt} . The values of u_{belt} for each Φ can be found in Figure 5.8.

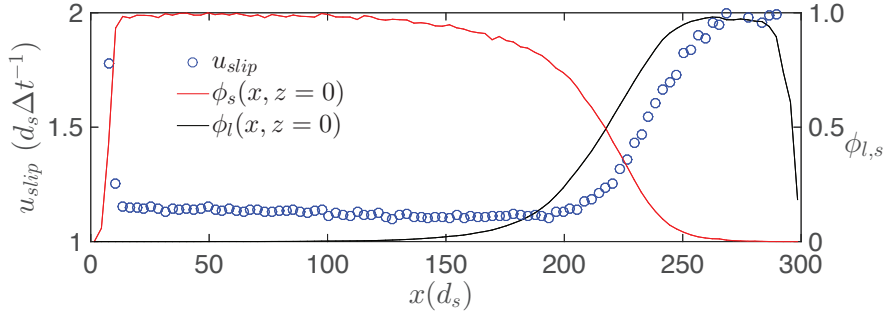


Figure 5.16: Slip velocity $u_{slip} = u(z=0) - u_{belt}$ for $\Phi = 50\%$ plotted together with $\phi(x, 0)$ and $\phi_l(x, 0) = 1 - \phi(x, 0)$.

plateau values, one high and one low. The x position of the transition between these plateaus increases with increasing Φ . We see a transition region for the curves of $\Phi = 10\%$ and $\Phi = 25\%$, whereas for $\Phi = 60\%$ the transition is shifted to the end of the channel and the second higher plateau is barely reached. We also see that the plateau values for the different flows are shifted vertically. The curves seem to shift down for higher Φ . However, I suspect this scaling results from a change in u_{belt} , which alters the mean velocity of the flow. Weinhart et al. [2012b] reported a scaling of slip with the mean velocity in their chute flow simulations. Indeed, if we divide u_{slip} by u_{belt} the two plateaus collapse for all data, as shown in Figure 5.15(b), clearly demonstrating that a higher u_{belt} gives rises to more slip independent of Φ .

Given that the transition between the plateaus shifts with Φ it is reasonable to associate them with the local presence of the two species, where the large-particle front experiences more slip compared to the tail. In Figure 5.16, u_{slip} is plotted for $\Phi = 50\%$ together with $\phi(x, 0)$ and $\phi_l(x, 0) = 1 - \phi$ of the same flow. The x -position where u_{slip} starts to increase to the higher plateau correlates with $\phi(0, x) \approx 0.5$. Possibly the slip scales linear with the mean local diameter, however, if I determine the ratio of the plateaus (after normalising with u_{belt}) I find a value of approximately $0.35/0.65 = 0.53$, whereas the ratio of the diameters is $d_s/d_l = 0.42$.

It is crucial to point out that the fraction of the bed that experiences a slip equal to the lower plateau value is always bigger than the fraction of small particles in the mixture. This must be the result of the preferential position of small particles at the bed, demonstrated by the data of $\phi(x, 0)$ in Figure 5.16 and Figure 5.11. A reduction of the internal friction coefficient in large-particle fronts has been previously predicted by Te Voortwis [2013]. Although not able to verify this in his own simulations, the results here support the theoretical predictions.

5.3.6 Mobility Feedback

Mobility feedback is the name for the inter-dependent relation that exists between the bulk flow and size-segregation [Gray and Ancey, 2009; Gray and Kokelaar, 2010a; Woodhouse et al., 2012]. In this section we will see that the presence of the BSS wave has a complex effect on the flow velocity through the vertical and horizontal separation of small and large particles and

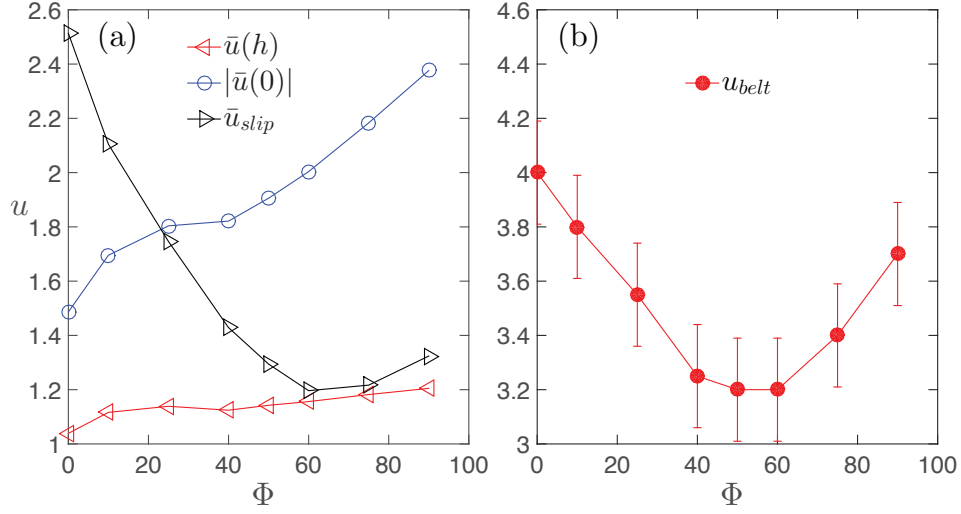


Figure 5.17: (a) Plotted as a function of Φ : The mean downstream free-surface velocity $\bar{u}(h)$, where h is the flow depth; the absolute value of the mean velocity at the bed $|\bar{u}(0)|$; and the mean slip velocity \bar{u}_{slip} . (b) The belt velocity as a function of Φ .

the basal slip that results from this separation.

Central in this discussion is the trend observed in Figure 5.8 where the belt velocity—required to maintain uniform depth—showed a minimum around $\Phi = 50\%$. In Figure 5.17(a) I plot the following data as a function of Φ : The mean downstream free-surface velocity $\bar{u}(h)$, where h is the flow depth; the absolute value of the mean velocity at the bed $|\bar{u}(0)|$; and the mean slip velocity \bar{u}_{slip} . The belt velocities for each value of Φ are replotted in Figure 5.17(b). The data demonstrates that, despite decreasing the belt velocity and subsequently increasing it, the flow velocity increases when adding more small particles to the flow.

This raises the following question: Why does the belt velocity need to be decreased between $\Phi = 0\%$ and 50% in order to maintain a uniform flow depth, whilst the flow velocity seems to increase? The mean slip velocity \bar{u}_{slip} suggests an answer to this question: As Φ increases the slip is reduced significantly, indicating that the addition of small particles increases the traction between the flowing mixture and the bed. Hence, the velocity at the bed is increased. The belt will drag more particles towards the upstream wall, increasing the flow depth. In order to compensate we can reduce u_{belt} . This reduction of u_{belt} will by itself increase the traction even more, but we can reduce u_{belt} enough such that a new balance is found. In this new balance the velocity near the bed and the velocity at the free-surface have increased.

Around $\Phi = 50\%$ we are forced to stop decreasing u_{belt} because more material starts to accumulate at the downstream wall. Why is the addition of small particles not forcing us to keep reducing the speed? Apparently the traction is no longer increased, which is confirmed by the minimum in the slip velocity. The bed is saturated with small particles despite Φ not being equal to 100% . This is demonstrated in Figure 5.15(a) where can be seen that at $\Phi = 60\%$

the lower slip plateau stretches nearly along the entire channel.

If we continue to add small particles we must start to increase u_{belt} because above $\Phi = 60\%$ the basal slip is no longer reduced by the addition of small particles. If we switch our reference point and consider that now we are removing large particles from a flow that is predominantly composed of small particles, doing so makes the flow internally less frictional [Te Voortwis, 2013; Staron and Phillips, 2015b], thereby increasing the flow velocity. Hence, we must increase the belt velocity to compensate. This increase of u_{belt} increases u_{slip} and we are forced to keep increasing u_{belt} in search of a new balance.

The presence of small particles in a bi-disperse granular flow has been reported to increase run-out distance and velocity by lubricating the bed [Linares-Guerrero et al., 2007; Phillips et al., 2006]. The data presented here demonstrates that, although we have to reduce the belt velocity in order to maintain a uniform flow depth, adding small particles increases the mean velocity of the flow, and removing large particles from the flow also increases the velocity, in agreement with previous findings and predictions [Te Voortwis, 2013; Staron and Phillips, 2015b].

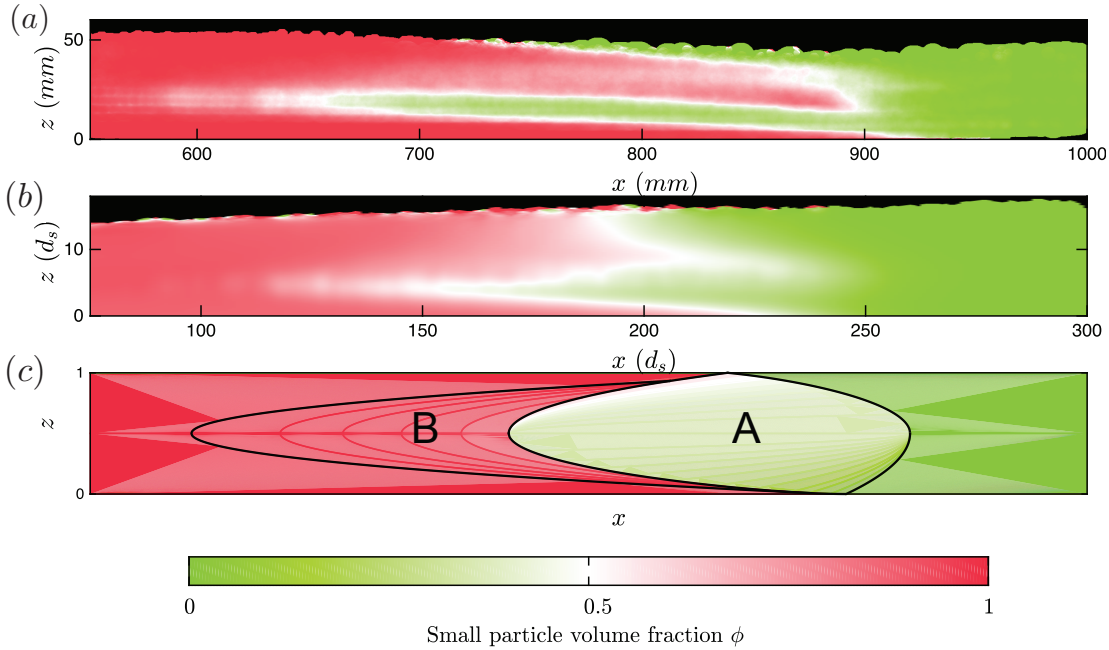


Figure 5.18: (a) The experimental time-averaged small-particle volume fraction field $\phi(x, z)$. (b) The time-averaged small-particle volume fraction field for the simulations. (c) Continuum BSS wave structure with an asymmetric flux function. The solid lines mark the boundaries of the recirculation zone, with two distinct ‘lens’ and ‘tail’ regions, marked by A and B respectively. Image adapted from [Gajjar et al., 2016].

5.3.7 Theoretical Comparison

This section discusses a comparison between the $\phi(z, x)$ fields obtained from the experiment and simulation and a theoretical prediction. The theory and theoretical solution is discussed in detail in [Gajjar et al., 2016]. The aim here is to show that implementing size-segregation asymmetry in the theory reproduces some important features of the experiment and simulation.

Figure 5.18(c) shows a theoretical solution of a BSS wave using the cubic flux function (Equation (4.5) in Section 4.4.4). The theoretical solution has a recirculation zone that separates the coarse front from the tail, marked by the solid black lines. The recirculation zone is divided in two and contains a so-called ‘lens’ structure on the right (A), and a large-particle ‘tail’ on the left (B). The cubic flux function gives rise to this asymmetric shape of the recirculation zone. A symmetric flux function results in a lens region that is symmetric in shape and does not produce a ‘tail’ [Gajjar et al., 2016]. In the tail of the recirculation zone large particles travel far into the small-particle tail of the flow and rise slowly. The lens region (A), where the segregation of small particles occurs, is obtuse on the side of the large-particle front, indicating a fast segregation of small particles in the front. Additionally, the theory accurately reproduces the higher proportion of small particles at the bed compared to the free-surface.

Although the above described features are in general very similar to the individual particle motion observed in experiments and simulations, the shape and structure of the recirculation zone produced by the theory is qualitatively different. This must be the result of a number of other factors present within the experiments and simulations that are unaccounted for by the simple theory. Stream-wise spatial variations in the velocity field, diffusive remixing, and the difference in basal slip of the two species, may all have an influence on $\phi(z, t)$. The size of the system and finite size effects probably also contribute to the discrepancy. Nevertheless, the ability of the asymmetric flux function to capture some of features of the experiment and simulations that I attribute to the asymmetry is remarkable.

5.4 Conclusions

The picture that emerges from the data is both simple and complex at the same time: We find several general features and behaviours that describe a breaking size-segregation (BSS) wave, such as a coarse front and a small-particle tail, a recirculation zone that is asymmetric, with large particles being carried further into the tail than small particles are carried into the front. The recirculation of particles arising from segregation is robust and occurs for various mixture ratios. On the other hand we observe a complex downstream velocity profile, with a significant amount of slip, linked to the presence of the different particle species near the bed. The travel distance of large particles into the tail has a complex dependence on numerous flow and mixture parameters. And we observe a complex relation between the velocity of the flow and the species mixing ratio.

Nonetheless I have demonstrated the existence of a recirculation pattern near the front of an avalanche that is the result of size-segregation. This direct evidence of breaking size-segregation waves opens the door to more detailed quantitative studies. The fact that an asymmetric flux function is essential for producing a ‘tail’ of slowly segregating large particles behind the recirculation zone provides further physical evidence for the asymmetry between large and small particle segregation velocities.

An important question that is left unanswered is whether we can confidently translate our findings to the situation of a normal avalanche? One that is not flowing on a moving bed. Will the relation between mixture ratio and flow velocity be similar? Closely related to this issue is whether the observed basal slip behaviour is unique to the moving-bed channel or not. One way to address this question is to perform simulations of a flow on very long channel. If the channel is long enough the breaking size-segregation wave can form and its structure can be investigated. The approach however will cost considerable computation time, because of the amount of particles required.

I must also comment on the simplifying assumptions of the work. In naturally occurring granular flows that exhibit coarse-front formation, the lateral freedom gives rise to additional effects, such as levee formation and fingering. In our configuration the side-walls in the experiment and the periodic walls in the simulation prevent such behaviour. Furthermore, I have used a bi-disperse mixture of spherical particles of small size-ratio. This is quite far from the reality, where particles range in size from micro-meters to meters and their shape is often not spherical. The particle shape influences in particular the basal slip: Spheres can easily rotate, whilst angular boulders are more likely to slide than roll. Indeed, a rolling resistance is part of the contact model used for the simulations, however, I did not investigate the effect of varying the amount of rolling resistance.

I believe that important topics for future investigation are; the stress fields inside the bulk, in order to determine whether indeed the removal of large particles from a small-particle flow reduces the internal friction and viscosity; and a verification of the belt speed dependence on Φ in the experimental geometry.

6 Conclusion and Outlook

“We shall not cease from exploration, and the end of all our exploring will be to arrive where we started and know the place for the first time.”

– T.S. Elliot

IN this dissertation I sought to gain insight into the particle-scale behaviour in the process of particle-size segregation in dense granular flows. I also sought to test fundamental theoretical assumptions in current state-of-the-art modelling approaches for size-segregation. In particular, whether the segregation velocities of small and large particles have an identical, but opposite dependence on local concentration. I also sought to reveal the internal structure of breaking size-segregation waves and verify the theoretical predictions.

I performed measurements of particle displacements and local concentration in an experimental shear-box geometry—using the non-intrusive imaging technique Refractive Index Matched Scanning (RIMS)—and in discrete particle simulations of a chute flow. These measurements demonstrate a fundamental asymmetry between large and small particles: The dependency of the segregation velocities on local concentration is different between large and small particles. In contrast to theoretical assumptions, the maximum velocity of large particles is lower than the maximum velocity of small particles, and the maximum velocity of large particles occurs at an intermediate concentration.

I also developed a moving-bed channel that works in combination with the RIMS technique. I used this novel facility to reveal the interior and structure of a breaking size-segregation wave. This recirculating structure separates the coarse particle front of a gravity driven avalanche from its small particle tail. I compared the findings with discrete particle simulations of the same flow configuration and observed qualitatively similar features. I also proposed an

explanation for the relation between mean flow velocity, species mixing ratio and basal slip.

By revealing the effect of size-segregation asymmetry I have introduced a new quantifiable property in size-segregating flows. This new measure allows investigators to characterize a size-segregating system on a more fundamental level. Theoretical models for size-segregation can be tested whether they reproduce this particle-scale property, before going through the effort of comparing solutions with experimental bulk features. Presumably, if the underlying particle dynamics are not accurately predicated, the predicated bulk behaviour is unlikely to match the reality.

This raises the question as to how asymmetry should be implemented in theoretical models. In current modelling approaches, the segregation velocities are directly linked to the stress partitioning between different sized species. Depending on the choice of stress partitioning, symmetric or asymmetric segregation velocities can be modelled. Such asymmetric stress partitioning has been verified in simulations [Weinhart et al., 2013; Hill and Tan, 2014; Staron and Phillips, 2014; Tunuguntla et al., 2016], however, importantly, the direct coupling between stress partitioning and segregation velocities has not yet been verified. What if the measured asymmetry in velocities does not match the asymmetry in stress partitioning? This has to be further investigated. If a difference is found, a possible solution lies in the inter-particle drag, which at the moment is assumed to be independent of the local concentration. However, one can imagine, for example, a small particle experiencing less drag when surrounded by many large particles, compared to a large particle surrounded by many small particles. The segregation velocities could result from a combination of concentration dependent drag and stress partitioning.

Through the discovery of size-segregation asymmetry I have also introduced a new understanding of various bulk features, such as the fast initial mixing of normally graded flows followed by a slower un-mixing [Golick and Daniels, 2009], and the linear dependence of segregation time on species mixture ratio [Staron and Phillips, 2014]. In breaking size-segregation waves asymmetry explains why large particles are carried far back in the small-particle tail, whilst slowly segregating. The formation of a coarse front is promoted by the fast segregation of small particles in such a front. These findings are likely to prove valuable in understanding the behaviour of naturally occurring avalanches.

The phenomenon of size-segregation asymmetry draws parallels with other fields. Namely, our observation of an optimal segregation condition for large particles at intermediate concentration, when a few large particles group together, brings to mind the behaviour of collective motion [Vicsek and Zafeiris, 2012; Aranson and Tsimring, 2006]. Collective motion can be observed in systems that follow seemingly simple rules on the particle-scale, that give rise to complex collective pattern formation at the bulk scale. Finding these rules is the challenge of the study of collective motion. Furthermore, asymmetric flux functions are also used to model asymmetry in sedimentation [Kynch, 1952; Batchelor, 1972; Diehl, 2007] and traffic flows [Lighthill and Whitham, 1955; Greenshields et al., 1935]. In the sedimentation of suspen-

sions, particles settle faster when traveling together, and the settling velocity goes to zero more rapidly than linear at high concentrations. Similarly, the velocity of cars in traffic approaches zero non-linearly at high car densities, and the optimal throughput occurs at intermediate concentration. The commonality between these processes opens up possibilities for using size-segregation as a model system.

A number of uncertainties in the presented work have been outlined in the respective chapters. I would like to point out the most important ones here. Isolating the velocity dependence on local concentration from other local effects, such as shear and pressure gradients, and the mean flow velocity, is a major challenge that could only partially be addressed in this dissertation. Hence, I can not rule out with certainty that these effects play a role in our results. Furthermore, in the study of breaking size-segregation waves, the relation between the length and depth of the flow forced us to study systems that were very shallow in terms of particle diameters. Thus finite-size effects are clearly visible in the results. This has made the comparison with theoretical solutions far from ideal.

The effect of the void space or packing fraction has been generally neglected in this work. This is mostly because the continuum frameworks that exists for size-segregation in dense granular flows ignore this parameter. Certainly however, it is reasonable to argue that packing fraction must play a crucial role in the dependency of the segregation velocities on local species volume fraction. For example, the low packing fraction at low small-particle volume fraction probably allows the small particles to segregate so fast. As soon as more small particles are added the packing fraction is increased and the segregation rate of small particles is reduced. Thus, the flux function should probably depend on the local packing fraction and the local species volume fraction. Since the packing fraction is known to depend on the inertial number, indirectly the flux function will too.

The findings presented in this dissertation open up a number of avenues for further investigation. As already mentioned above, the link between stress partitioning and asymmetry in velocities could be investigated. Furthermore, the inter-particle drag can be tested for a local volume fraction dependence. Diffusive remixing is currently also considered to be concentration in-dependent, an assumption that has not been verified yet. One can imagine that at low local small-particle concentration diffusion of small particles is considerable, because of the amount of void space. Diffusion of large particles at high small-particle concentration, on the other hand, is reasonably lower. As mentioned above, the effect of the packing fraction and inertial number could be further investigated to determine how the segregation flux depends on these non-dimensional quantities.

Concerning the uncertainties discussed in the previous paragraph, I believe that for the study of breaking size-segregation waves it will be invaluable to investigate much deeper flows, and verify whether the theoretically predicted structure captures the experiments better. Additionally, a more thorough attempt should be made to isolate the dependence of the segregation velocities on local concentration in order to measure the real flux function. Last

Chapter 6. Conclusion and Outlook

but not least, I provided some new insight into the rising mechanism of single large particles, but the fundamental origin of this rising is still far from understood.

I would like to conclude with a quote by science fiction author Frank Herbert that is perhaps valuable in the context of granular flows and size-segregation:

“A process cannot be understood by stopping it. Understanding must move with the flow of the process, must join it and flow with it.”

A Theoretical Segregation Velocities

This appendix outlines a compact derivation of the particle segregation velocities in the size-segregation modeling framework of Gray and Thornton [2005] as can be found in full detail in Gajjar and Gray [2014].

The momentum conservation law for each constituent $\nu = l, s$ in a bi-disperse mixture described in the mixture theory framework is:

$$\frac{\partial}{\partial t}(\rho_\nu \mathbf{u}_\nu) + \nabla \cdot (\rho_\nu \mathbf{u}_\nu \otimes \mathbf{u}_\nu) = \nabla p_\nu + \rho_\nu \mathbf{g} + \boldsymbol{\beta}_\nu \quad (\text{A.1})$$

where \otimes denotes the dyadic product, ∇ is the standard vector differential operator and \cdot is the dot product, \mathbf{g} is the gravitational force, ρ_ν , p_ν and \mathbf{u}_ν are the partial density, pressure and velocity, respectively, and $\boldsymbol{\beta}_\nu$ is the interaction force exerted on constituent ν by the other constituent. By Newton's third law, these interaction forces are equal and opposite, $\boldsymbol{\beta}_l = -\boldsymbol{\beta}_s$. The partial velocity \mathbf{u}_ν has components (u_ν, v_ν, w_ν) in the (x, y, z) directions.

It is assumed that the flow is shallow, i.e. the depth of the flow is much less than its length, so that the normal acceleration terms in the constituent momentum balances (A.1) may be neglected. The individual constituent momentum balances may be summed to give the bulk normal momentum balance,

$$0 = -\frac{\partial p}{\partial z} = \rho g \cos \zeta, \quad (\text{A.2})$$

where ζ is the slope inclination angle. By assuming the pressure to be zero at the free surface $z = h$, (A.2) can be integrated to show that the bulk pressure field is lithostatic,

$$p = \rho g (h - z) \cos \zeta. \quad (\text{A.3})$$

Each constituent is assumed to support a proportion of the bulk lithostatic pressure p :

$$p_s = f_s p, \quad p_l = f_l p, \quad (\text{A.4})$$

Appendix A. Theoretical Segregation Velocities

where the scaling factors f_v must sum to unity: $f_l + f_s = 1$. Each constituent cannot support negative pressure, so f_v lies in the range $0 \leq f_v \leq 1$. The interaction drag $\boldsymbol{\beta}_v$ in (A.1) is assumed to take the form

$$\boldsymbol{\beta}_v = p \nabla f_v - \rho_v c (\mathbf{u}_v - \mathbf{u}) - \rho d \nabla \phi_v, \quad (\text{A.5})$$

where coefficient c gives the magnitude of the linear drag between constituent v and the bulk particle matrix, and d gives the strength for the diffusive remixing.

With the interaction drag (A.5) and the lithostatic pressure distribution (A.3), the momentum balance (A.1) implies that the normal particle flux of constituent v is given by

$$\phi_v w_v = \phi_v w + (f_v - \phi_v) \frac{g}{c} \cos \zeta - \frac{d}{c} \frac{\partial \phi_v}{\partial z} \quad (\text{A.6})$$

In the bi-disperse case $\phi_l = 1 - \phi_s$ and hence $f_v - \phi_v$ can be written solely in terms of the small-particle concentration ϕ_s as

$$f_l - \phi_l = +bF(\phi_s), \quad (\text{A.7})$$

$$f_s - \phi_s = -bF(\phi_s) \quad (\text{A.8})$$

where $F(\phi_s)$ is the flux function which describes the dependence of the segregation on the small-particle volume fraction ϕ_s , and b is a parameter dependent on system properties.

In the absence of diffusion the last term in (A.6) is zero and the large- and small-particle segregation velocities in the normal direction can be derived by substituting (A.7) and (A.8) into (A.6) to give

$$w_l(\phi_s) = w + q \frac{F(\phi_s)}{1 - \phi_s}, \quad w_s(\phi_s) = w - q \frac{F(\phi_s)}{\phi_s}. \quad (\text{A.9})$$

where $q = g(b/c) \cos \zeta$.

Bibliography

- Ancey, C., Coussot, P., and Evesque, P. A theoretical framework for granular suspensions in a steady simple shear flow. *Journal of Rheology*, 43(6):1673–1699, 1999.
- Andreini, N. *Dam break of Newtonian fluids and granular suspensions: internal dynamics measurements*. PhD thesis, École Polytechnique Fédérale de Lausanne, 2016.
- Andreotti, B., Forterre, Y., and Pouliquen, O. *Granular media: between fluid and solid*. Cambridge University Press, 2013.
- Aranson, I. S. and Tsimring, L. S. Patterns and collective behavior in granular media: Theoretical concepts. *Reviews of Modern Physics*, 78:641–692, 2006.
- Armanini, A., Capart, H., Fraccarollo, L., and Larcher, M. Rheological stratification in experimental free-surface flows of granular–liquid mixtures. *Journal of Fluid Mechanics*, 532: 269–319, 2005.
- Artoni, R. and Richard, P. Average balance equations, scale dependence, and energy cascade for granular materials. *Physical Review E*, 91(3):032202, 2015.
- Babic, M. Average balance equations for granular materials. *International journal of engineering science*, 35(5):523–548, 1997.
- Bagnold, R. A. Experiments on a gravity-free dispersion of large solid spheres in a newtonian fluid under shear. *Proceedings of the Royal Society of London. Series A. Mathematical and Physical Sciences*, 225(1160):49–63, 1954.
- Bagnold, R. A. Deposition in the process of hydraulic transport. *Sedimentology*, 10(1):45–56, 1968.
- Ballard, D. H. Generalizing the hough transform to detect arbitrary shapes. *Pattern Recognition*, 13(2):111–122, 1981.
- Bartelt, P. and McArdell, B. W. Granulometric investigations of snow avalanches. *Journal of Glaciology*, 55(193):829–833, 2009.
- Batchelor, G. Sedimentation in a dilute dispersion of spheres. *Journal of Fluid Mechanics*, 52 (02):245–268, 1972.

Bibliography

- Batchelor, G. A brief guide to two-phase flow. In *Theoretical and Applied Mechanics*, volume 1, pages 27–40, 1989.
- Baxter, J., Tüzün, U., Heyes, D., Hayati, I., and Fredlund, P. Stratification in poured granular heaps. *Nature*, 391(6663):136–136, 1998.
- Bridgwater, J. Mixing and segregation mechanisms in particle flow. In *Granular Matter*, pages 161–193. Springer, 1994.
- Bridgwater, J. and Ingram, N. Rate of spontaneous inter-particle percolation. *Transactions of the Institution of Chemical Engineers*, 49(3):163, 1971.
- Brujić, J., Edwards, S. F., Hopkinson, I., and Makse, H. A. Measuring the distribution of interdroplet forces in a compressed emulsion system. *Physica A: Statistical Mechanics and its Applications*, 327(3):201–212, 2003.
- Capart, H., Young, D. L., and Zech, Y. Voronoï imaging methods for the measurement of granular flows. *Experiments in Fluids*, 32(1):121–135, 2002.
- Cas, R. A. F. and Wright, J. V. Volcanic successions, modern and ancient: A geological approach to processes, products and successions, 528 pp, 1987.
- Cassar, C., Nicolas, M., and Pouliquen, O. Submarine granular flows down inclined planes. *Physics of Fluids*, 17(10):103301, 2005.
- Cellai, D., Cregan, V., Curtis, M., Fowler, A., Hinch, J., Hocking, G., McGuinness, M., Murnane, J., O'Brien, S., and Smith, N. Particle size segregation in granular flow in silos. 2012.
- Chambon, G., Ghemmour, A., and Laigle, D. Gravity-driven surges of a viscoplastic fluid: An experimental study. *Journal of Non-Newtonian Fluid Mechanics*, 158(1):54–62, 2009.
- Chambon, G., Ghemmour, A., and Naaïm, M. Experimental investigation of viscoplastic free-surface flows in a steady uniform regime. *Journal of Fluid Mechanics*, 754:332–364, 2014.
- Chong, J., Christiansen, E., and Baer, A. Rheology of concentrated suspensions. *Journal of applied polymer science*, 15(8):2007–2021, 1971.
- Costa, J. E. and Williams, G. Debris flow dynamics. Technical Report 84–606, (videotape) U.S. Geological Survey, 1984.
- Crocker, J. C. and Weeks, E. R. Particle tracking using idl. *Retrieved from <http://www.physics.emory.edu/faculty/weeks/idl>*, 2000.
- Cross, J. *Electrostatics: Principles, Problems and Applications* (Bristol, UK: Adam Hilger). Bristol, UK: Adam Hilger, 1987.
- Cundall, P. A. and Strack, O. D. L. A discrete numerical model for granular assemblies. *Geotechnique*, 29(1):47–65, 1979.

- Davies, T. R. H. Debris-flow surges — experimental simulation. *Journal of Hydrology*, 29(1): 18–46, 1990.
- de Gennes, P.-G. Granular matter: a tentative view. *Reviews of Modern Physics*, 71(2):S374, 1999.
- Diehl, S. Estimation of the batch-settling flux function for an ideal suspension from only two experiments. *Chemical Engineering Science*, 62(17):4589–4601, 2007.
- Dijksman, J. A. and van Hecke, M. Granular flows in split-bottom geometries. *Soft Matter*, 6(13):2901–2907, 2010.
- Dijksman, J. A., Rietz, F., Lőrincz, K. A., van Hecke, M., and Losert, W. Invited article: Refractive index matched scanning of dense granular materials. *Reviews of Scientific Instruments*, 83(1):011301, 2012.
- Dingler, J. R. and Anima, R. J. Subaqueous grain flows at the head of carmel submarine canyon, california. *Journal of Sedimentary Research*, 59(2), 1989.
- Dodds, J. The porosity and contact points in multicomponent random sphere packings calculated by a simple statistical geometric model. *Journal of colloid and interface science*, 77(2):317–327, 1980.
- Dolgunin, V. N. and Ukolov, A. Segregation modeling of particle rapid gravity flow. *Powder Technology*, 83(2):95–103, 1995.
- du Pont, S. C., Gondret, P., Perrin, B., and Rabaud, M. Granular avalanches in fluids. *Physical Review Letters*, 90:044301, 2003a.
- du Pont, S. C., Gondret, P., Perrin, B., and Rabaud, M. Granular avalanches in fluids. *Physical Review Letters*, 90(4):044301, 2003b.
- Duran, J. *Sands, powders, and grains: an introduction to the physics of granular materials*. Springer Science & Business Media, 2012.
- Einav, I. Fracture propagation in brittle granular matter. In *Proceedings of the Royal Society of London A: Mathematical, Physical and Engineering Sciences*, volume 463, pages 3021–3035. The Royal Society, 2007.
- Ertaş, D., Grest, G. S., Halsey, T. C., Levine, D., and Silbert, L. E. Gravity-driven dense granular flows. *Europhysics Letters*, 56(2):214, 2001.
- Fan, Y. and Hill, K. M. Theory for shear-induced segregation of dense granular mixtures. *New Journal of Physics*, 13(9):095009, 2011.
- Fisher, R. V. and Mattinson, J. M. Wheeler gorge turbidite-conglomerate series, california; inverse grading. *Journal of Sedimentary Research*, 38(4), 1968.

Bibliography

- Forterre, Y. and Pouliquen, O. Flows of Dense Granular Media. *Annual Review of Fluid Mechanics*, 40:1–24, January 2008.
- Franklin, S. V. and Shattuck, M. D. *Handbook of Granular Materials*. CRC Press, 2016.
- Gajjar, P. and Gray, J. M. N. T. Asymmetric flux models for particle-size segregation in granular avalanches. *Journal of Fluid Mechanics*, 757:297–329, 10 2014.
- Gajjar, P., van der Vaart, K., Thornton, A., Johnson, C., Ancey, C., and Gray, J. M. N. T. Asymmetric breaking size-segregation waves in dense granular free-surface flows. *Journal of Fluid Mechanics*, 794:460–505, 2016.
- Gajjar, P. *Modelling Size-Segregation in Dense Granular Flows*. PhD thesis, University of Manchester, 2016.
- Gauch, J. M. Image segmentation and analysis via multiscale gradient watershed hierarchies. *IEEE Transactions on Image Processing*, 8(1):69–79, 1999.
- GDRMiDi. On dense granular flows. *European Physical Journal E*, 14:341–365, 2004.
- Glasser, B. and Goldhirsch, I. Scale dependence, correlations, and fluctuations of stresses in rapid granular flows. *Physics of Fluids*, 13(2):407–420, 2001.
- Goldhirsch, I. Stress, stress asymmetry and couple stress: from discrete particles to continuous fields. *Granular Matter*, 12(3):239–252, 2010.
- Golick, L. A. and Daniels, K. E. Mixing and segregation rates in sheared granular materials. *Physical Review E*, 80:042301, Oct 2009.
- Gray, J. M. N. T. and Ancey, C. Segregation, recirculation and deposition of coarse particles near two-dimensional avalanche fronts. *Journal of Fluid Mechanics*, 629:387–423, 2009.
- Gray, J. M. N. T. and Chugonov, V. A. Particle-size segregation and diffusive remixing in shallow granular avalanches. *Journal of Fluid Mechanics*, 569:365–398, 2006.
- Gray, J. M. N. T. and Kokelaar, B. P. Large particle segregation, transport and accumulation in granular free-surface flows. *Journal of Fluid Mechanics*, 652:105–137, 2010a.
- Gray, J. M. N. T. and Kokelaar, B. P. Erratum large particle segregation, transport and accumulation in granular free-surface flows – erratum. *Journal of Fluid Mechanics*, 657:539, 2010b.
- Gray, J. M. N. T. and Thornton, A. A theory for particle size segregation in shallow granular free-surface flows. *Proceedings of the Royal Society A: Mathematical, Physical and Engineering Science*, 461(2057):1447–1473, 2005.
- Gray, J. and Hutter, K. Pattern formation in granular avalanches. *Continuum Mechanics and Thermodynamics*, 9(6):341–345, 1997.

- Gray, J. M. N. T., Gajjar, P., and Kokelaar, P. Particle-size segregation in dense granular avalanches. *Comptes Rendus Physique*, 16(1):73–85, 2015.
- Greenshields, B., Channing, W., and Miller, H. A study of traffic capacity. In *Highway research board proceedings*, volume 1935. National Research Council (USA), Highway Research Board, 1935.
- Haralick, R. M., Sternberg, S. R., and Zhuang, X. Image analysis using mathematical morphology. *IEEE transactions on pattern analysis and machine intelligence*, (4):532–550, 1987.
- Herrmann, H. J., Hovi, J.-P., and Luding, S. *Physics of dry granular media*, volume 350. Springer Science & Business Media, 2013.
- Hill, K. M. and Tan, S. D. Segregation in dense sheared flows: gravity, temperature gradients, and stress partitioning. *Journal of Fluid Mechanics*, 756:54–88, 10 2014.
- Hill, K., Khakhar, D., Gilchrist, J., McCarthy, J., and Ottino, J. Segregation-driven organization in chaotic granular flows. *Proceedings of the National Academy of Sciences*, 96(21):11701–11706, 1999.
- Huerta, D. and Ruiz-Suárez, J. Vibration-induced granular segregation: a phenomenon driven by three mechanisms. *Physical Review Letters*, 92(11):114301, 2004.
- Hunter, R. E. Subaqueous sand-flow cross strata. *Journal of Sedimentary Research*, 55(6), 1985.
- Hunter, R. E. and Kocurek, G. An experimental study of subaqueous slipface deposition. *Journal of Sedimentary Research*, 56(3), 1986.
- Iverson, R. M. The physics of debris-flows. *Reviews of Geophysics*, 35:245–296, 1997.
- Iverson, R. M. Regulation of landslide motion by dilatancy and pore pressure feedback. *Journal of Geophysical Research: Earth Surface*, 110(F2):F02015, 2005.
- Iverson, R. M. Debris flows: behaviour and hazard assessment. *Geology Today*, 30(1):15–20, 2014.
- Iverson, R. M. and LaHusen, R. G. Dynamic pore-pressure fluctuations in rapidly shearing granular materials. *Science*, 246(4931):796–799, 1989.
- Iverson, R. M. and Vallance, J. W. New views of granular mass flows. *Geology*, 29(2):115–118, 2001.
- Iverson, R. M., Logan, M., LaHusen, R. G., and Berti, M. The perfect debris flow? aggregated results from 28 large-scale experiments. *Journal of Geophysical Research*, 115:F03005, JUL 10 2010.
- Jaeger, H. M., Nagel, S. R., and Behringer, R. P. The physics of granular materials. *Physics Today*, 49(4):32–38, 1996.

Bibliography

- Jha, A., Gill, J., and Puri, V. Percolation segregation in binary size mixtures of spherical and angular-shaped particles of different densities. *Particulate Science and Technology*, 26(5): 482–493, 2008.
- Johanson, J. Particle segregation... and what to do about it. *Chemical Engineering Journal*, May:183–188, 1978.
- Johanson, K., Eckert, C., Ghose, D., Djomlija, M., and Hubert, M. Quantitative measurement of particle segregation mechanisms. *Powder technology*, 159(1):1–12, 2005.
- Johnson, A. M. *Physical Processes in Geology*. Freeman, Cooper & Company, 1970.
- Johnson, A. M. Debris flows. In *Slope Instability*. Wiley, 1984.
- Johnson, C. G., Kokelaar, B. P., Iverson, R. M., Logan, M., LaHusen, R. G., and Gray, J. M. N. T. Grain-size segregation and levee formation in geophysical mass flows. *Journal of Geophysical Research*, 117(F1):013301, 2012.
- Jop, P., Forterre, Y. L., and Pouliquen, O. Crucial role of sidewalls in granular surface flows: consequences for the rheology. *Journal of Fluid Mechanics*, 541:167–192, 2005.
- Kaitna, R. and Rickenmann, D. A new experimental facility for laboratory debris flow investigation. *Journal of Hydraulic Research*, 45(6):797–810, 2007.
- Khakhar, D. V., McCarthy, J. J., and Ottino, J. M. Mixing and segregation of granular materials in chute flows. *Chaos*, 9:594–610, 1999.
- Khakhar, D. V. Rheology and mixing of granular materials. *Macromolecular Materials and Engineering*, 296(3-4):278–289, 2011.
- Knight, J. B., Jaeger, H. M., and Nagel, S. R. Vibration-induced size separation in granular media: The convection connection. *Physical Review Letters*, 70(24):3728–3731, Jun 1993.
- Kohonen, M. M., Geromichalos, D., Scheel, M., Schier, C., and Herminghaus, S. On capillary bridges in wet granular materials. *Physica A: Statistical Mechanics and its Applications*, 339 (1):7–15, 2004.
- Kokelaar, B. P., Graham, R. L., Gray, J. M. N. T., and Vallance, J. W. Fine-grained linings of leveed channels facilitate runout of granular flows. *Earth and Planetary Science Letters*, 385: 172–180, 2014.
- Kuhn, H. W. The hungarian method for the assignment problem. *Naval Research Logistics Quarterly*, 2(1-2):83–97, 1955.
- Kynch, G. J. A theory of sedimentation. *Transactions of the Faraday Society*, 48:166–176, 1952.
- LaMarche, K. R., Liu, X., Shah, S. K., Shinbrot, T., and Glasser, B. J. Electrostatic charging during the flow of grains from a cylinder. *Powder Technology*, 195(2):158–165, 2009.

- Leonardi, A., Cabrera, M., Wittel, F. K., Kaitna, R., Mendoza, M., Wu, W., and Herrmann, H. J. Granular-front formation in free-surface flow of concentrated suspensions. *Physical Review E*, 92(5):052204, 2015.
- Lighthill, M. J. and Whitham, G. B. On Kinematic Waves: II. A Theory Of Traffic Flow On Long Crowded Roads. *Proceedings of the Royal Society of London*, A229(1178):317–345, 1955.
- Linares-Guerrero, E., Goujon, C., and Zenit, R. Increased mobility of bidisperse granular avalanches. *Journal of Fluid Mechanics*, 593:475–504, 2007.
- Luding, S. Introduction to discrete element methods: basic of contact force models and how to perform the micro-macro transition to continuum theory. *European Journal of Environmental and Civil Engineering*, 12(7-8):785–826, 2008.
- Mahapatra, P. S., Mathew, S., Panchagnula, M. V., and Vedantam, S. Effect of size distribution on mixing of a polydisperse wet granular material in a belt-driven enclosure. *Granular Matter*, 18(2):1–12, 2016.
- Majmudar, T. S. and Behringer, R. P. Contact force measurements and stress-induced anisotropy in granular materials. *Nature*, 435(7045):1079–1082, 2005.
- Major, J. J. and Iverson, R. M. Debris-flow deposition: Effects of pore-fluid pressure and friction concentrated at flow margins. *Geological Society of America Bulletin*, 111(10):1424–1434, 1999.
- Marks, B. and Einav, I. A cellular automaton for segregation during granular avalanches. *Granular Matter*, 13:211–214, 2011.
- Marks, B., Einav, I., and Rognon, P. Polydisperse segregation down inclines: Towards degradation models of granular avalanches. In *Advances in Bifurcation and Degradation in Geomaterials*, pages 145–151. Springer, 2011.
- Marks, B., Rognon, P., and Einav, I. Grainsize dynamics of polydisperse granular segregation down inclined planes. *Journal of Fluid Mechanics*, 690:499–511, 2012.
- May, L. B. H., Golick, L. A., Phillips, K. C., Shearer, M., and Daniels, K. E. Shear-driven size segregation of granular materials: Modeling and experiment. *Physical Review E*, 81:051301, May 2010.
- McElwaine, J. and Nishimura, K. Size segregations in snow avalanches. In *IUTAM Symposium on Segregation in Granular Flows*, pages 81–88. Springer, 2000.
- Middleton, G. Experimental studies related to problem of flysch sedimentation. In Middleton, G. and Bouma, A., editors, *Flysch Sedimentology in North America (Lajoie, J., ed.) Business and Economics Science Ltd.*, pages 253–272, 1970.

Bibliography

- Middleton, G. and Hampton, M. Subaqueous sediment transport and deposition by sediment gravity flows. In Stanley, D. J. and Swift, D. J. P., editors, *Marine Sediment Transport and Environmental Management*, pages 197–218. John Wiley, New York, 1976.
- Mitarai, N. and Nori, F. Wet granular materials. *Advances in Physics*, 55(1-2):1–45, 2006.
- Morland, L. W. Flow of viscous fluids through a porous deformable matrix. *Surv. Geophys.*, 13(3):209–268, May 1992.
- Mueth, D. M., Jaeger, H. M., and Nagel, S. R. Force distribution in a granular medium. *Physical Review E*, 57(3):3164, 1998.
- Muite, B. K., Hunt, M. L., and Joseph, G. G. The effects of a counter-current interstitial flow on a discharging hourglass. *Physics of Fluids*, 16(9):3415–3425, 2004.
- Nakagawa, M., Altobelli, S., Caprihan, A., Fukushima, E., and Jeong, E.-K. Non-invasive measurements of granular flows by magnetic resonance imaging. *Experiments in Fluids*, 16(1):54–60, 1993.
- Nedderman, R. M. *Statics and kinematics of granular materials*. Cambridge University Press, 2005.
- Nityanand, N., Manley, B., and Henein, H. An analysis of radial segregation for different sized spherical solids in rotary cylinders. *Metallurgical Transactions B*, 17(2):247–257, 1986.
- Ottino, J. M. and Khakhar, D. V. Mixing and segregation of granular materials. *Annual Review of Fluid Mechanics*, 32(1):55–91, 2000.
- Pailha, M. and Pouliquen, O. A two-phase flow description of the initiation of underwater granular avalanches. *Journal of Fluid Mechanics*, 633:115–135, 8 2009.
- Pailha, M., Nicolas, M., and Pouliquen, O. Initiation of underwater granular avalanches: Influence of the initial volume fraction. *Physics of Fluids*, 20(11):111701, 2008.
- Parker, D., Dijkstra, A., Martin, T., and Seville, J. Positron emission particle tracking studies of spherical particle motion in rotating drums. *Chemical Engineering Science*, 52(13):2011–2022, 1997.
- Phillips, J., Hogg, A., Kerswell, R., and Thomas, N. Enhanced mobility of granular mixtures of fine and coarse particles. *Earth and Planetary Science Letters*, 246(34):466–480, 2006.
- Pierson, T. C. *Flow behavior of channelized debris flows, Mount St. Helens, Washington*, pages 269–296. Allen & Unwin, 1986.
- Pouliquen, O. Scaling laws in granular flows down rough inclined planes. *Physics of Fluids*, 11(3):542–548, 1999.
- Pouliquen, O. and Vallance, J. W. Segregation induced instabilities of granular fronts. *Chaos*, 9(3):621–630, 1999.

- Pouliquen, O., Delour, J., and Savage, S. B. Fingering in granular flows. *Nature*, 386:816–817, 1997.
- Pouliquen, O., Cassar, C., Jop, P., Forterre, Y., and Nicolas, M. Flow of dense granular material: towards simple constitutive laws. *Journal of Statistical Mechanics: Theory and Experiment*, 2006(07):P07020, 2006.
- Pouliquen, O. Velocity correlations in dense granular flows. *Physical Review Letters*, 93(24): 248001, 2004.
- Pouliquen, O. and Chevoir, F. Dense flows of dry granular material. *Comptes Rendus Physique*, 3(2):163–175, 2002.
- Rahman, M., Zhu, H., Yu, A., and Bridgwater, J. Dem simulation of particle percolation in a packed bed. *Particuology*, 6(6):475–482, 2008.
- Rajchenbach, J. Dense, rapid flows of inelastic grains under gravity. *Physical Review Letters*, 90 (14):144302, 2003.
- Remond, S. Dem simulation of small particles clogging in the packing of large beads. *Physica A: Statistical Mechanics and its Applications*, 389(21):4485–4496, 2010.
- Richefeu, V., El Youssoufi, M. S., and Radjai, F. Shear strength properties of wet granular materials. *Physical Review E*, 73(5):051304, 2006.
- Rognon, P. G., Roux, J.-N., Naaim, M., and Chevoir, F. Dense flows of bidisperse assemblies of disks down an inclined plane. *Physics of Fluids*, 19(5):058101, 2007.
- Rosato, A. D., Blackmoreb, D. L., Zhanga, N., and Lanc, Y. A perspective on vibration-induced size segregation of granular materials. *Chemical Engineering Science*, 57:265–275, 2002.
- Royer, J. R. and Chaikin, P. M. Precisely cyclic sand: Self-organization of periodically sheared frictional grains. *Proceedings of the National Academy of Sciences*, 112(1):49–53, 2015.
- Savage, S. B. and Lun, C. K. K. Particle size segregation in inclined chute flow of dry cohesionless granular solids. *Journal of Fluid Mechanics*, 189:311–335, 1988.
- Schlick, C. P., Fan, Y., Isner, A. B., Umbanhowar, P. B., Ottino, J. M., and Lueptow, R. M. Modeling segregation of bidisperse granular materials using physical control parameters in the quasi-2d bounded heap. *American Institute of Chemical Engineers Journal*, 61(5):1524–1534, 2015.
- Schmincke, H.-U. Graded lahars in the type sections of the ellensburg formation, south-central washington. *Journal of Sedimentary Research*, 37(2), 1967.
- Schofield, A. and Wroth, P. *Critical state soil mechanics*. McGraw-Hill London, 1968.
- Schröter, M., Ulrich, S., Kreft, J., Swift, J. B., and Swinney, H. L. Mechanisms in the size segregation of a binary granular mixture. *Physical Review E*, 74:011307, Jul 2006.

Bibliography

- Schulze, D. *Powders and Bulk Solids*. Springer, 2008.
- Scott, A. M. and Bridgwater, J. Self-diffusion of spherical particles in a simple shear apparatus. *Powder Technology*, 14(1):177–183, 1976.
- Scott, A. M. and Bridgwater, J. Interparticle percolation: a fundamental solids mixing mechanism. *Industrial & Engineering Chemistry Fundamentals*, 14(1):22–27, 1975.
- Sharp, R. P. and Nobles, L. H. Mudflow of 1941 at wrightwood, southern california. *Geological Society of America Bulletin*, 64(5):547–560, 1953.
- Shinbrot, T. and Muzzio, F. J. Nonequilibrium patterns in granular mixing and segregation. *Physics Today*, 53(3):25–30, 2000. doi: 10.1063/1.883018.
- Silbert, L. E., Ertas, D., Grest, G. S., Halsey, T. C., Levine, D., and Plimpton, S. J. Granular flow down an inclined plane: Bagnold scaling and rheology. *Physical Review E*, 64(5):051302, 2001.
- Silbert, L. E., Landry, J. W., and Grest, G. S. Granular flow down a rough inclined plane: transition between thin and thick piles. *Physics of Fluids*, 15(1):1–10, 2003.
- Sohn, Y. K. and Chough, S. K. The udo tuff cone, cheju island, south korea: transformation of pyroclastic fall into debris fall and grain flow on a steep volcanic cone slope. *Sedimentology*, 40(4):769–786, 1993.
- Staron, L. and Phillips, J. Segregation time-scale in bi-disperse granular flows. *Physics of Fluids*, 26(3):033302, 2014.
- Staron, L. and Phillips, J. Stress partition and microstructure in size-segregating granular flows. *Physical Review E*, 92(2):022210, 2015a.
- Staron, L. and Phillips, J. C. How large grains increase bulk friction in bi-disperse granular chute flows. *Computational Particle Mechanics*, pages 1–6, 2015b.
- Stephens, D. J. and Bridgwater, J. The mixing and segregation of cohesionless particulate materials part i. failure zone formation. *Powder Technology*, 21(1):17–28, 1978a.
- Stephens, D. J. and Bridgwater, J. The mixing and segregation of cohesionless particulate materials part ii. microscopic mechanisms for particles differing in size. *Powder Technology*, 21(1):29–44, 1978b.
- Takahashi, T. Debris flow on prismatic open channel. *Journal of the Hydraulics Division, ASCE*, 106(3):381–396, 1980.
- Takahashi, T. Debris flow. *Annual Review of Fluid Mechanics*, 13:57–77, 1981.
- Tang, P., Puri, V., and Patterson, P. Size segregation studies using a primary segregation shear cell. In *2002 ASAE Annual Meeting*, page 1. American Society of Agricultural and Biological Engineers, 2002.

- Te Voortwis, A. *Closure laws for granular shallow-layer, bi-dispersed flows down an inclined chute*. PhD thesis, Master Thesis. Multi Scale Mechanics Group. University of Twente, 2013.
- Thornton, A. R. and Gray, J. M. N. T. Breaking size segregation waves and particle recirculation in granular avalanches. *Journal of Fluid Mechanics*, 596:261–284, 2008.
- Thornton, A. R., Gray, J. M. N. T., and Hogg, A. J. A three-phase mixture theory for particle size segregation in shallow granular free-surface flows. *Journal of Fluid Mechanics*, 550:1–25, 2006.
- Thornton, A. R., Weinhart, T., Luding, S., and Bokhove, O. Modeling of particle size segregation: calibration using the discrete particle method. *International Journal of Modern Physics*, 23(8):1240014, Aug 2012.
- Thornton, A. R., Krijgsman, D., A. te Voortwis, V. O., Luding, S., Fransen, R., Gonzalez, S. I., Bokhove, O., Imole, O., and Weinhart, T. A review of recent work on the Discrete Particle Method at the University of Twente: An introduction to the open- source package Mercury-DPM. In *Proceedings of DEM6 - 6th International Conference on Discrete Particle Method*, 2013a.
- Thornton, A. R., Krijgsman, D., Fransen, R., Gonzalez, S., Tunuguntla, D. R., ten Voortwis, A., Luding, S., Bokhove, O., and Weinhart, T. Mercury-DPM: Fast particle simulations in complex geometries. *Newsletter of EnginSoft Year 10*, 1:48–53, 2013b.
- To, K., Lai, P.-Y., and Pak, H. Jamming of granular flow in a two-dimensional hopper. *Physical Review Letters*, 86(1):71, 2001.
- Tunuguntla, D. R., Bokhove, O., and Thornton, A. R. A mixture theory for size and density segregation in shallow granular free-surface flows. *Journal of fluid mechanics*, 749:99–112, 2014.
- Tunuguntla, D. R., Thornton, A. R., and Weinhart, T. From discrete elements to continuum fields: Extension to bidisperse systems. *Computational particle mechanics*, pages 1–17, 2015.
- Tunuguntla, D. R., Weinhart, T., and Thornton, A. R. Applying coarse-graining to perfectly bidisperse systems. *under review*, 2016.
- Turnbull, B., Bowman, E. T., and McElwaine, J. N. Debris flows: Experiments and modelling. *Comptes Rendus Physique*, 16(1):86–96, 2015.
- Vallance, J. W. and Savage, S. B. Particle segregation in granular flows down chutes. In Rosato, A. D. and Blackmore, D. L., editors, *IUTAM Symposium on segregation in granular materials*. Kluwer, 2000.
- Vicsek, T. and Zafeiris, A. Collective motion. *Physics Reports.*, 517(3):71–140, 2012.

Bibliography

- Wang, L., Frost, J., and Lai, J. Three-dimensional digital representation of granular material microstructure from x-ray tomography imaging. *Journal of Computing in Civil Engineering*, 18(1):28–35, 2004.
- Weinhart, T., Luding, S., and Thornton, A. R. From discrete particles to continuum fields in mixtures. *AIP Conference Proceedings*, 1542(1):1202–1205, 2013.
- Weinhart, T., Thornton, A. R., Luding, S., and Bokhove, O. From discrete particles to continuum fields near a boundary. *Granular Matter*, 14(2):289–294, 2012a.
- Weinhart, T., Thornton, A. R., Luding, S., and Bokhove, O. Closure relations for shallow granular flows from particle simulations. *Granular Matter*, 14(4):531–552, 2012b.
- Wiederseiner, S., Andreini, N., Epely-Chauvin, G., and Ancey, C. Refractive-index and density matching in concentrated particle suspensions: a review. *Experiments in Fluids*, 50: 1183–1206, 2011a.
- Wiederseiner, S., Andreini, N., Epely-Chauvin, G., Moser, G., Monnereau, M., Gray, J. M. N. T., and Ancey, C. Experimental investigation into segregating granular flows down chutes. *Physics of Fluids*, 23(1):013301, 2011b.
- Williams, J. C. The mixing of dry powders. *Powder Technology*, 2(1):13–20, 1968.
- Williams, J. C. Continuous mixing of solids. a review. *Powder Technol.*, 15(2):237–243, 1976.
- Woodhouse, M. J., Thornton, A. R., Johnson, C. G., Kokelaar, B. P., and Gray, J. M. N. T. Segregation-induced fingering instabilities in granular free-surface flows. *Journal of Fluid Mechanics*, 709:543–580, 2012.
- Zuriguel, I. and Mullin, T. The role of particle shape on the stress distribution in a sandpile. In *Proceedings of the Royal Society of London A: Mathematical, Physical and Engineering Sciences*, volume 464, pages 99–116. The Royal Society, 2008.

EDUCATION

-
- | | |
|--|-------------|
| Ph.D. in Mechanics , EPFL, LAUSANNE, SWITZERLAND | AUGUST 2016 |
| Research Area: Granular Physics | |
| Dissertation: <i>Particle-Size Segregation in Dense Granular Flows</i> . | |
| M.Sc. in Physics , UNIVERSITY OF UTRECHT, NETHERLANDS | AUGUST 2011 |
| Research focus: Photonics and Soft Matter | |
| Dissertation: <i>New Physical Insights into Chocolate Rheology</i> . | |
| B.Sc. in Physics , UNIVERSITY OF AMSTERDAM, NETHERLANDS | AUGUST 2009 |
| Research focus: Photonics and Soft Matter | |
| Dissertation: <i>Light from Silicon Nano Crystals</i> . | |

SERVICES & PROFESSIONAL ACTIVITIES

-
- | | |
|---|-----------------------|
| User committee member | MAY 2015 — NOW |
| Dutch Technology Foundation STW, Research project 13472 | |
| Session co-convener | APRIL 2014 |
| European Geosciences Union (EGU), General Assembly | |
| Committee member | SEP. 2007 — AUG. 2008 |
| Physics & Astronomy Bachelor committee, University of Amsterdam | |
| Peer review | FEB. 2015 — NOW |
| Physical Review E, Physical Review Fluids | |

HONORS & AWARDS

-
- Nominated for EPFL doctorate award 2017**
- EPFL Prime Special 2013**
Awarded to PhD students for demonstrating exceptional merit

CONFERENCE TALKS

-
- "Breaking size-segregation waves in granular avalanches." APS March Meeting, Denver. March 2014.
 - "Breaking size-segregation waves in granular avalanches." AERC Meeting, Karlsruhe. April 2014
 - "Segregation in a quasi-stationary avalanche on an inclined conveyor-belt." 2nd IMA Conference on Dense Granular Flows, Cambridge. July 2013.

INVITED TALKS

-
- "Asymmetric particle behavior during size segregation." Particles Conference, Barcelona. September 2015.

PUBLICATIONS

- (1) P. Gajjar, **K. van der Vaart**, A.R. Thornton, C.G. Johnson, C. Ancey, and J.M.N.T. Gray, "Asymmetric breaking size segregation waves." *Journal of Fluid Mechanics*, 2016.
- (2) **K. van der Vaart**, P. Gajjar, J.M.N.T. Gray, and C. Ancey, "Underlying Asymmetry within Particle Size Segregation." *Physical Review Letters*, 2015.
- (3) **K. van der Vaart**, Y. Rahmani, Z. Hu, D. Bonn, and P. Schall, "Rheology of concentrated soft and hard-sphere suspensions." *Journal of Rheology*, 2013.
- (4) **K. van der Vaart**, F. Depypere, V. De Graef, P. Schall, A. Fall, D. Bonn, and K. Dewettinck, "Dark chocolate's compositional effects revealed by oscillatory rheology." *European Food Research and Technology*, 2013.
- (5) Y. Rahmani, **K. van der Vaart**, B. van Dam, Z. Hu, V. Chikkadi, and P. Schall, "Dynamic heterogeneity in hard and soft sphere colloidal glasses." *Soft Matter*, 2012.

TEACHING

- **Teaching Assistant**, EPFL, LAUSANNE, SWITZERLAND
 - Analysis I, bachelor Mathematics, 5ECTS 1 SEMESTER
 - Hydraulics, master Civil Engineering, 5ECTS 4 SEMESTERS
 - Fluid Mechanics, master Civil Engineering, 5ECTS 4 SEMESTERS
 - Fluid Mechanics, bachelor Civil Engineering, 5ECTS 4 SEMESTERS
 - General Physics I, bachelor Physics, 5ECTS 1 SEMESTER
- **Practicum Assistant**, UNIVERSITY OF AMSTERDAM, NETHERLANDS
 - Practicum I, bachelor Physics & Astronomy, 5ECTS 2 SEMESTERS

SUPERVISION

- **Master Theses**
 - Jean-François Poustis, *Size segregation in dense granular flows.* SUMMER 2015
 - Justine Caillet, *Asymmetric size-segregation process in dense granular flows.* SUMMER 2014
 - Jean-Lou Pfister, *Experimental study of size-segregation in dense granular avalanches.* SUMMER 2013

